

COMPUTATIONAL MECHANICS OF TAINTER GATES; TRUNNION FRICTION STUDY

by

Norma L. Álvarez Quiñones

A thesis submitted in partial fulfillment of the requirements for the degree of

MASTER OF SCIENCE
in
CIVIL ENGINEERING

UNIVERSITY OF PUERTO RICO
MAYAGÜEZ CAMPUS
2012

Approved by:

Guillermo Riveros, PhD
President, Graduate Committee

Date

Felipe Acosta, PhD
Member, Graduate Committee

Date

Ricardo Lopez, PhD
Member, Graduate Committee

Date

, PhD
Representative of Graduate Studies

Date

Ismael Pagán Trinidad, MSCE
Chairperson of the Department

Date

ABSTRACT

Tainter gates are a type of floodgate with a radial geometry that is used in dams and canal locks to control the water flow from navigation structures. Throughout the years, these structures have presented operational difficulties and structural problems, frequently attributed to the effect of trunnion friction. In 1995, tainter gate #3 on Folsom Dam, California, failed catastrophically releasing approximately 40,000 cu ft/sec, which caused several flooding problems in the region. The forensic studies described the trunnion friction as the main cause of the failure. This gate was designed in the 1960s, when moment induced by the friction in the trunnion was not considered in the design of the gate; this was a common engineering practice at the time.

In 2008, Dr. Gopalarathnam, from the University of Missouri-Columbia and Dr. Riveros, from the U.S. Army Engineer Research and Development Center performed a series of experimental tests in a tainter gate located in the Carlyle Lake Dam, IL. The purpose was to measure the strains in the elements while the gate was lifted and lowered and study the effect of moment induced friction in the structure. For this study a 3-D numerical model of the Carlyle Lake Dam tainter gate was created and validated with the experimental data obtained from the tests performed in 2008 using Finite Element Analysis. A series of parametrical analyses were performed including the increment in friction coefficient in the trunnion bearing and a study of unsymmetrical cable pressure. The analytical results obtained from the 3-D numerical model concluded that the strain magnitudes are directly proportional to the friction coefficient in the trunnion and that the moment induced by the friction in the trunnion only affects the structure when it is under operation.

RESUMEN

Las compuertas radiales “tainter” se utilizan en represas y canales para controlar el flujo de agua. A través de los años estas estructuras han presentados dificultades operacionales, frecuentemente atribuidas al efecto de fricción en el área del “trunnion”. En 1995, la compuerta #3 de la Represa Folsom localizada en California fallo inesperadamente descargando aproximadamente 40,000 cu ft/sec, lo cual produjo severos problemas de inundaciones en la región. Los estudios forensicos atribuyeron el origen de la falla al incremento en fricción en el área del “trunnion”. Esta compuerta fue diseñada en los 1960s donde el momento inducido por la fricción en el “trunnion” no era tomado en consideración para el diseño de la compuerta; esto era una práctica común para ese tiempo.

En el 2008, Dr. Gopalarathnam, de la University of Missouri-Columbia y Dr. Riveros, del U.S. Army Engineer Research and Development Center realizaron una serie de experimentos en una compuerta “tainter” localizada en la represa Carlyle, en Illinois. El propósito de estos experimentos fue medir las deformaciones en los elementos mientras la compuerta estaba en operación para estudiar los efectos en la compuerta del momento inducido por la fricción en el área del “trunnion”. Para este estudio se creó un modelo numérico 3-D de la compuerta de de la represa Carlyle y fue calibrado con los datos experimentales obtenidos en las pruebas realizadas en el 2008 utilizando un análisis de elementos finitos. Una serie de análisis paramétricos fueron realizados incluyendo el aumento de coeficiente de fricción en el “trunnion” y un estudio de no simetría en la presión de los cables. Los resultados obtenidos del modelo numérico 3-D reflejan que la magnitud de las deformaciones es directamente proporcional al coeficiente de fricción en

el “trunnion” y el momento inducido por la fricción en esa área solo afecta a los elementos en la compuerta cuando está en operación.

© Norma Luz Álvarez Quiñones 2012

DEDICATION

To my parents, Norma and Manuel, for always supporting me with all their love and effort.

ACKNOWLEDGEMENTS

LEFT BLANK FOR SUBMITTAL TO GRADUATE SCHOOL

Table of Contents

ABSTRACT	II
ACKNOWLEDGEMENTS	VII
TABLE OF CONTENTS	VIII
TABLE LIST	X
FIGURE LIST.....	XI
1 INTRODUCTION.....	1
1.1 INTRODUCTION TO TAINTER GATES	1
1.2 MOTIVATION.....	4
1.3 PROBLEM DESCRIPTION	9
1.4 OBJECTIVES	13
1.5 SCOPE OF WORK	14
1.6 OVERVIEW	15
2 DESIGN CONSIDERATIONS OF TAINTER GATES.....	17
2.1 GENERAL FEATURES OF DESIGN	17
2.1.1 <i>Skin-plate assembly</i>	19
2.1.2 <i>Girder-strut arm assembly</i>	23
2.1.3 <i>End Frames</i>	24
2.1.4 <i>Trunnion assembly</i>	25
2.1.5 <i>Friction Design Considerations</i>	26
2.2 CARLYLE TAINTER GATE EVALUATION.....	27
2.2.1 <i>Bottom Horizontal Girder Evaluation</i>	27
2.2.2 <i>Bottom Strut arm Evaluation</i>	35
3 TAINTER GATES EXPERIMENTAL STUDIES AT CARLYLE DAM	42
3.1 EXPERIMENTAL PROCEDURE	42
3.2 EXPERIMENTAL RESULTS	47
3.3 EXPERIMENTAL PROCEDURE ACHIEVEMENTS.....	61
4 COMPUTATIONAL STUDY OF TAINTER GATES.....	62
4.1 COMPUTATIONAL MODELING	63
4.2 COMPUTATIONAL SIMULATION.....	66
4.2.1 <i>Finite Element Method (FEM)</i>	66
4.2.2 <i>Simulation of experimental procedure</i>	70
4.2.3 <i>Interaction simulation</i>	74
5 EXPERIMENTAL VALIDATION, TRUNNION FRICTION STUDY AND PARAMETRIC ANALYSES	80
5.1 EXPERIMENTAL VALIDATION.....	80
5.2 TRUNNION FRICTION STUDY	96
5.2.1 <i>Friction Sensibility Analysis</i>	96
5.2.2 <i>Unsymmetrical friction in trunnion pins</i>	103
5.3 PARAMETRICAL ANALYSES.....	109

5.3.1	<i>Unsymmetrical lifting cables</i>	109
5.3.2	<i>Limit cases</i>	114
6	CONCLUSIONS AND RECOMMENDATIONS	118
6.1	CONCLUSIONS.....	118
6.1.1	<i>Design Consideration of the Carlyle tainter gate</i>	118
6.1.2	<i>Experimental Procedure</i>	119
6.1.3	<i>Computational Study of the Tainter Gate</i>	119
6.1.4	<i>Experimental Validation, Trunnion Friction Study and Parametrical Analyses</i>	120
6.2	RECOMMENDATIONS	120
APPENDIX A. LIMITING WIDTH-THICKNESS RATIOS FOR COMPRESSION ELEMENTS.....		125
APPENDIX B. LIMIT STATES CALCULATIONS FOR GIRDER W36X170		127
APPENDIX C. LIMIT STATES CALCULATIONS FOR STRUT ARM W14X13		131

Table List

Tables	Page
Table 1: Section and material properties for the W36x170	28
Table 2: Limit length for the bottom horizontal girder	30
Table 3: Flange and web compact verification	31
Table 4: Section and material properties for W14x132	35
Table 5: Maximum and Minimum Principal Stresses for the Diagonal Bracing (DB)	102
Table 6: Maximum and Minimum Principal Stresses for the Bottom Strut (BS).....	102
Table 7: Minimum principal stresses for different friction coefficients	103
Table 8: Minimum Principal Stresses for the different friction coefficients analyses.....	106
Table 9: Principal Stresses for the Diagonal Bracing and the Bottom Strut.....	115

Figure List

Figures	Page
Figure 1: Hoisting cable from Carlyle tainter gate. Picture from the experimental procedures performed by Dr. Gopalaratnam and Dr. Riveros in Carlyle Lake Dam.	2
Figure 2: Lifting mechanism from 3D numerical model created in Abaqus CAE v6.10.	3
Figure 3: Principal structural components of a tainter gate from 3D numerical model created in Abaqus CAE v6.10.	3
Figure 4: Initial point of failure. Picture taken from Forensic Report on Spillway Gate3 Failure, Folsom Dam.	5
Figure 5: Failure on tainter gate in Folsom Dam, CA. Picture from Forensic Report Spillway Gate 3 Failure Folsom Dam, Bureau of Reclamation Mid-Pacific Region, 1996.	6
Figure 6: Trunnion pin-hub configuration	11
Figure 7: Strut arm deflection along the x-axis due to trunnion friction moment	11
Figure 8: Reaction forces in the pin	12
Figure 9: Phases for the 2D design. Picture from 3D numerical model created in Abaqus CAE v6.10.	17
Figure 10: Section diagram for the skin-plate	20
Figure 11: Top view of a girder-strut section of a tainter gate.	23
Figure 12: Trunnion assembly. Figure from EM 1110-2-2702.	25
Figure 13: Trunnion assembly of the Carlyle Tainter gate. Picture from experimental procedures performed in Carlyle Lake Dam by Dr. Gopalaratnam and Dr. Riveros.	26
Figure 14: Reactions acting on the bottom horizontal girder. Drawing from Carlyle Dam Design Memorandum, 1960	28
Figure 15: General available flexural capacity for beams	29
Figure 16: Moment diagram for girder W36x170. Drawing from ETABS v9.1.4.	32
Figure 17: Maximum moment at mid-span in beam W36x170. Figure from ETABS v.9.1.4.	32
Figure 18: Shear diagram for girder W36x170. Drawing from ETABS v9.1.4.	34
Figure 19: Maximum shear located at the support of the girder	34
Figure 20: Required axial force for the bottom strut W14x132	37
Figure 21: Maximum moment about the major axis for the section W14x132.	38
Figure 22: Maximum moment about the minor axis for the W14x132	39
Figure 23: Reactions generated in the pin	40
Figure 24: Reaction in the pin due to dead and hydrostatic load, and cable pressure.	40
Figure 25: Carlyle Lake Dam. Picture from Dr. Gopalaratnam and Dr. Riveros experimental procedure	42
Figure 26: Carlyle tainter gate components. Picture from Dr. Gopalaratnam and Dr. Riveros' experimental procedure in Carlyle Lake Dam.	43

Figure 27: Clamp-on transducers placed in the gate for strain measurements. Picture from Dr. Gopalaratnam's presentation "Strain Measurements and Numerical Investigation of Tainter Gate Operations"	44
Figure 28: MTS testing Machine. Picture from Dr. Gopalaratnam's presentation "Strain Measurements and Numerical Investigation of Tainter Gate Operations".	45
Figure 29: Location of the transducers in the Carlyle Tainter Gate. Picture from the experimental procedure performed in Carlyle Lake Dam by Dr. Gopalaratnam and Dr. Riveros.	45
Figure 30: Installation challenges. Picture form experimental procedures performed by Dr. Gopalaratnam and Dr. Riveros in Carlyle Lake Dam.....	46
Figure 31: Displacement Elevation vs. Time plot	47
Figure 32: Gage location and nomenclature. Picture from Gopalaratnam’s presentation “Strain Measurements and Numerical Investigation of Tainter Gates Operations”.	48
Figure 33: Typical Results, Top Struts Gages	50
Figure 34: Cross section strain diagram for top strut arms	51
Figure 35: Strain diagram for left top strut when the gate starts to open.....	53
Figure 36: Typical Results, Bottom Strut Gages	54
Figure 37: Cross section strain diagram for top strut arms	55
Figure 38: Typical Results, Diagonal Bracings	57
Figure 39: Cross section strain diagram for diagonal bracings.....	58
Figure 40: Typical Results, Diagonal Bracings close to Skin-Plate	59
Figure 41: Cross section strain diagram for diagonal bracings closer to the skin-plate	60
Figure 42: Computational modeling and simulation flowchart.	62
Figure 43: Deformable solid pin inside tainter gate’s hub.....	63
Figure 44: (a) Mesh for the shell elements of the gate. (b) Mesh for the solid elements of the pin. Picture from the 3D numerical model in Abaqus CAE v.6-10.....	65
Figure 45: Nonlinear response of a structure subjected to a small load	70
Figure 46: Water elevation in experimental procedure. Picture from the experimental procedures performed by Dr. Gopalaratnam and Dr. Riveros in the Carlyle Lake Dam.	73
Figure 47: Load schematic (a) static case, (b) kinetic case.....	76
Figure 48: Friction Force vs. Applied Force.....	77
Figure 49: Coulomb friction model, from Abaqus Documentation.....	78
Figure 50: Experimental Results vs. Numerical Analysis from the Left Top Strut Arm Gages. .	81
Figure 51: Simulation of the lifting of the gate.....	82
Figure 52: Experimental Results vs. Numerical Analysis from the Right Top Strut Arm Gages	83
Figure 53: Cross section strain diagram from numerical analysis for top strut arms	85
Figure 54: Experimental Results vs. Numerical Analysis from Left Bottom Strut Arm Gages...	86
Figure 55: Experimental Results and Numerical Analysis from the Right Bottom Strut Arm Gages.....	87
Figure 56: Water elevation for the experimental procedures.....	88
Figure 57: Cross section strain diagram from numerical analysis for bottom strut arms	89
Figure 58: Experimental Results and Numerical Analysis for the Left Diagonal Bracings.	90
Figure 59: Experimental Results and Numerical Analysis for the Right Diagonal Bracings.....	91

Figure 60: Cross section diagrams from numerical analyses results for the diagonal bracings ...	92
Figure 61: Experimental Results and Numerical Analysis for the Left Diagonal Bracings closer to the Skin-plate	93
Figure 62: Experimental Results and Numerical Analysis for the Right Diagonal Bracings closer to the Skin-plate	94
Figure 63: Cross section strain diagram from numerical analyses for diagonal bracings closer to the skin-plate.....	95
Figure 64: Friction sensibility study for gages 1 and 4.....	97
Figure 65: Friction sensibility study for gages 5 and 7.....	98
Figure 66: Von Misses stresses when the gate is stopped at 16.8-in	99
Figure 67: Stress configuration in the critical end frame members when the gate is lifted.....	100
Figure 68: Points where the principal stresses were taken.	101
Figure 69: Different friction coefficient plots for top strut gages.....	104
Figure 70: Different friction coefficient plots for bottom strut gages.	105
Figure 71: Stresses in the analysis with $FC_{left}=0.3$ and $FC_{right}=0.1$	107
Figure 72: Stresses in the analysis with $FC_{left}=0.1$ and $FC_{right}=0.3$	108
Figure 73: Effects of unsymmetrical loading in the left top strut	110
Figure 74: Effects of unsymmetrical loading in the right top strut.....	111
Figure 75: Effects of unsymmetrical loading in the left bottom strut.....	112
Figure 76: Effects of unsymmetrical loading in the right bottom strut.....	113
Figure 77: Strain vs. Time plot for DB	116
Figure 78: Strain vs. Time for BS.....	117

1 INTRODUCTION

In 1995, a tainter gate in the Folsom Dam, California failed releasing an overflow of water and endangering the nearby locations. Studies proved that the cause of failure was an increase in trunnion friction which generated a moment in the weak axis of a strut arm that was not considered in the original design. Tainter gates designed prior to 1960 are characterized by this practice. For this study a 3D numerical model of a tainter gate is going to be created using finite element analysis software, Abaqus v.6-10, and validated with experimental data from tests performed in a tainter gate located in the Carlyle Dam, Illinois. A friction sensibility study is going to be performed with the purpose of studying the effects of trunnion friction in the elements of the structure and analyze the distribution of stresses.

1.1 Introduction to tainter gates

Tainter gates are considerably large structures design for navigation and flood control purposes. This type of gate consists of a cylinder segment built up on radial arms that rotate on trunnions, which are attached to piers (Headquarters, U.S. Army Corps of Engineers, 2000). Tainter gates are controlled by hoisting cables (Figure 1) that are attached to a lifting mechanism located near the edges of the bottom of the skin plate (Figure 2). The hoisting cables are used to lift and lower the gate to permit the flow of water. These gates were developed by Jeremiah Burnham Tainter, an engineer and inventor from Wisconsin. The design is a modification of a previous model that was adjusted to make the structure simpler and more efficient than the original design. The primary components of a tainter gate are the skin-plate assembly, the strut arms, and the trunnion area. The skin-plate is stiffened by a series of vertical tee sections also

known as ribs (Figure 3a). The ribs connect to the horizontal girders that support the strut arms of the gate (Figure 3b), which at the same time are attached to the trunnion area (Figure 3c). The skin plate receives the loads from the hydrostatic and the hoist cable pressure and transfers it through the struts into the trunnion, which serves as a pivot point to rotate the gate. Additionally, the skin plate has a convex geometry on the upstream so that the rush of water would help open and close the gate. The strut bracings support the struts by shortening the un-brace length, thus reducing their vulnerability to fail by buckling.



Figure 1: Hoisting cable from Carlyle tainter gate. Picture from the experimental procedures performed by Dr. Gopalaratnam and Dr. Riveros in Carlyle Lake Dam.

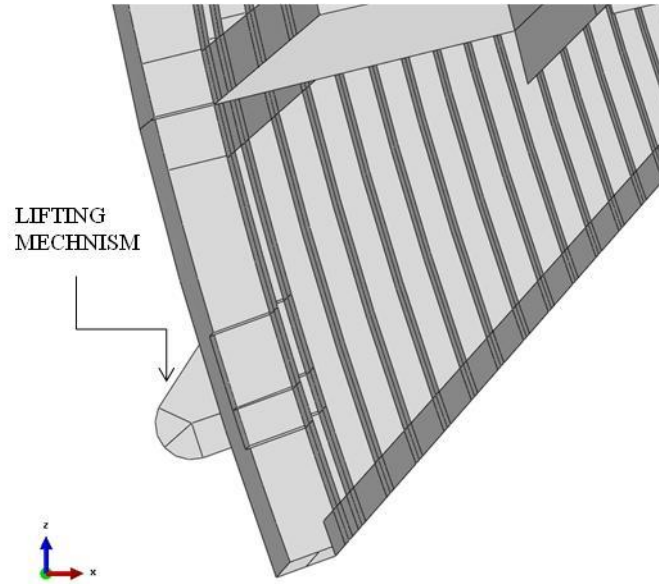


Figure 2: Lifting mechanism from 3D numerical model created in Abaqus CAE v6.10.

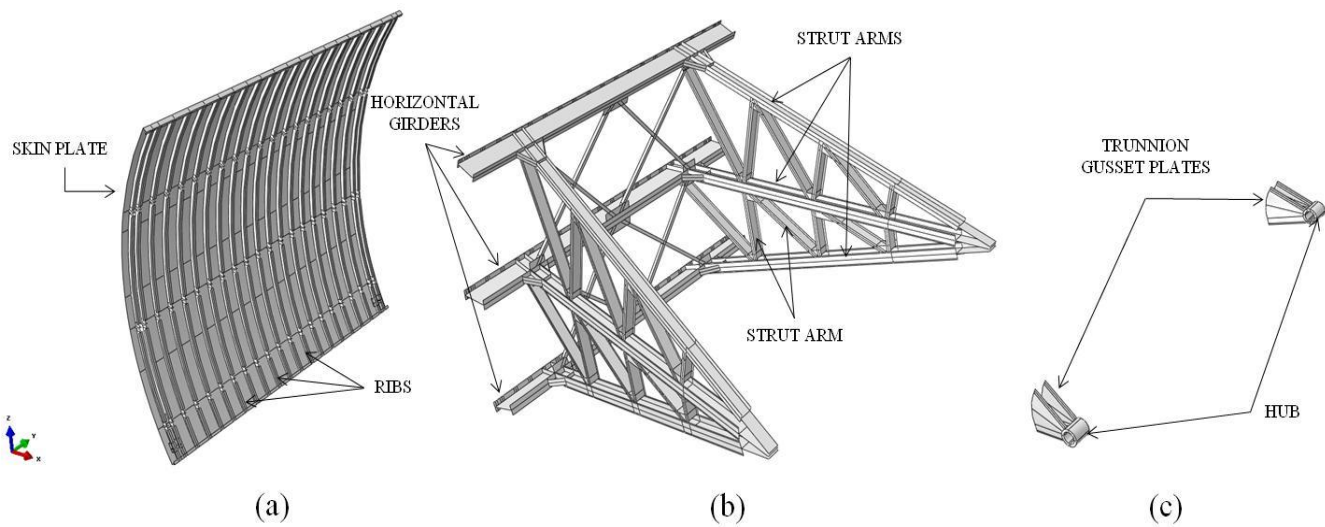


Figure 3: Principal structural components of a tainter gate from 3D numerical model created in Abaqus CAE v6.10.

Because of the effective geometry and performance of this type of gate they are commonly used in locks, dams, and reservoirs. The main purposes of these gates are to maintain a minimum of 9 feet of draft in navigation projects, to increase the storage capacity in a reservoir (flood control), and to divert water for irrigation, among others.

Around more than 75% of the major water control facilities in North America are employed by tainter gates, including famous dams as Grand Coulee and Chief Joseph (Daleo, 1976). Both of these dams are located on the Columbia River with the purpose of power generation and irrigation.

1.2 Motivation

On July 17, 1995, Spillway Gate No. 3 in Folsom Dam, California (Figure 5), failed during a weekday morning operation with a nearly full reservoir. The gate was being opened to maintain the flow in the river during a power plant shut down (Bureau of Reclamation Mid-Pacific Region, 1996). Even though the collapse affected only park areas around the flood channel of the American River and did not cause any loss of life, this failure created an awareness of the consequences of a similar type of failure in a highly populated area.

A multi-disciplinary forensic team of professionals attributed the structural failure to trunnion friction moment, which is the product of the force generated by the friction and the pin radius. The team performed an examination which determined that the initial point of failure was a diagonal brace joint 3E close to the trunnion area (Figure 4). Consequently, the diagonal brace 3E-4E failed leaving Strut 4 without bracing, thus increasing the slenderness ratio (kl/r) for the weak axis. The increase in the un-braced length of the strut caused a downward buckling of the

Strut 4, then Strut 3 and subsequent collapse of the structure (Figure 5). All of the strut braces initially failed in tension by shearing the $\frac{3}{4}$ -inch-diameter bolts at one of the attachment plates for each brace (Bureau of Reclamation, 1996).

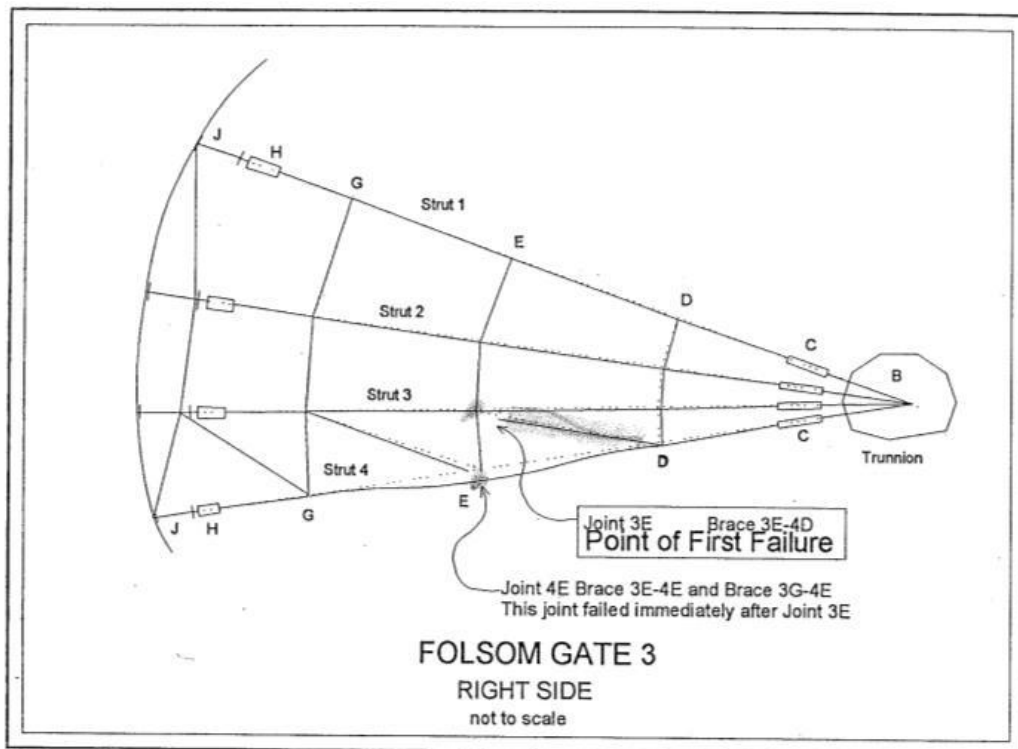


Figure 4: Initial point of failure. Picture taken from Forensic Report on Spillway Gate3 Failure, Folsom Dam.



Figure 5: Failure on tainter gate in Folsom Dam, CA. Picture from Forensic Report Spillway Gate 3 Failure Folsom Dam, Bureau of Reclamation Mid-Pacific Region, 1996.

Folsom Dam was designed and constructed between 1948 and 1956 by the US Army Corps of Engineers, Sacramento District. After the construction, it was transferred for maintenance to the Bureau of Reclamation Mid-Pacific Region. Before the failure there was no sign of structural problems, but there was a concern about the rusting of the members for the six years prior. After the failure, an intensive inspection revealed that a lot of the welds and bolts were severely damaged by corrosion. However, the forensic team determined that this was not the principal cause of failure. Another particular observation was the marking of the wall plates that indicated a lateral movement of the gate. This behavior could be attributed to a non-uniform friction at the pins or asymmetric loads. All these deficiencies found in the Folsom Dam gate make this study essential for the understanding of the state of stresses generated by trunnion friction and the numerical validation of the design manuals.

After all the studies were performed the forensic team determined that the two main causes of failure of the Folsom Dam tainter gate were the insufficient stiffness and strength in the critical structural members and the increase in trunnion friction. The original design of the gate complies with the requirements of the existing standards at the time but it did not consider the strut brace loading caused by the trunnion friction, therefore it does not meet the current design standards in which the trunnion friction load is considered. The omission of the trunnion friction load resulted in under-sizing of the strut and brace members. The Folsom Dam tainter gate was modeled using finite element analysis and it was determined that with its original design the gate would fail at a coefficient of trunnion friction of 0.22 to 0.28, current design standards by the Reclamation and by the Corps of Engineers require a minimum coefficient of friction of 0.3 for steel pins on bronze bushings. From the original calculations, the loads considered for the design of the struts were the dead load and the axial live loads generated by the hydrostatic and cable pressures. The trunnion friction was only considered for the hoist system and it was assigned a value of 0.2. For the design of the strut bracings moment distribution techniques were not used to determine loads and moments and truss action of the bracing was neglected. The brace member sizing was based on experience rules for area and slenderness ratios. Their purpose was only to limit weight deflection and reduce slenderness ratios of each individual strut member. A good engineering practice is to match the joint strength to the structural member capacity.

From the studies performed in Gate 3 of the Folsom Dam, it was determined that the right pin had approximately 50% more corrosion than the left pin. Therefore a bigger load was applied to the right strut, where the gate failed. Water gets into the trunnion pin in the gap between the hub and the bearing deteriorating with time the steel surface. When water reacts with the steel surface creates rust in the loaded side of the pin increasing the friction between the two surfaces.

The reason why rusting occurs only in the loaded side is because is where the lubricant film is the thinnest. This area is called Boundary Lubrication, where bearing surfaces are separated by a film of molecular thickness in which metal-to-metal contact is made by the asperities of the surfaces (F.F. Ling et al, 1969). Water can enter between the pin and the hub by capillary action through the thin film and small spaces. If the reservoir level is below the spillway water and air can get pushed in by atmospheric pressure. When metal-to-metal contact occurs with water or contaminant acting as an electrolyte it produces a galvanic reaction which causes corrosion.

Twenty eight years prior to the Folsom Dam tainter gate collapsed there was another known failure of a tainter gate in Wachi Dam, Japan on July 1967. This failure caused a swept of the gate along with the bridge over it of 41.5 ft downstream of the gate bay (Ishii et al., 2009). Ishii and Anami, professors of mechanical engineering in Osaka Electro-Communication University and Ashikaga Institute of Technology respectively have dedicated years to the study of the failure of these structures. They attribute both failures to a dynamic instability mechanism that all tainter gates possess. This phenomenon can be described as a self excited vibration instability caused by the damping of the water in the upstream side of the gate, flow of water under the gate, sliding of the side seals against the stainless steel wall plates and friction between the pin and the hub (Todd, 2005).

Tainter gates are steel structures that are exposed to rough environmental conditions including constant exposure to water, rain and in some cases snow. In order to ensure dam safety it is important to maintain these structures in good conditions and rehabilitate the ones that present hazard to their surroundings. Since most of these structures were design and constructed by the 1960's many of them lack of the correct design and are considerably deteriorated. The Folsom Dam failure created conscience of this problem and that is why a detailed investigation

should be performed to determine how these structures can be rehabilitated. Even though retrofit operations are being applied to several gates to strengthen their end frame members, it is important to have a better understanding of the trunnion friction phenomenon to avoid future failures and to ensure safe operations in tainter gates under extreme loading events and conditions.

1.3 Problem Description

On those tainter gates designed prior to 1960 the moment generated by the increase in trunnion friction in the weak axis of the strut arms was not taken into consideration. This is a critical parameter because these metallic structures are constantly exposed to water. Corrosion and deterioration provokes an increment in the coefficient of friction between the pin and the hub causing an increase in the loads of the structural members. This phenomenon is difficult to assess because the pin is fully covered by the hub casting. When these loads exceed the capacity of the structure it becomes more susceptible to failure.

For the design of the strut arms of the tainter gate structures, the demand/capacity equation 1.1 was employed applying the Allowable Stress Design method. This equation combines the axial and flexural forces.

$$f_a/F_a + f_{by}/F_{by} + f_{bz}/F_{bz} \leq 1.0 \quad 1.1$$

Where,

f_a = required axial stress at the point of consideration, ksi

F_a = available axial stress at the point of consideration, ksi

f_{by}, f_{bz} = required flexural stress at the point of consideration, ksi

F_{by}, F_{bz} = available flexural stress at the point of consideration, ksi

y = subscript relating symbol to major principal axis bending

z = subscript relating symbol to minor principal axis bending

Even though this equation is under the unsymmetrical members subjected to flexural and axial force section of the AISC Manual 13th ed., it can be applied to any shape member. This equation takes into consideration three parameters: axial load, strong axis moment and weak axis moment. The struts are treated as beam-columns having a compressive force or axial load and flexural moments, which are the product of the hydrostatic pressure, combined with the pressure that exerts the lifting cables. The bracings that were placed between the struts restrict the weak and the strong axis generating moments.

The trunnion consists of a cylindrical pin surrounded by a hub (Figure 6). Between these two surfaces normal and shear stresses are generated. The weak axis moment in the strut is generated by the friction between the pin and the hub as the hub rotates to lift or lower the gate and the pin stays fixed. Figure 6 illustrates a simple configuration of the moment, M_f , generated between the pin and the hub surfaces. The magnitude of the moment, M_f , will be the product of the friction force by the distances between the center of the pin and the surface which will be the radius. Therefore the greater the radius, the bigger the resultant moment will be. This was a factor that was not considered in the original designs.

$$M_f = F_f \times d \quad 1.2$$

Where,

d = distance between the center of the pin to the edge of the pin, in

F_f = friction force generated by the contact between the pin and the hub, kip

M_f = moment generated by the friction between the pin and the hub, kip-in

In the 1950's Crest and Head Gates engineering manual was mentioned that as the depth of the weight increases, supporting a greater hydrostatic load, the turning radius of the pin must also be increased. The document does not advise that with a bigger turning radius a greater moment can be generated.

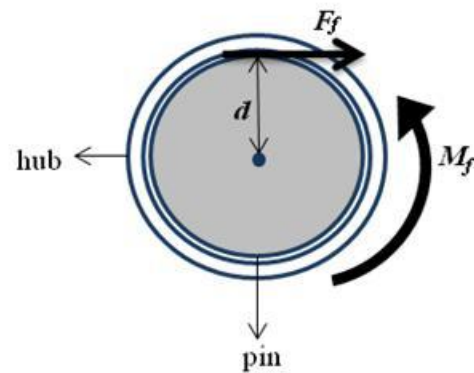


Figure 6: Trunnion pin-hub configuration

Figure 7 illustrates how the generated moment affects the strut arm in its weak axis making it bend along the x-axis.

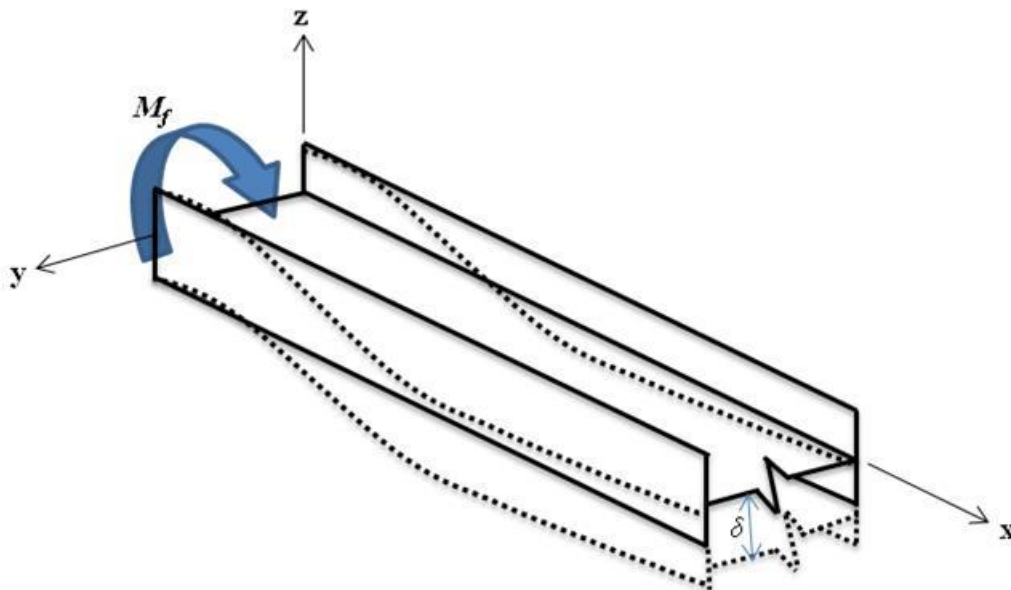


Figure 7: Strut arm deflection along the x-axis due to trunnion friction moment

The trunnion pin has a total of three global components, R_x , R_y and R_z , which are parallel to the global X, Y, and Z axes (Figure 8). Components X and Z lead to a resultant force R which exerts pressure directly on the trunnion pins. This pressure leads to a friction force, F_f , around the trunnion pin in a direction perpendicular to R (Emkin, 1976). This friction force is the one that generates a moment in the weak axis of the strut arm (Figure 7).

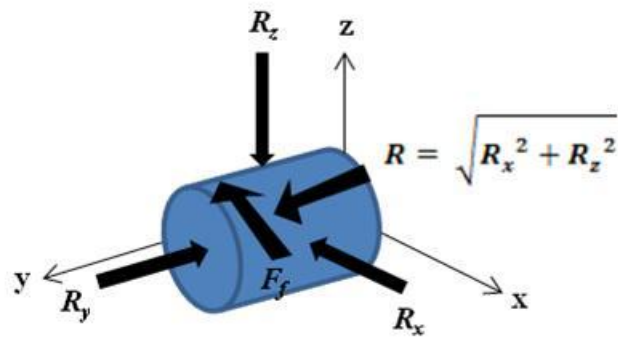


Figure 8: Reaction forces in the pin

In 2008 Dr. Gopalaratnam from the University of Missouri-Columbia and Dr. Riveros from the U.S. Army Engineering Research and Development Center performed a series of tests on a tainter gate located in Carlyle Dam, Illinois. This gate has similar characteristics to the tainter gate that failed in Folsom Dam and was also design prior to 1960. From the Carlyle Dam Design Memorandum the frame design section presents in detail the parameters consider for the design of the strut arms. After calculating the reactions and moments in the struts due to the different load cases the controlling one was taken, which was the water load only. With these parameters the required axial and flexural stresses were computed. Only the maximum moment about the strong axis was calculated. The weak axis moments was taken to be zero, making $f_{bz}/F_{bz} = 0$ in the design equation. For the actual case the parameter was not zero, therefore the

resultant from the equation may be greater than the one for gates with slender strut arms, consequently exceeding the capacity of the member.

1.4 Objectives

The main objective of this research effort is to enhance the efficiency of the tainter gates by studying the stress-strain behavior due to external loads and the increase in moment due to friction in the trunnion area. To achieve this purpose it is necessary to fulfill the following criteria:

- Verify the capacity of the principal members of the Carlyle Lake Dam tainter gate for the actual loads acting on the structure.
- Develop a three-dimensional (3-D) finite element model of the Carlyle Dam Tainter Gate, which represents the Corps of Engineers standard tainter gates.
- Validate the model with existing experimental data.
- Evaluate the resulting forces and their distribution among the different structural components for different magnitudes of trunnion friction.
- Study the effects of different friction coefficients in each trunnion and how it affects the stress behavior in the structural members.
- Study the effects of asymmetric loading due to the lifting cables.
- Study the limit cases (gate empty and completely under water) for the gate under normal operation.

1.5 Scope of Work

Around 50 percent of the tainter gates were designed without considering trunnion friction as a design load. The methods that currently are considered the best to determine the coefficient of friction in the trunnion have shown a margin of error between 15 and 30 percent; therefore a better method of determining the trunnion friction coefficient is essential (Riveros, 2006). The failure of the Folsom Dam spillway gate focused a significant amount of attention on the forces generated by the trunnion friction, especially in those cases for which maintenance has not been performed regularly or was performed ineffectively, and when severe loading events occurred. This research will study the different measuring methods developed to determine trunnion friction and establish their advantages and disadvantages to provide a better understanding and help in the development of this new methodology. The study will use state-of-practice 3D modeling techniques on standard tainter gates where experimental data is available.

To obtain a better understanding of the behavior of the different types of tainter gates, it is necessary to perform a literature review about the design and performance of these structures and the difficulties they have encounter through the years. The investigation will emphasize the dam structures operated by the U.S. Army Corps of Engineers as well as other government agencies, but it would also review literature available in the public domain on similar structures worldwide.

Previous experimental procedures to measure trunnion friction and guidance in EM 1110-2-2702 show that with the measurement of the strains on the end frame member, the loads of the hoist cables, and the measurement of the position of the gate, friction parameters and loads on the gate during routine operation can be calculated (Golpalaratnam, 2007). For an accurate approximation of the stresses in the members it is necessary to perform a 3-D finite element

analysis. Additionally a good first order model would be useful to compute friction coefficients from experimental results and facilitate performance evaluation. The numerical model of the Carlyle tainter gate will be used to perform improvements in the design of the structural members. These numerical simulations will also provide the capability of performing parametric analysis of different configurations of trunnion geometry and friction coefficient.

1.6 Overview

The description of the tainter gate mechanism demonstrates that the trunnion area is one of the most important parts of the structure. This research project intends to investigate the effects of the trunnion friction in the structural components of a tainter gate to obtain the optimum hub-pin dimensions that will produce the minimum flexural stress and thus the most efficient operation.

This research study is divided in 6 chapters. The first chapter is an introduction to tainter gates including their background and problem description. Chapter 2 discusses the design features and considerations of this type of structure and includes an evaluation of two of the principal member of the Carlyle Lake Dam tainter gate. Chapter 3 explains the experimental procedure that was performed on the Carlyle Lake Dam in 2008 by Dr. Golpalartnam and Dr. Riveros. Chapter 4 presents the computational modeling and simulation of the 3D numerical model of the tainter gate. Chapter 5 includes the validation of the 3D numerical model, the trunnion friction investigation performed on the gate and the parametric analyses. Chapter 6 gives the conclusion from the study and recommendations for further research.

With this research it is intended to validate the Carlyle tainter gate, which has a geometry that can be generalized to any radial gate, analyze the behavior of each component when

subjected to internal and external loads and study how an increment in trunnion friction affects its performance.

2 DESIGN CONSIDERATIONS OF TAINTER GATES

The purpose of this chapter is to illustrate how a complicated structure with challenging geometric characteristics can be broken into pieces and analyzed as different basic structural members like beams, columns and frames. Also it is intended to evaluate the primary sections of the Carlyle Tainter Gate using the actual design codes.

2.1 General features of design

Depending on the purpose of the gate, its basic geometry will be different. For example, a typical spillway for a flood control project has the downstream support, or trunnion pin, located one third point of the height of the gate, as for a navigation project its trunnion support is located at a higher elevation (TGDA Workshop, 1976). The skin-plate configuration and the strut arms are the most critical sections which its geometry and design depends on the use and application of the gate.

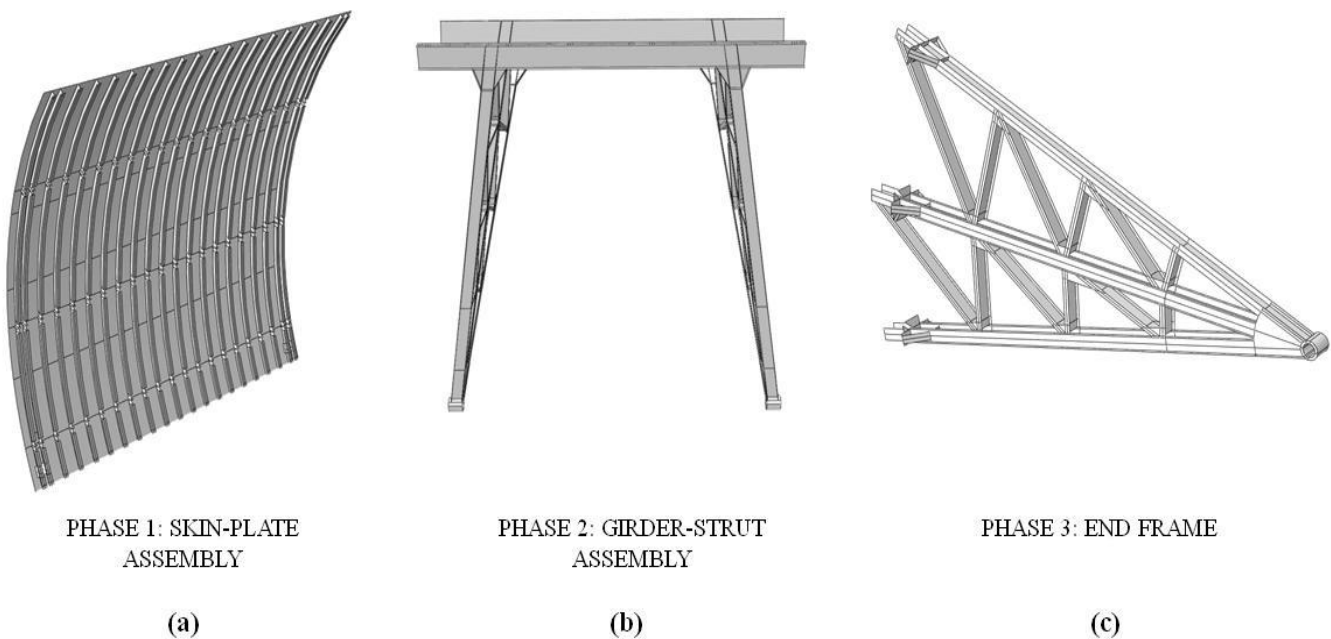


Figure 9: Phases for the 2D design. Picture from 3D numerical model created in Abaqus CAE v6.10.

Tainter gates are design using a simplify method that divides the structure in a two dimensional analysis in which each structural member is designed separately but taking into consideration the forces and reactions of the adjacent members. The primary gate components are the skin-plate assembly, the horizontal girders and the end frame, which contains the struts and its bracings and the trunnion bearing (Figure 3). Therefore the whole design can be divided into three phases, the skin-plate assembly (Figure 9a), the girder-strut frame assembly (Figure 9b) and the end frame (Figure 9c).

The 2-D approach can be used when the loading conditions have a symmetrical distribution, otherwise a 3-D analysis have to be perform. Unsymmetrical loading may occur when a lifting cable breaks or becomes loose making the total weight of the gate be supported by only one cable. Another case can be cause by the wedging along one of the side of the gate with the spillway pier. This resistance could cause the hoisting motor to develop a maximum torque increasing the tension in each cable. Both of these cases will make the gate sway towards a pier face provoking translation and twisting forces in the structure.

In the 1960s all the designs were based on the Allowable Stress Design. For the specific case of the Carlyle Dam Tainter Gates, its design was in accordance with the engineering manuals “Crest and Head Gates – Tainter Gates”, from November 1950 and “Working Stresses for Structural Design” from January 1958.

One of the general features of design mentioned in the document “Crest and Head Gates –Tainter Gates” is the emphasis in simplicity of framing, thus using a minimum number of members of heavier cross section as oppose to greater number of members with a lighter cross-section. This topic was later discussed in the Journal of the Power Division published by the American Society of Civil Engineers in 1962. This document states that a greater amount of

lighter elements, the arms and its bracings, can be built more economically and would have a greater resistance than a gate with less members of heavier cross-section because there will be more elements bracing the struts, therefore reducing its un-brace length. The problem with this principle was the detailing that involves the construction of a gate with greater amount of elements.

Before the 1960's the radial gate design practice varied between entities within the Bureau of Reclamation. It was not until the late 1960's and early 1970's when computational techniques began to evolve through the use of computers that design standards began to unify (Bureau of Reclamation, 1996). An extract from a 1950's design standard illustrates the absence of induce trunnion moment in the design loads consideration: "The individual arm struts are primarily loaded as a column but also carry high secondary stresses induced by the angular rotation of the joints" (Bureau of Reclamation, 1950) .

2.1.1 Skin-plate assembly

The skin plate assembly consists of a thin radial wall stiffened by vertical ribs along the width of the plate. For the design of the skin plate a 2-D approach is applied with the purpose of simplifying the model. One of the assumptions is that there is no curvature in the assembly. The skin plate acts both as a unity strip spanning along the width of the gate simply supported by the ribs (Figure 10) and as the upper flange of the T-sections ribs. The loads for the skin plate design are determined based on a unit width of plate and for the rib model the magnitude for the loads is determined based on the tributary area of the rib. Different hydrostatic pressures are considered depending on the headwater level to determine the changing point where the thickness of the

skin-plate has to be increased or reduced. Due to the varying loading on the skin plate it is more cost effective for a gate higher than 10ft to vary the thickness of the plate along the height of the gate. In the case of gates with wire ropes it is required to add a thicker plate to support the extra pressure of the cables. The designs of the skin plate and the vertical ribs are interconnected. The skin plate thickness depends on the rib spacing and the rib size depends on the skin plate thickness.

Considering the skin-plate as a continuous member spanning horizontally with ribs as vertical support:

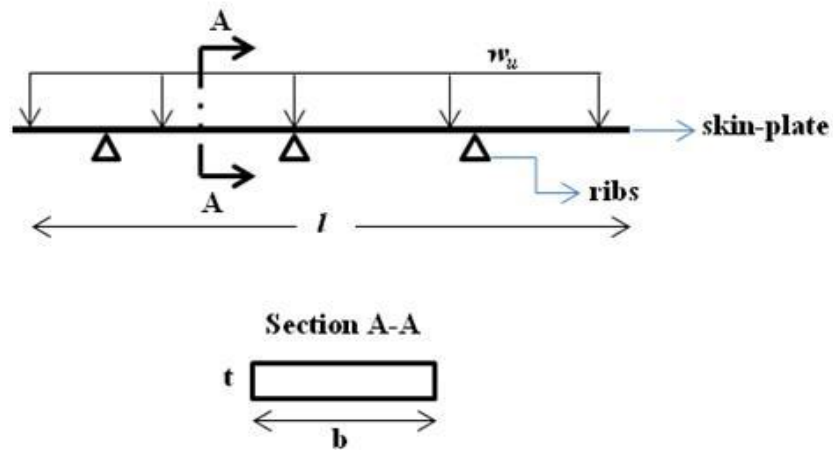


Figure 10: Section diagram for the skin-plate.

Where,

w_u = distributed ultimate load, kip/in

l = width of the skin-plate, in

t = thickness of the skin-plate, in

b = unitary width of the skin-plate, in

The moment of inertia, I_x , for the Section A-A is

$$I_x = \frac{1}{12}bt^3 \quad 2.1$$

$$I_x = \frac{1}{12}t^3, \text{ for } b = 12\text{in}$$

$$c = t/2 \quad 2.2$$

Therefore,

$$S_x = \frac{I_x}{c} = 2t^2 \quad 2.3$$

The capacity of the continuous member is

$$\sigma_n = \phi_b \alpha F_y \quad 2.4$$

and the stresses acting on the member

$$\sigma_{acting} = \frac{M_u}{S_x} \quad 2.5$$

Where,

I_x = moment of inertia about the principal axis, in⁴

S_x = elastic section modulus taken about the principal axis, in³

ϕ_b = resistance factor for flexure

α =

F_y = specified minimum yield stress, ksi

M_u = ultimate moment in the section, kip-in

σ_n = nominal stress capacity of the member, ksi

σ_{acting} = acting stress on the member, ksi

Solving for M_u

$$M_u = \sigma_{acting} S_x$$

Since $\sigma_{acting} \leq \sigma_n$,

$$M_u = \phi_b \alpha F_y \times 2t^2 [kip - in]$$

To determine a preliminary thickness of the skin-plate solve for t,

$$t = \sqrt{\frac{M_u}{2\phi_b \alpha F_y}} [in]$$

Where;

$$M_u = \frac{w_u l^2}{12}, \text{ only considering the hydrostatic load and}$$

$$M_u = \frac{w_u l^2}{12} + \frac{Pl}{8}, \text{ considering the hydrostatic load and the cable pressure load}$$

It is recommended that the vertical ribs be structural tee sections with the web welded to the skin plate. To determine the geometrical properties for the section an effective width, b_e , of the skin plate is assumed to act as an upstream flange.

For compact sections,

$$b_e = \frac{187t}{\sqrt{F_y}} \quad \mathbf{2.6}$$

and for non-compact sections,

$$b_e = \frac{255t}{\sqrt{F_y}} \quad \mathbf{2.7}$$

Where t is the thickness of the skin plate and F_y is the yield stress of the skin plate's material.

2.1.2 Girder-strut arm assembly

The second phase of the structural design is the girder frame model (Figure 9b). This part of the gate is design to provide support to the skin plate and to transfer the loads from the skin plate to the end frame. In a 2D-analytical model each horizontal girder acts as a beam and the connecting struts as columns, thus forming a one-story frame (Figure 11). The strong axes of the struts are oriented to resist flexural forces in the plane of the frame (EM 1110-2-2702). The loads acting on the girders are the reactions from the ribs; therefore the magnitude of the loads on each girder depends on its elevation. The end frame of the gate also affects the girder forces because they act as the supports of the frame system.

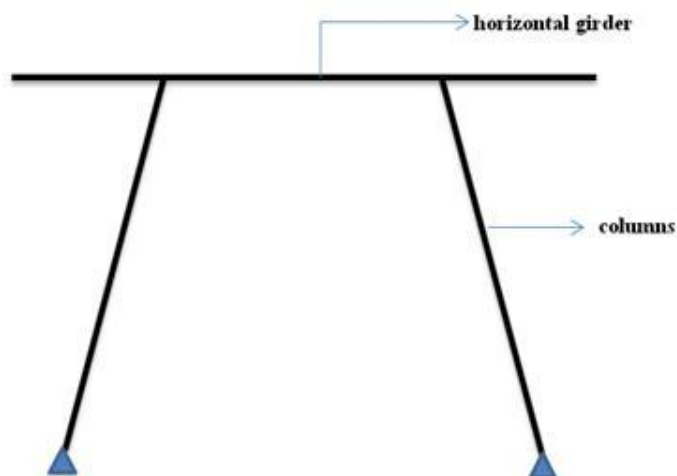


Figure 11: Top view of a girder-strut section of a tainter gate.

According to the 2000 Design Manual (EM 1110-2-2702), a maximum girder moment will be achieved if the struts are parallel to the pier face. To reduce the girder moments the struts should be inclined to redistribute the moments acting along the girder. A considerable reduction can be obtained if the struts intersect the girder at approximately one-fifth of the gate's width.

Revising the as-built drawings from the Carlyle Tainter gate, the design complies with the recommendations described above. The total width of the gate is 38ft and both struts intersect each girder at a distance of 7.5ft, which is one-fifth of the total width.

2.1.3 *End Frames*

The third phase of the structural design of the tainter gate is the end frame configuration (see Figure 9c). The end frame plays an important part in the design of a tainter gate, even though these elements are considered secondary members, depending in their configuration and connection details these bracings can carry a significant amount of loads and act as primary elements (EM 1110-2-2702).

The end frame consists of the strut arms and the strut bracings simulated as frame and truss elements. The model includes the skin-plate and girder geometry as rigid members just for load transferring purposes. The main objective of the end frame model is to determine the sill reaction load, the trunnion reaction and the end frame member forces. The most critical load cases are considered to determine the loads in the members, when the gate is closed, when the gate is fully open, and when the cables are lifting or lowering the gate. The boundary conditions also vary for each case. The trunnion is usually modeled as a pin, free to rotate with no translation. For the case where the gate is closed, the sill is modeled as a roller-pin free to translate tangent to the sill. The lifting cables are treated as loads acting on the skin plate.

2.1.4 Trunnion assembly

The trunnion assembly is located at the end of the gate and is the pivot point of the whole structure. In simple 2D-analysis it is modeled as the bottom boundary conditions of the struts as a pin, free to rotate but with no translation. Figure 12 illustrates the components of the trunnion assembly.

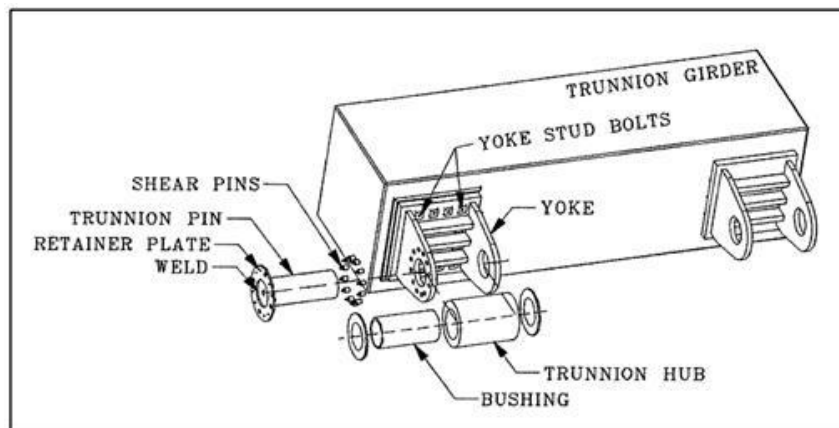


Figure 12: Trunnion assembly. Figure from EM 1110-2-2702.

The trunnion yoke consists of two structural steel plates that are welded to a base plate which is bolted to the trunnion girder. The pin, hub, and associated components are supported by the trunnion yoke. The struts are connected to the hub which receives the loads and transfer them to the pin. To allow a more distribution of stresses and to provide clearance for welding, the hub is design to be wider than the web of the strut arms. Inside the hub is a cylindrical bushing that minimizes friction and wear between the pin and the hub. The pin transfer the gate loads to the yoke plates connected to the base plate that is attached to the trunnion girder. A retainer plate is

welded to the pin to prevent it from rotating. Figure 13 illustrates the trunnion assembly of the Carlyle Tainter gate.



Figure 13: Trunnion assembly of the Carlyle Tainter gate. Picture from experimental procedures performed in Carlyle Lake Dam by Dr. Gopalaratnam and Dr. Riveros.

2.1.5 Friction Design Considerations

Tainter gates are designed such that all the applied forces would converge in a point thus making it easier to rotate. This pivot point in which the structure also rotates is the trunnion area, therefore it is important to preserve and maintain this region in good condition.

The revised design standards establish that the pin dimensions depends on the bearing pressure from the bearing or bushing and it's flexural and shear stresses must not exceed the allowable shear stresses. Another specification from the design requirements is that the pin must

contain a retainer plate and shear pins that will be design to carry frictional loads when the gate is raised or lowered (Headquarters, U.S. Army Corps of Engineers, 2000).

2.2 Carlyle Tainter Gate Evaluation

As an evaluation method two structural members from the Carlyle Dam tainter gate were analyzed using the AISC Manual 13th edition and the engineering software ETABS. The selected structural sections were the bottom horizontal girder, and the bottom left strut arm. They were chosen because the maximum hydrostatic pressures occur at the bottom of the gate. The idea of this evaluation is verify if the existing structural sections comply with the actual design codes. To compare the results with the original design the loads were taken directly from the Carlyle Dam Design Memorandum, 1960.

It is important to mention that the evaluation performed was a simplified 2D analysis assuming complete symmetry in the geometry and loading of the gate. Also it is assumed that both pins have the same coefficient of friction.

2.2.1 *Bottom Horizontal Girder Evaluation*

Since the horizontal girders can be analyzed as beams, a simple model was created using the engineering software ETABS to compute the shear and moment diagrams. The model consisted of a horizontal beam with two supports at a distance of one fifth of the total length of the beam from the edge of the element on each side as a representation of the strut arms. The gusset plates between the girders and the strut arms were also created by assigning roller

restrains in their respective location resisting the vertical movement of the beam. The loads acting on the beam are the resulting reactions from the ribs that are generated by the hydrostatic load and the cable pressure. Figure 14 illustrates the reactions used for the analysis. The figure shows only half of the section because it is symmetric along the center line.

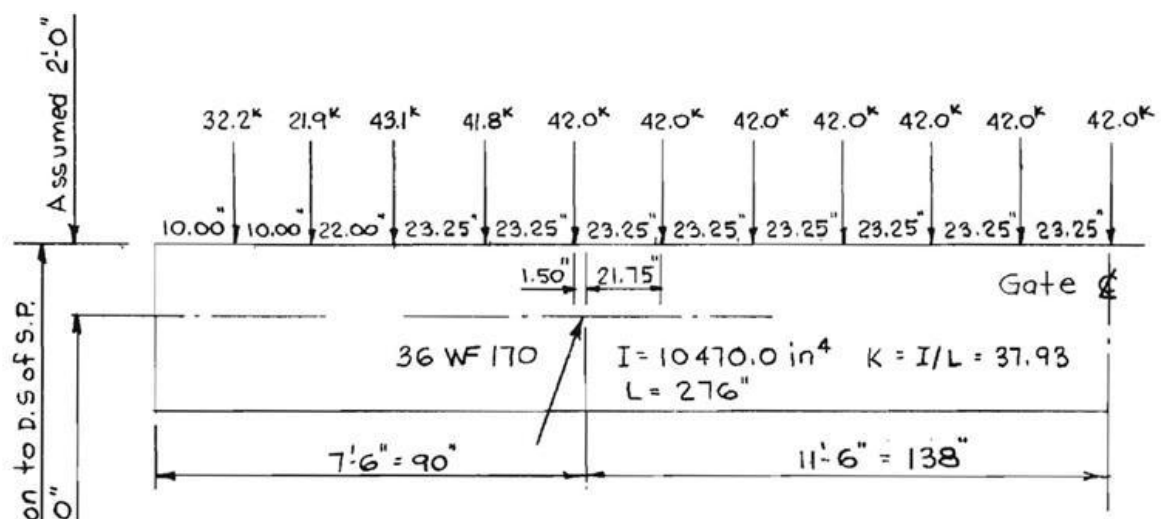


Figure 14: Reactions acting on the bottom horizontal girder. Drawing from Carlyle Dam Design Memorandum, 1960

The section under evaluation is the W36x170, which is the bottom girder of the Carlyle tainter gate. Table 1 illustrates the material and section properties of the girder.

Table 1: Section and material properties for the W36x170

W36x170 Section Properties			Material Properties		
$d =$	36.2	in	$F_y =$	50	psi
$t_w =$	0.68	in	$E =$	29000	psi
$r_y =$	2.53	in			
$I_y =$	320	in ⁴			
$C_w =$	98500	in ⁶			
$S_x =$	581	in ³			

$J =$	15.1	in^4
$h_o =$	35.1	in
$Z_x =$	668	in^3
$S_y =$	53.2	in^3
$Z_y =$	83.8	in^3

To determine the capacity of the strut the strength limit states yielding, lateral-torsional buckling and shear were calculated. The capacity of flexural members depends on the brace length because it will determine the equations to calculate the limit states. Figure 15 illustrates the corresponding moment capacity depending on the limit length range. L_b is the length between the brace points in the section, L_p and L_r are the limit lengths that determine the state of lateral torsional buckling in a section.

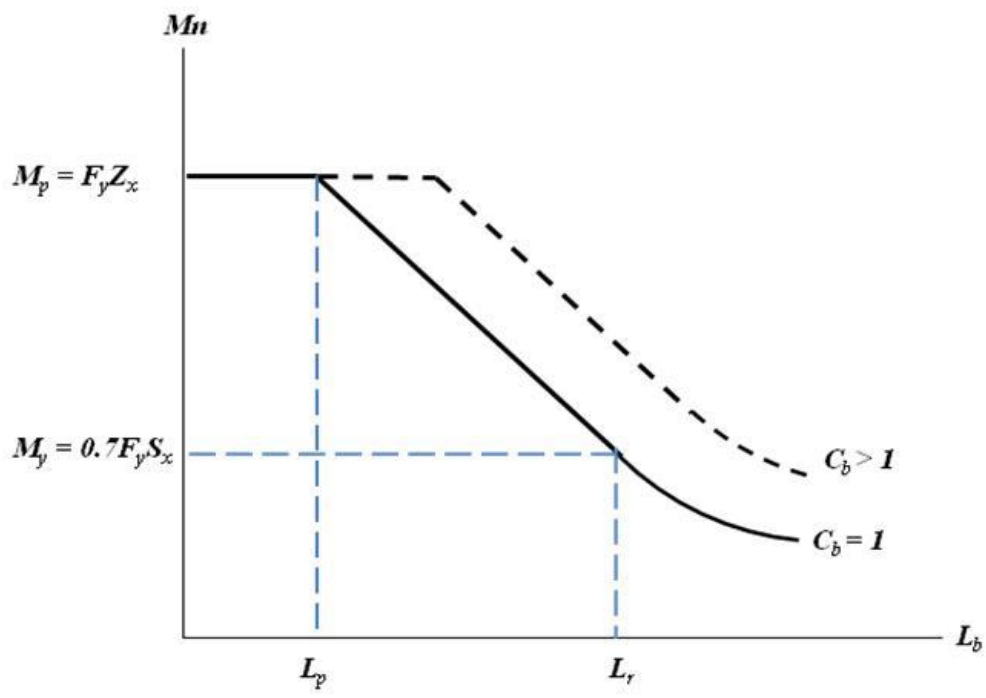


Figure 15: General available flexural capacity for beams

$$L_p = 1.76r_y \sqrt{\frac{E}{F_y}} \quad 2.8$$

$$L_r = 1.95r_{ts} \frac{E}{0.7F_y} \sqrt{\frac{Jc}{S_x h_0} \sqrt{1 + \sqrt{1 + 6.76 \left(\frac{0.7F_y S_x h_0}{E Jc} \right)^2}}} \quad 2.9$$

Where,

$$r_{ts}^2 = \frac{\sqrt{I_y C_w}}{S_x} \quad 2.10$$

Table 2 illustrates the calculation of the limiting lengths and $L_p < L_b < L_r$, therefore the flexural member is subjected to inelastic lateral-torsional buckling according to the Classification of Spans for Flexure Section of the AISC Manual 13th edition.

Table 2: Limit length for the bottom horizontal girder

Limiting Lengths		
$L_b =$	261.3	in
$L_p =$	107.24	in
$L_r =$	288.98	in

Before calculating the limit states it is also important to calculate the limiting width-thickness ratios for compression elements. The values for the width thickness ratios are taken from Table B4.1 (Appendix A) of the AISC Manual 13th ed. Table 3 show the calculations to determine that the flange and web are compact sections.

Table 3: Flange and web compact verification

Flange		Web	
$\lambda = b/t =$	5.47	$\lambda = h/t_w =$	47.70
$\lambda_p =$	9.15	$\lambda_p =$	90.55
$\lambda_r =$	24.08	$\lambda_r =$	137.27
compact		compact	

Where,

λ = width-thickness ratio of the section

λ_p = Compact limiting width-thickness ratio

λ_r = Non-compact limiting width-thickness ratio

Given that $\lambda < \lambda_p \leq \lambda_r$, for both the flange and the web of the section W36x170, they are both classified as compact. Since the section was compact in the web and the flange the local buckling verifications did not have to be computed. To verify that the section complies with the actual requirements the limit states for yielding, lateral torsional buckling and shear were calculated and compared with the ultimate capacity acting in the members.

(1) Verification for yielding

Since $L_b > L_p$

$$\phi M_n = \phi 0.7 F_y S_x \quad 2.11$$

The calculated $\phi M_n = 18,302$ k-in and the maximum moment acting on the beam is $M_{ult} = 13,799$ k-in. Since $\phi M_n > M_{ult}$ the girder section for the design loads complies with the yielding requirements. Figure 16 illustrates the moment diagram for the girder, where the maximum

moments are located at the supports of the member. Figure 17 illustrates the maximum value M_{ult} located at the mid-span of the beam.

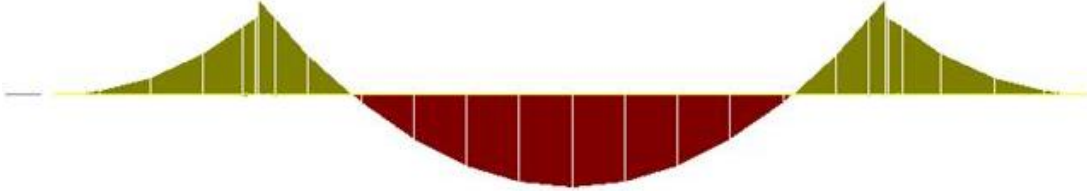


Figure 16: Moment diagram for girder W36x170. Drawing from ETABS v9.1.4.

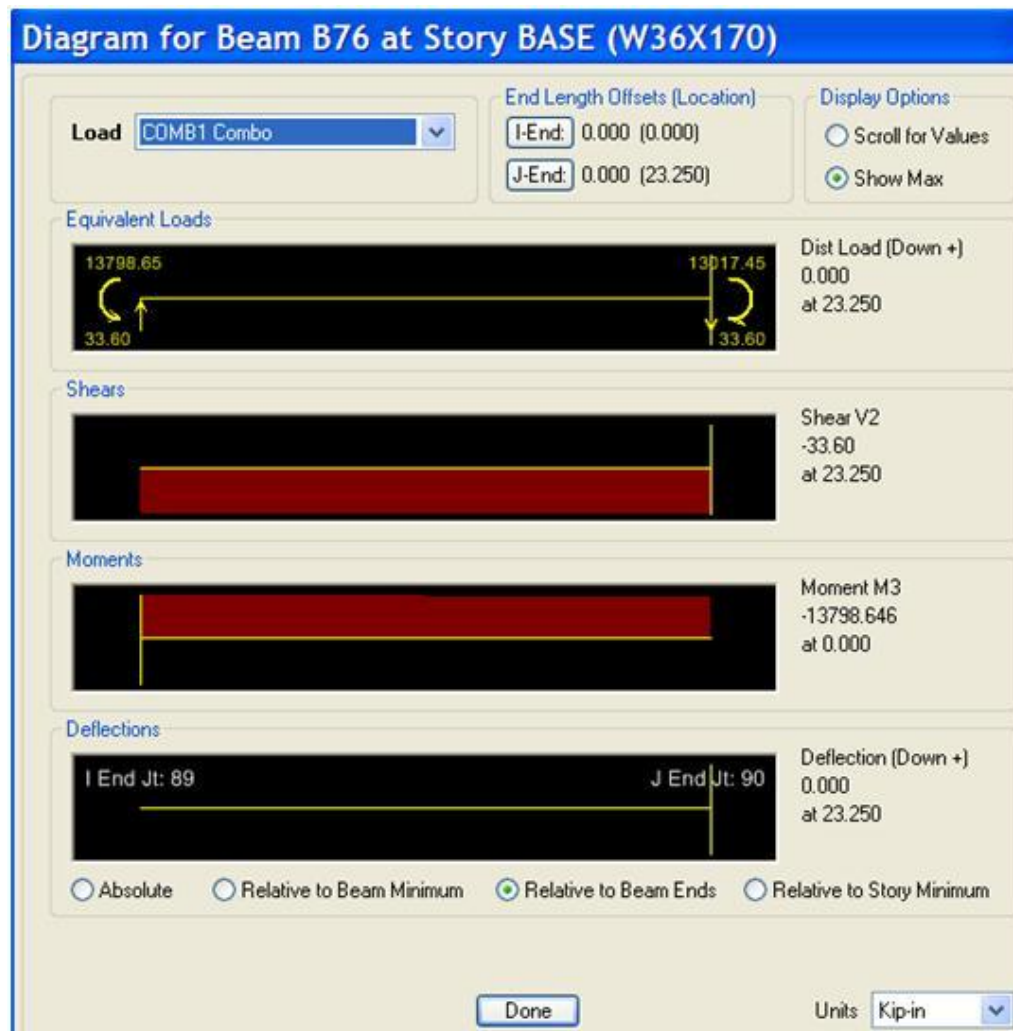


Figure 17: Maximum moment at mid-span in beam W36x170. Figure from ETABS v.9.1.4.

(2) Verification for lateral torsional buckling

Table 2 shows the values for the limit lengths of the girder under evaluation. Since the value of L_b is between L_p and L_r the capacity is

$$M_n = C_b \left[M_p - (M_p - 0.7F_y S_x) \left(\frac{L_b - L_p}{L_r - L_p} \right) \right] \quad 2.12$$

The calculated $\phi M_n = 23,032$ k-in that compared with the ultimate moment illustrated above $M_{ult} = 13,799$ k-in also complies with the lateral torsional buckling requirements.

(3) Verification for nominal shear strength

$$\phi V_n = \phi 0.6 F_y A_w C_v \quad 2.13$$

Where C_v is determine as follows;

$$\text{For } \frac{h}{t_w} \leq 1.10 \sqrt{\frac{k_v E}{F_y}}$$

$$C_v = 1.0$$

$$\text{For } 1.10 \sqrt{\frac{k_v E}{F_y}} < \frac{h}{t_w} \leq 1.37 \sqrt{\frac{k_v E}{F_y}}$$

$$C_v = 1.10 \frac{\sqrt{k_v E / F_y}}{h / t_w}$$

$$\text{For } 1.10 \sqrt{\frac{k_v E}{F_y}} < \frac{h}{t_w} \leq 1.37 \sqrt{\frac{k_v E}{F_y}}$$

$$C_v = 1.551 \frac{E k_v}{(h / t_w)^2 F_y}$$

The value of k_v for stiffened webs is

$$k_v = 5 + \frac{5}{a/h^2}$$

The obtained nominal shear strength $\phi V_n=665k$ which is greater than the ultimate shear from the ETABS analysis $V_{ult} = 369kip$ as illustrated in Figure 19, therefore the section complies with the nominal shear strength requirements. Appendix B illustrates in detail the calculations for the capacities for yielding, lateral torsional buckling and shear of the beam.



Figure 18: Shear diagram for girder W36x170. Drawing from ETABS v9.1.4.

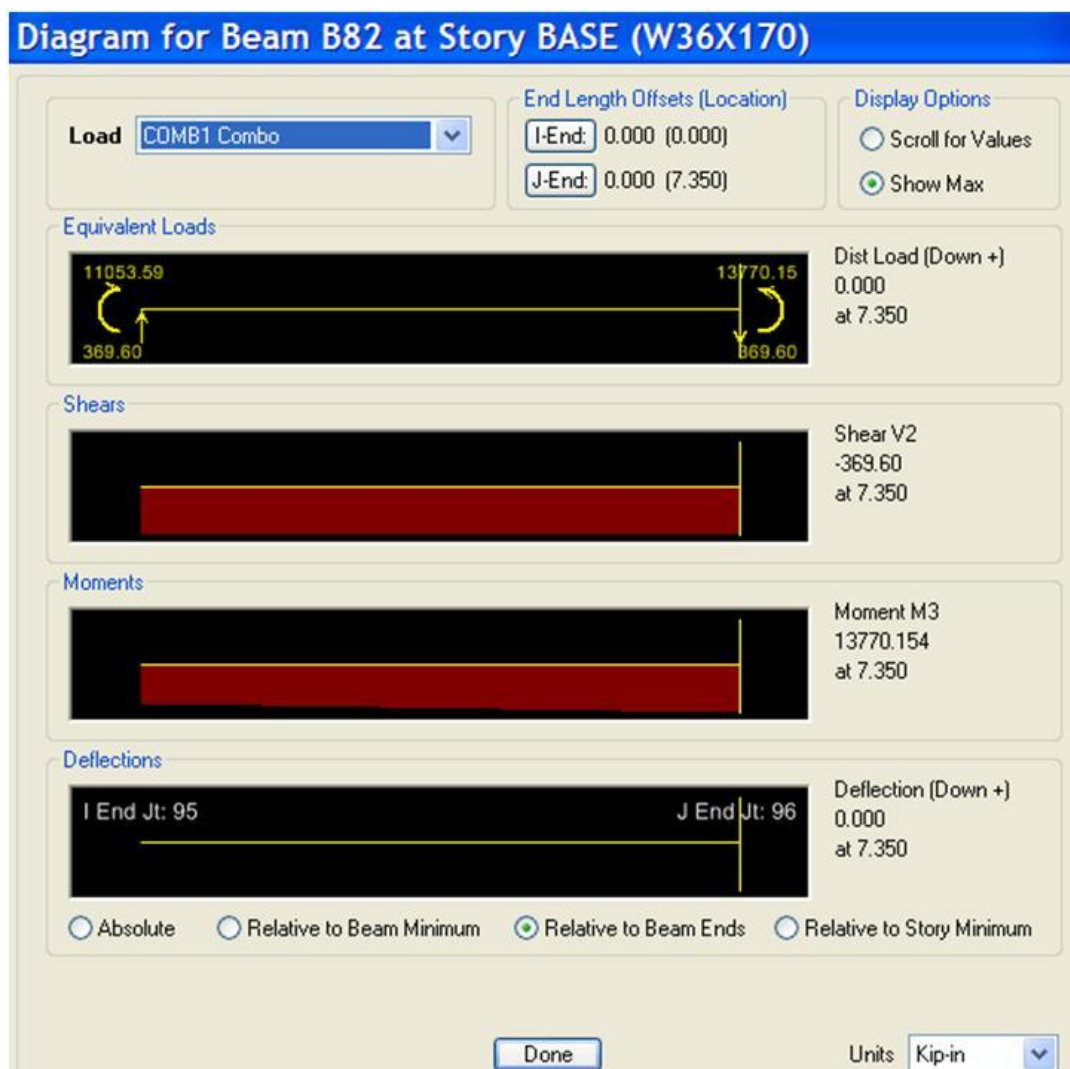


Figure 19: Maximum shear located at the support of the girder.

2.2.2 Bottom Strut arm Evaluation

The second member evaluated was the bottom strut arm. This structural member is considered to act like a column subjected to axial compressive loads. However the strut arm section is also subjected to moments caused by the eccentricity of the resultant forces from the ribs and the lateral support from the gusset plates that are welded in the connection between the girder and the strut, therefore the member is considered as a beam-column element.

The bottom and middle struts of the Carlyle tainter gate are W14x127 sections. Given that that section is not currently available the W14x132 section was chosen to perform the analysis because it has similar properties. Table 4 illustrates the properties of the strut arm section to be evaluated.

Table 4: Section and material properties for W14x132

W14x132 Section Properties			Material Properties		
$d =$	14.7	in	$F_y =$	50	ksi
$t_w =$	0.645	in	$E =$	29000	ksi
$r_y =$	3.76	in			
$I_y =$	548	in ⁴			
$C_w =$	25500	in ⁶			
$S_x =$	209	in ³			
$S_y =$	74.5	in ³			
$J =$	12.3	in ⁴			
$h_0 =$	13.6	in			
$Z_x =$	234	in ³			
$Z_y =$	113	in ³			

Following the specifications of the AISC Manual 13 edition, chapter H of the specifications, a doubly symmetric member subjected to flexure and axial force has to meet this following requirement:

$$\frac{P_r}{P_c} + \frac{8}{9} \left(\frac{M_{rx}}{M_{cx}} + \frac{M_{ry}}{M_{cy}} \right) \leq 1.0 \text{ for } \frac{P_r}{P_c} \geq 0.2 \quad 2.14$$

Where

P_r = required axial compressive strength, kips

$P_c = \phi_c P_n$ = design axial compressive strength, kips

M_r = required flexure strength, kips-in

$M_c = \phi_b M_n$ = design flexural strength, kips-in

x = subscript relating symbol to strong axis bending

y = subscript relating symbol to strong axis bending

The required axial and flexural strengths were taken from the numerical model created using ETABS. For the design axial compressive load

$$\phi P_n = \phi F_{cr} A_g \quad 2.15$$

$$\text{Where } F_{cr} = \left[0.658^{\frac{F_y}{F_e}} \right] F_y \text{ for } F_e \geq 0.44 F_y$$

$$F_e = \frac{\pi^2 E}{\left(\frac{KL}{r} \right)^2}$$

Since the strut arm is brace in various locations all the respective KL/r ratios were calculated and the controlling one was used to calculate the design load. The resulting design

compressive load $\phi_c P_n = 1,572$ kip which is higher than the required axial compressive strength, $P_r = 671$ kip as shown in Figure 20.

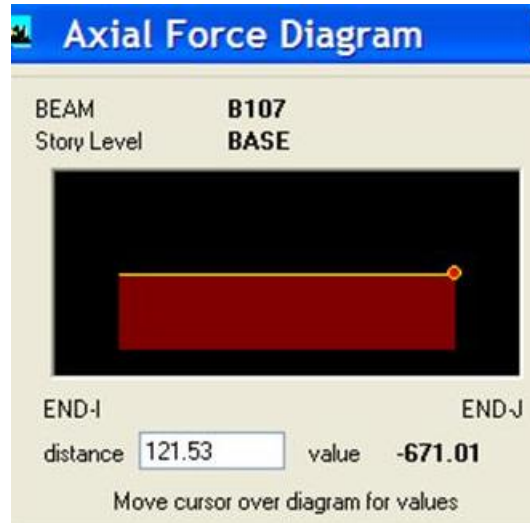


Figure 20: Required axial force for the bottom strut W14x132

The design flexural strength for the strong axis was calculated using the same procedure of the horizontal girder. Both the flange and the web are compact in the W14x132 section, therefore the same equations applied for this calculation (see Appendix C). The resulting $\phi_b M_{nx} = 6,286$ k-in which is higher than $M_{rx} = 2,130$ k-in (Figure 21).

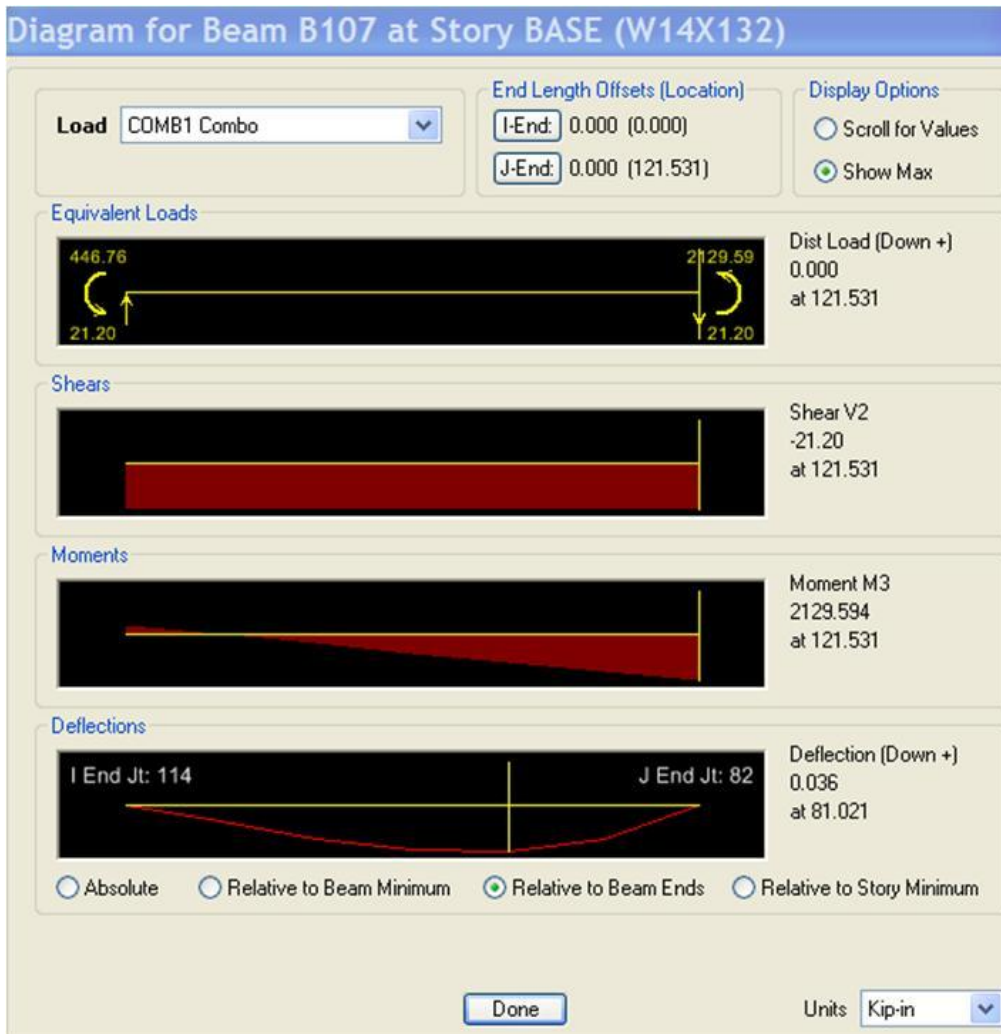


Figure 21: Maximum moment about the major axis for the section W14x132.

The design flexural strength for the weak axis moment was determined according to the section F6 from the AISC Manual 13 edition (Appendix C). The nominal flexural strength will be the lower value of the yielding and flange local buckling limit states. For the section W14x132 the plastic moment from yielding was the controlling limit with a value of $\phi_b M_{ny} = 5,085$ k-in. To calculate M_{ry} the sum of the moment about the weak axis induced by the loads is added to the moment induced by the friction in the trunnion. From the numerical calculation M_{ry} due to DL, HL and CP loads = 26 k-in as shown in Figure 22.

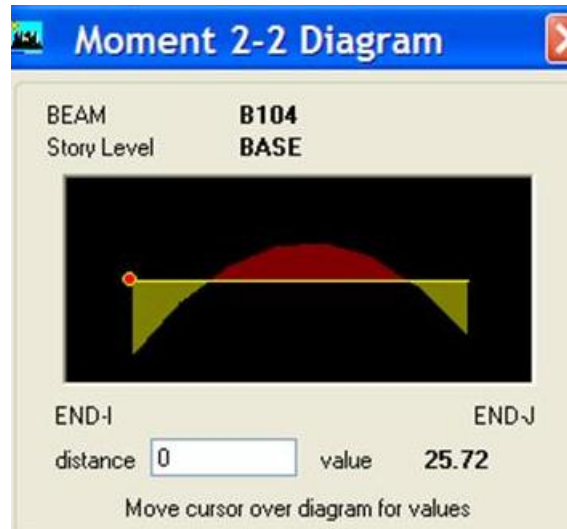


Figure 22: Maximum moment about the minor axis for the W14x132

The moment due to the friction coefficient is calculated with the reactions obtained from the model in ETABS. The reactions in the trunnion vary with respect to the position of the gate. For example when the gate is closed all the weight of the gate and the pressure from the hydrostatic load are distributed along the sill and the trunnion anchorages. As the gate opens the lifting cables start to carry the weight of the gate and the hydrostatic load decreases reducing the reactions in the trunnion. Considering the most critical case, the gate close, the resulting moment in the trunnion will be the tangential force multiplied by the distance between the surface and the center of the pin. Figure 23 illustrates the resulting reaction, R_R , caused by the vertical and horizontal reactions in the pin. The friction force, F_f , will be the product of the resulting reaction, R_R , by the coefficient of friction of the surface.

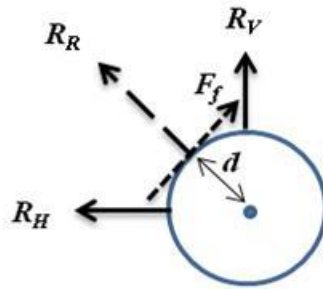


Figure 23: Reactions generated in the pin

The reaction values of the frame are shown in Figure 24. These values were taken from the model created in the engineering software ETABS.



Figure 24: Reaction in the pin due to dead and hydrostatic load, and cable pressure.

To calculate the friction force in the pin, F_f , the resultant force was multiplied by a friction coefficient assumed to be 0.3 (this is a typical value for these structures). This force was then multiplied by the radius of the pin giving a value of M_{ry} due to FC = 1200 k-in (see Appendix C). Therefore $M_{ry} = 1,226$ k-in.

Taking into account that by the time this structure was designed the weak axis moment was not taken into consideration a verification of the equation 2.14 was performed. The values of

M_{ry} and M_{cy} were taken to be zero. Substituting the values for the required and design axial and flexural strength the expression was $0.73 \leq 1$ which complies with the expression below.

$$\frac{P_r}{P_c} + \frac{8}{9} \left(\frac{M_{rx}}{M_{cx}} + \frac{M_{ry}}{M_{cy}} \right) = 0.73 \leq 1$$

Recalculating the expression with the values of the moment in the weak direction it gives

$$\frac{P_r}{P_c} + \frac{8}{9} \left(\frac{M_{rx}}{M_{cx}} + \frac{M_{ry}}{M_{cy}} \right) = 0.94 \leq 1$$

The computations demonstrate the importance of the consideration of the weak axis moment. Assuming a value of 0.3 for the coefficient of friction the expression increased from a value of 0.73 to 0.94. If the coefficient of friction was higher it could jeopardize the stability of the structural system.

3 TAITNER GATES EXPERIMENTAL STUDIES AT CARLYLE DAM

3.1 Experimental procedure

In 2008 a professor from the University of Missouri-Columbia, Dr. Gopalaratnam in association with Dr. Riveros from the U.S. Army Engineering Research and Development Center performed a series of experiments on a tainter gate with similar geometrical and material characteristics to the gate that failed in Folsom Dam. The purpose of this experiment was to obtain stresses and strains from specific locations in the structure to evaluate the friction coefficient in the trunnion, study its effects in the elements of the gate and determine its vulnerability to trunnion friction induced failure. The experiment was performed in the Carlyle Lake Dam, Illinois (Figure 25), located fifty miles east from St. Louis.



Figure 25: Carlyle Lake Dam. Picture from Dr. Gopalaratnam and Dr. Riveros experimental procedure.

The tainter gate in which the experiments were performed has a skin-plate height of 43 ft and a width of 38 ft. The whole gate's mass is 119,450 lb. The skin-plate is supported by 21 vertical T-beams and 3 horizontal girders. The strut arms are strengthened by a series of diagonal bracings to reduce the un-brace length of the arms (Figure 26). The gate is raised by two flat wire ropes 10-in. width that are attached to a lifting mechanism located at each lower end of the skin-plate (Figure 1). The lifting mechanism consists of two steel plates connected with a beam with a circular cross-section.

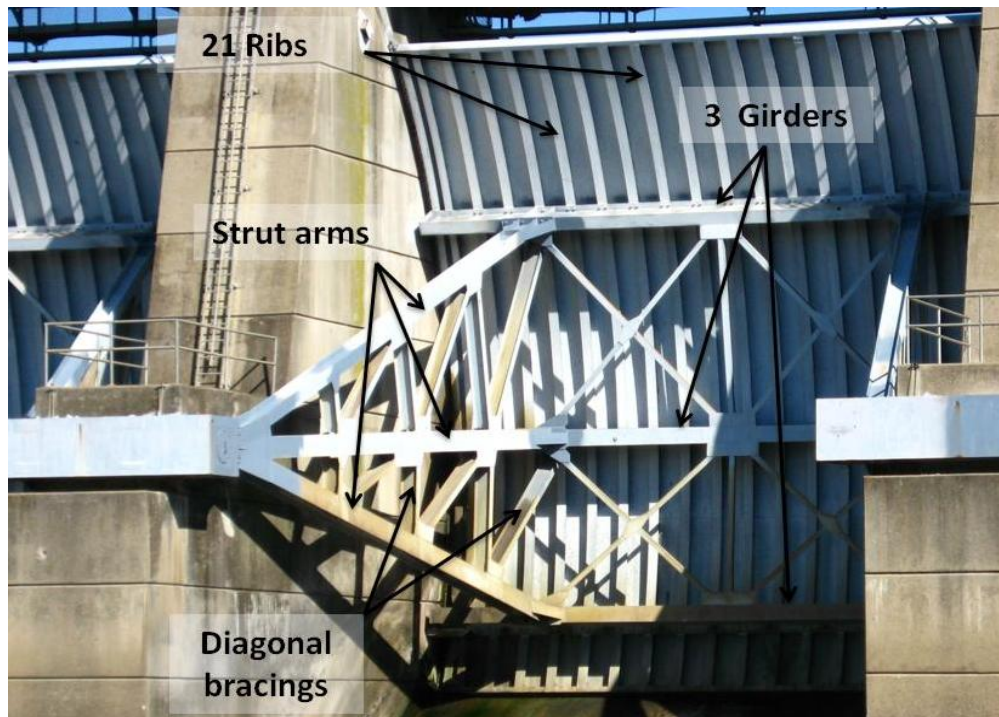


Figure 26: Carlyle tainter gate components. Picture from Dr. Gopalaratnam and Dr. Riveros' experimental procedure in Carlyle Lake Dam.

Sixteen clamp-on transducers were placed at the flange edges of the struts and strut diagonal bracings, eight on each side to measure the state of strains at those locations. The transducers consisted of an aluminum plate with the measuring gages attached to the surface

(Figure 27). The purpose of the aluminum plate was to increase strain output, minimize the potential for corrosion caused by long-term exposure to moisture and to reduce temperature drift between the steel and the aluminum. The gages were individually calibrated using a 3-point bending test configuration in a closed-loop MTS testing machine (Figure 28). For the calibration the transducers were placed in a rigid beam in the same position as in the experiments. A 3-point bending test consists of a beam simply supported at each end and a load is applied in the middle. Figure 29 illustrates the location of the transducers in one side of the arms. The figure shows eight gages, four at the struts (two in the top strut arm and two in the bottom strut arm) and four at the strut bracings (two in the bracing closer to the skin-plate and two in the second diagonal bracing). These locations are the same for the other eight gages in the other side of the gate.



Figure 27: Clamp-on transducers placed in the gate for strain measurements. Picture from Dr. Gopalaratnam's presentation "Strain Measurements and Numerical Investigation of Tainter Gate Operations".



Figure 28: MTS testing Machine. Picture from Dr. Gopalaratnam's presentation "Strain Measurements and Numerical Investigation of Tainter Gate Operations".



Figure 29: Location of the transducers in the Carlyle Tainter Gate. Picture from the experimental procedure performed in Carlyle Lake Dam by Dr. Gopalaratnam and Dr. Riveros.

The process of instrumentation and installing the transducers in the gate is complicated and physical. Given that these structures are big and the struts are located in the downstream side, it requires rappelling to place the transducers in their designated location. Figure 30 shows the installation of the instruments at the Carlyle Dam in 2008, which shows the physical and difficult processes to install the transducers.



Figure 30: Installation challenges. Picture from experimental procedures performed by Dr. Gopalaratnam and Dr. Riveros in Carlyle Lake Dam.

The experimental procedure performed in the Carlyle tainter gate consisted in applying a small displacement to the gate lifting and lowering it to measure the variation of strains throughout the experiment. Figure 31 shows the time vs. elevation curve which illustrates that the gate was lifted 9.6 inches from the sill, and then stopped for a small amount of time. It was lifted again 7.2 inches (to an elevation of 16.8 inches) and stopped. Then the gate was lowered to an elevation of 9.6 inches, stopped and finally lowered to the sill.

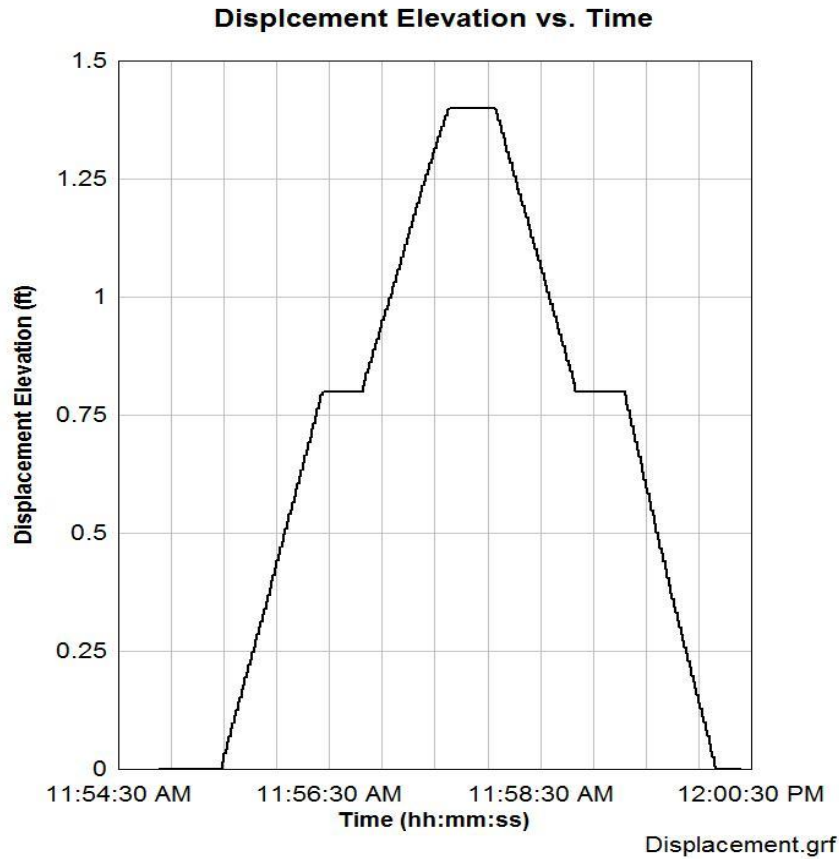


Figure 31: Displacement Elevation vs. Time plot

3.2 Experimental results

From the experimental procedures a series of strain plots versus time were obtained. Depending on the location of the gages, different behavior throughout the experiments were observed. Figure 32 illustrates the location and nomenclature of each gage. The discussion of the results is divided by the location of the gages, top strut arms, bottom strut arms, diagonal bracings and diagonal bracings closer to the skin-plate.

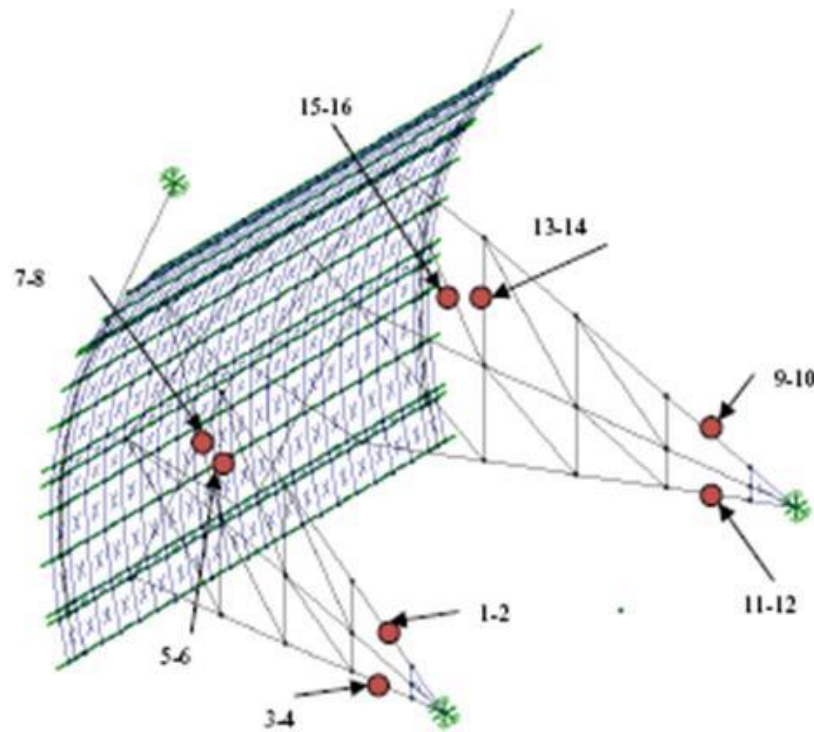


Figure 32: Gage location and nomenclature. Picture from Gopalaratnam’s presentation “Strain Measurements and Numerical Investigation of Tainter Gates Operations”.

Figure 33 presents the plots of the two top strut arms of the gate, gages 1, 2, 9 and 10. In the plots the gages are labeled as series. Also the displacement vs. time curve is shown, such that the strain behavior with respect to the elevation of the gate can be compared. Even though these gages are located in the same position they do not show the same behavior. The gages were calibrated to start at zero at the beginning of the experiments, therefore the initial step does not consider the self weight and the hydrostatic pressure loads. From the plots it can be seen a noticeable jump right when the gate starts to open. This jump can be attributed to the combination of the drastic pull the cable exerts in the bottom of the skin-plate and the initial static friction force the hub needs to break to start the rotation of the gate. This pull causes an

abrupt instant tension in the top strut arm members. As the gate keeps opening the tensile strains start decreasing because the self weight and cable pressure loads are compressing these members. In gage 1, the initial jump caused compression and as the gate starts going up the member decompresses until the gate starts to go down. Only gage 1 illustrates a different behavior when the gate starts to open, which indicates that the outer side of the left top strut is compressing while the inner side of the strut is in tension. During the stops there is no significant change in strains. There is also a significant jump in strains when the gate starts going down. The self weight of the gate pushes down and the top strut arms have an abrupt increase in tension. At this point gage 9 illustrates a different behavior with an instant increase in compression. In this case the outer side of the right top strut arm is in tension while the inner side of the strut is in compression as well as the left top strut. This behavior can be attributed to unsymmetrical loading in the lifting cables.

Figure 34 illustrates the cross section diagrams for the top strut gages throughout the experimental procedure. The left top strut arm, with gages 1 and 2, starts almost in pure bending as oppose to the right top strut arm (gages 9 and 10) that is carrying only axial load. As the gate is moving up both strut are mostly in flexure but when the gate is moving down, the members experience more tension in the inner side of the element.

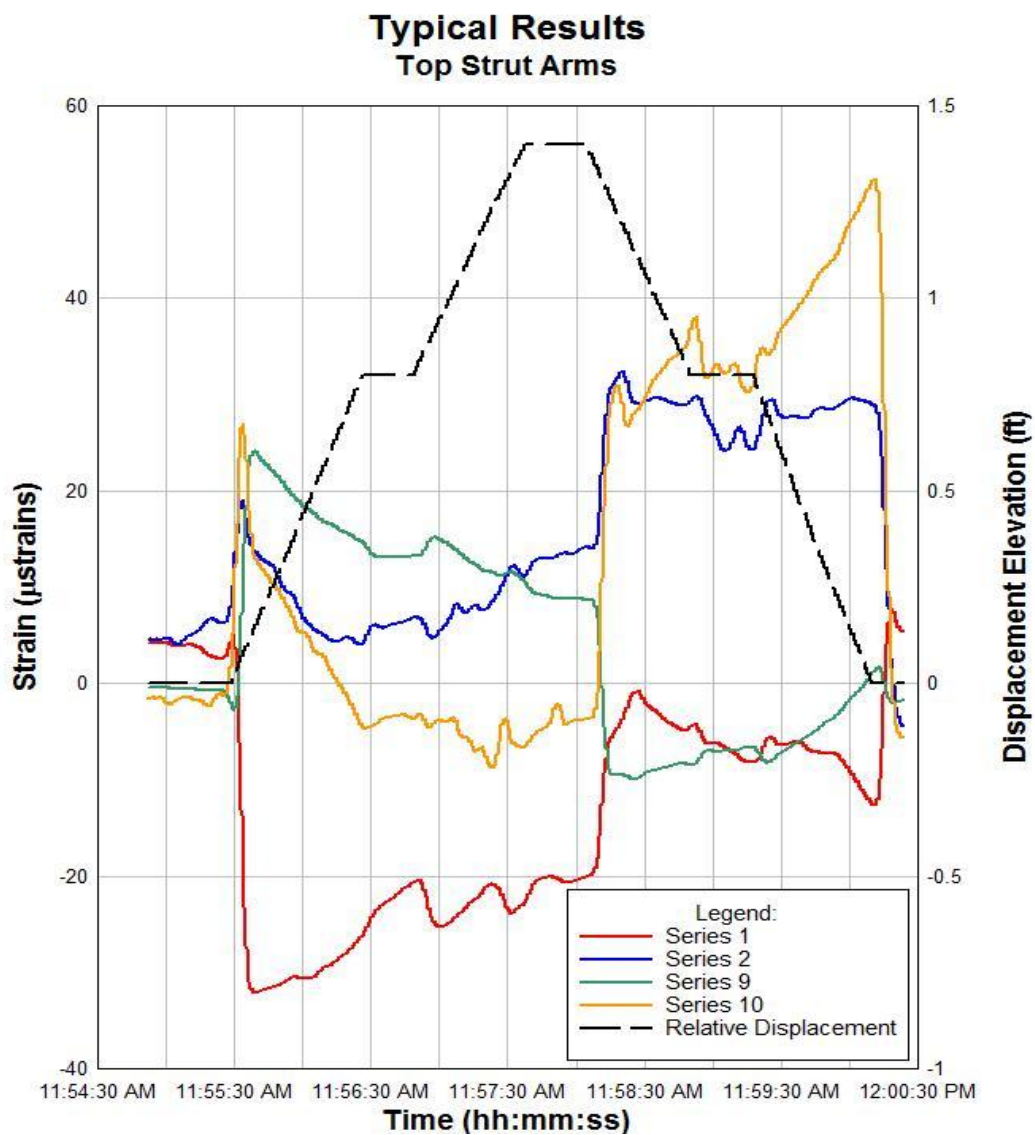


Figure 33: Typical Results, Top Struts Gages

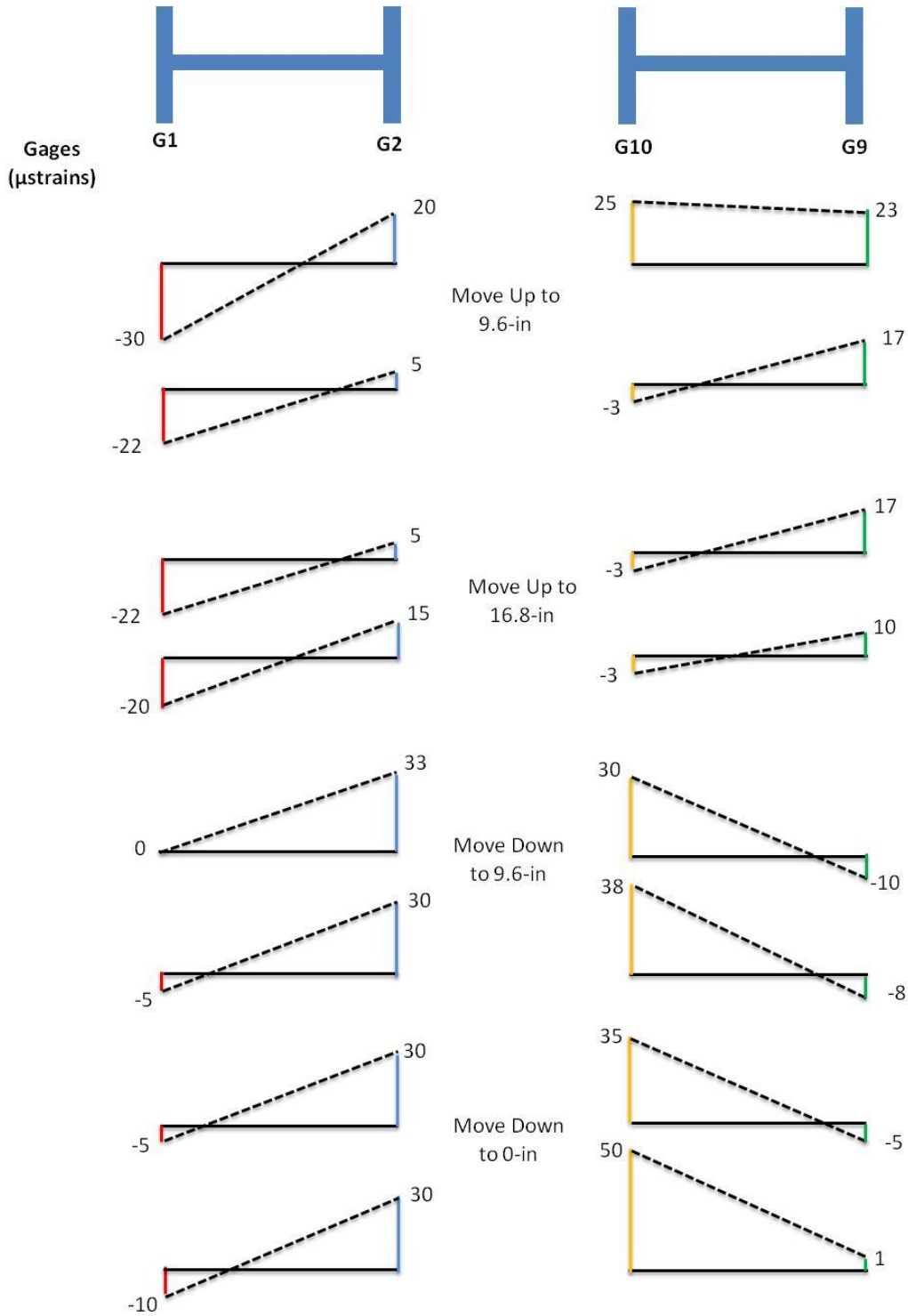


Figure 34: Cross section strain diagram for top strut arms

The bottom strut arm gages have a different behavior than the ones in the top strut arm but similar between each other. These gages are labeled 3, 4, 11 and 12. The initial jump due to the cable tension has a bigger impact on the bottom struts because the lifting mechanism is near that area causing the bottom strut arms to have higher tensile strain magnitudes. Also, the breaching of the static friction contributes to the magnitudes of these strains. When the gate starts to open, the forces from the self weight and the hydrostatic pressure are transmitted from the sill to the bottom strut arms in the gate, thus compressing the members reducing the tensile strain magnitudes. As the gate moves up, the tensile strains decrease at a faster rate compared to the top strut gages because the effect of the hydrostatic load is higher. Contrary to the top strut arms, when the gate is raised for the second time, there is a significant change in strains in all of the gages because they are transferring a higher amount of loads to the trunnion. The members continue compressing until the gate is stopped and starts to go down. When the gate starts to move down there is an instant compression in the member due to the self weight and the hydrostatic pressure. As the gate goes down the strains release their compression until they return to their initial state. In the bottom strut arms strain magnitudes remain constant during the stops.

The cross section strain diagrams from the bottom strut gages (Figure 37) illustrate how these elements are subjected to both axial and flexural forces. It is also noticeable that when the gate is lifted the bottom strut arms are in pure tension and when the gate is moving down they are subjected to pure compression. From the strain diagrams the axial force and moment from the section can be calculated. For example, taking the left side top strut with gages 1 and 2 it is shown that the first registered strains are 30- μ strains in compression and 20- μ strains in tension.

From Figure 35 it can be seen that 25-μstrains are in bending and 5-μstrains in pure compression.

$$P = AE\epsilon \tag{3.1}$$

$$M = SE\epsilon \tag{3.2}$$

Where,

P = axial force, kip

M = bending moment, ksi

ε = axial strains, μstrains

A = section area, in²

S = elastic section modulus, in³

E = modulus of elasticity, ksi

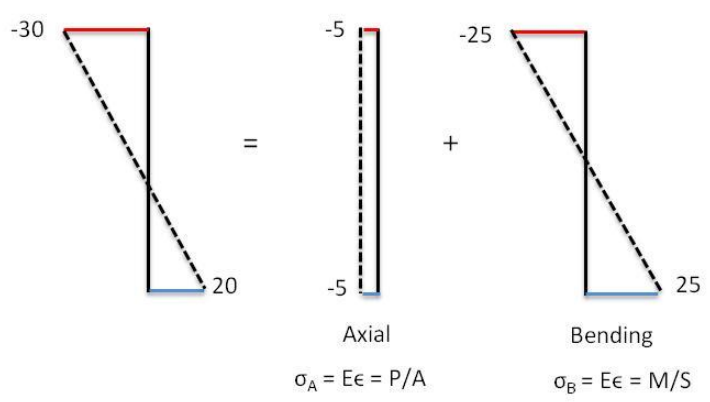


Figure 35: Strain diagram for left top strut when the gate starts to open

For the section W14x61 (top strut) the resulting initial axial force and bending moment when the gate is starting to move up are 3.6 kip and 67 k-in. respectively.

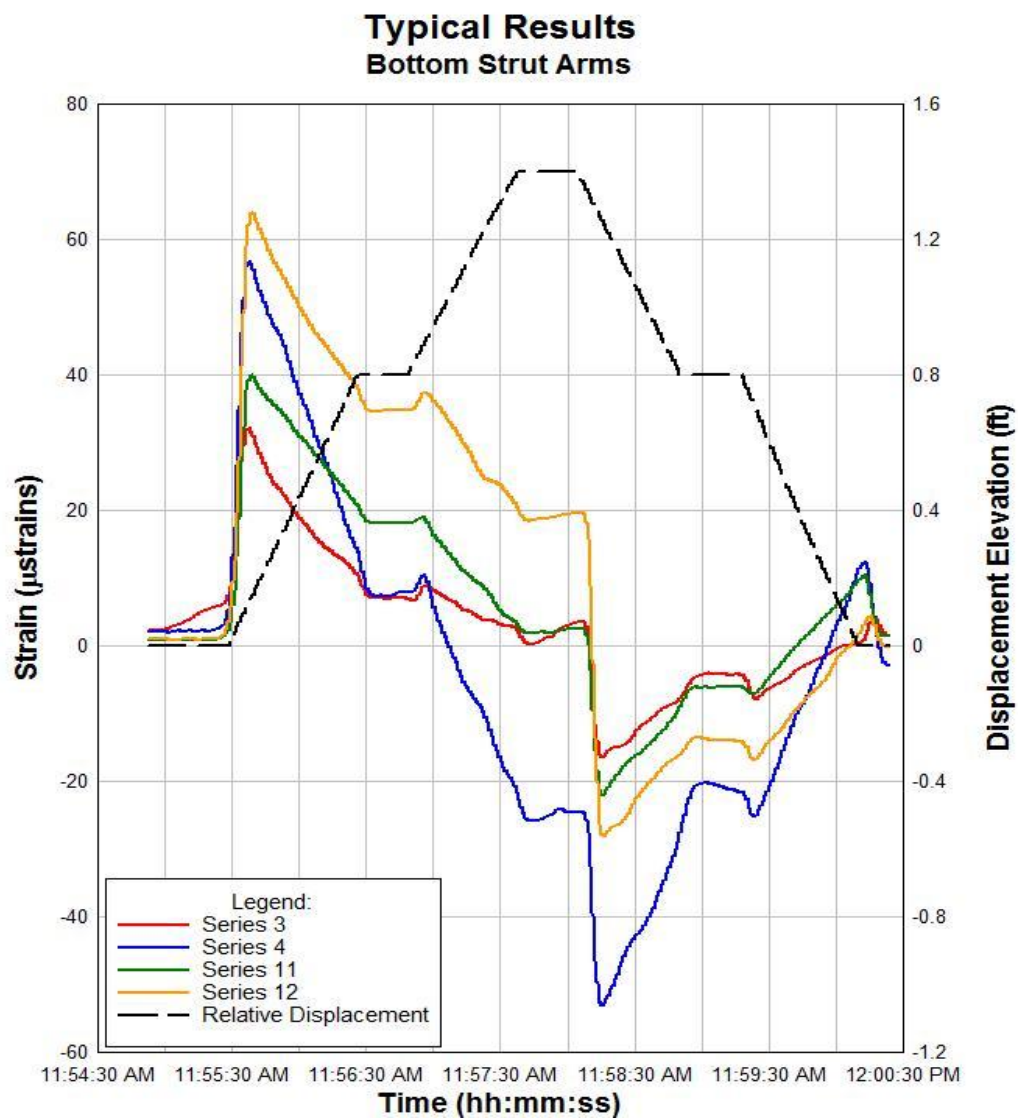


Figure 36: Typical Results, Bottom Strut Gages

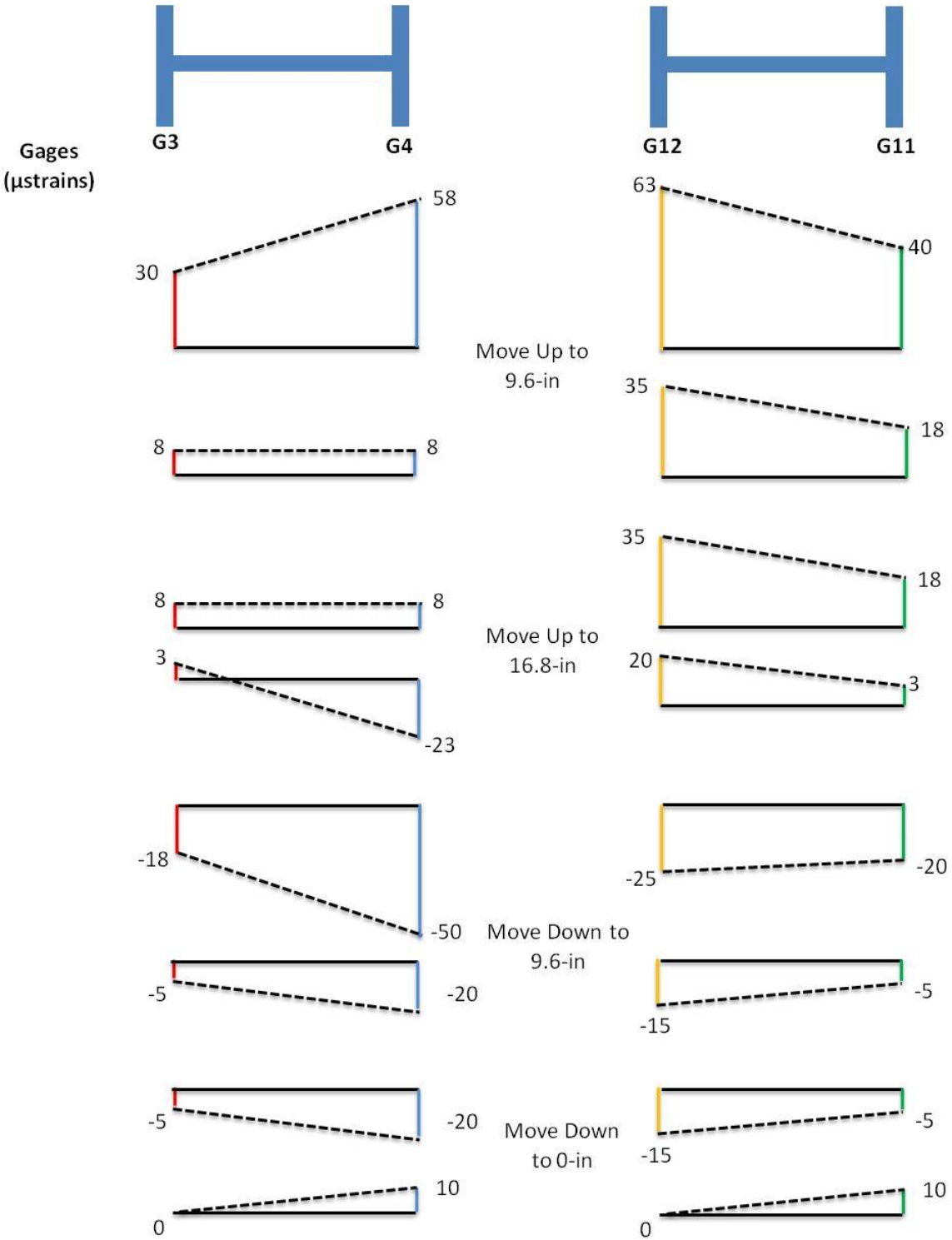


Figure 37: Cross section strain diagram for top strut arms

The diagonal bracing gages have a less structured behavior throughout the test compared to the strut arms. Figure 38 shows the plots for the gages 5, 6, 13 and 14. These members also experienced the initial tension caused by the initial pull of the lifting cable, but as the gate goes up for the first time, the diagonal bracing from the right side (gages 13 and 14) increases in tension as the diagonal bracing from the left decreases in tension. This behavior can be attributed to unsymmetrical loading in the cable pressure. As well as the bottom strut gages, the diagonal bracing experience the same instant compression when the gate starts to move down, which could be attributed to the self weight load when the gate changes in direction.

Figure 39 illustrates how contrary to the strut arms the diagonal bracings are subjected to almost pure axial loads. This behavior demonstrate that the bracings act like truss members in the gate. It is also noticeable the considerably smaller strain deformations at which both diagonal bracings are subjected compared to the ones from the strut arms.

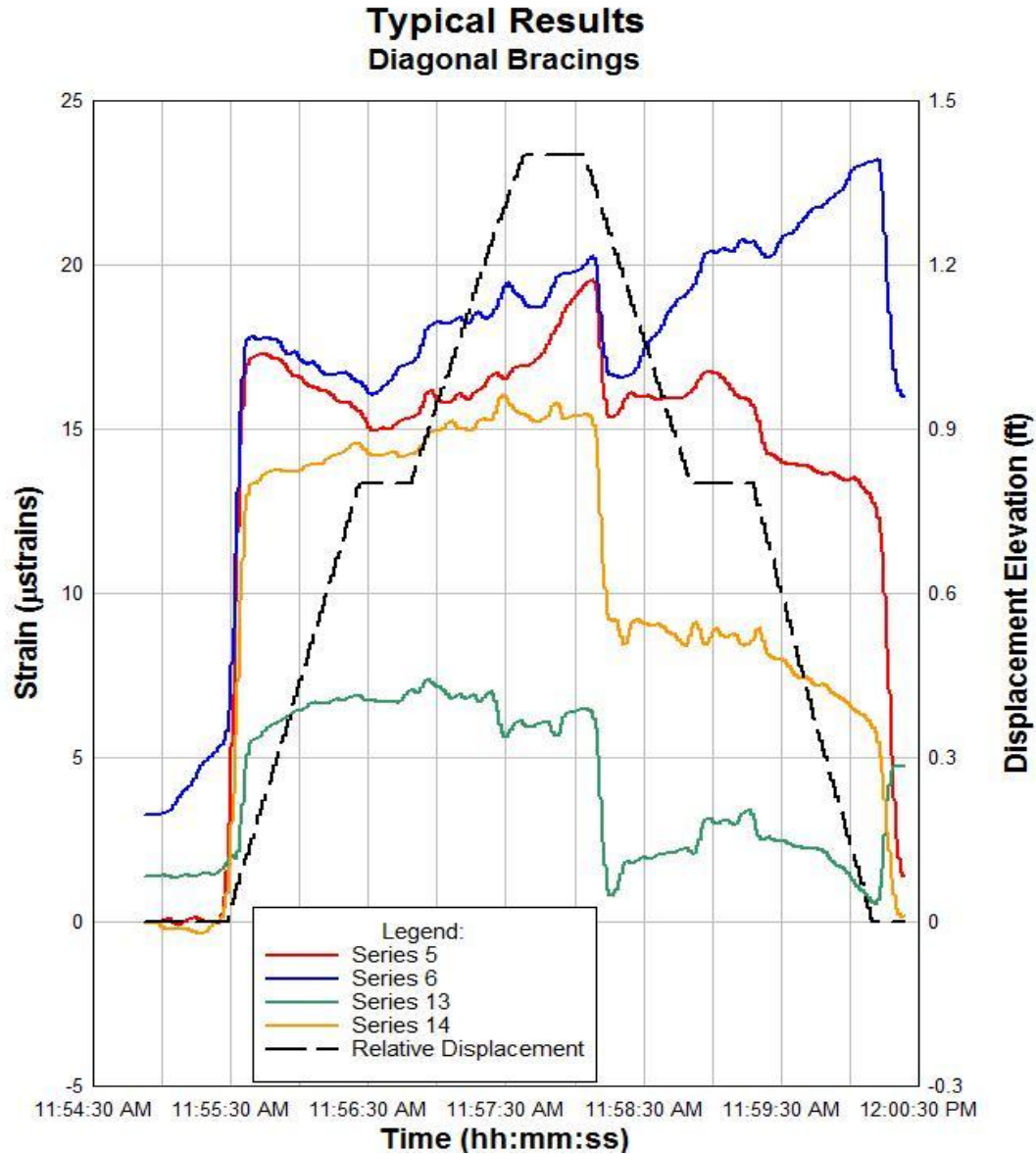


Figure 38: Typical Results, Diagonal Bracings

The diagonal bracings close to the skin-plate have almost a linear behavior throughout the whole experiment. Figure 40 show the typical results for the gages 7, 8, 15 and 16. Different to the other strut arms and diagonal bracings, the initial lifting of the gate caused compression in the members instead of tension. As the gate opens, the members start to release the compression. The diagonal bracing closer to the skin-plate from the right stays in compression during the test

as the other one starts to act in tension when the gate goes down. The gages from Figure 38 illustrate this same behavior which means that in overall the right side of the structure is perhaps receiving more compressive loads that the left side.

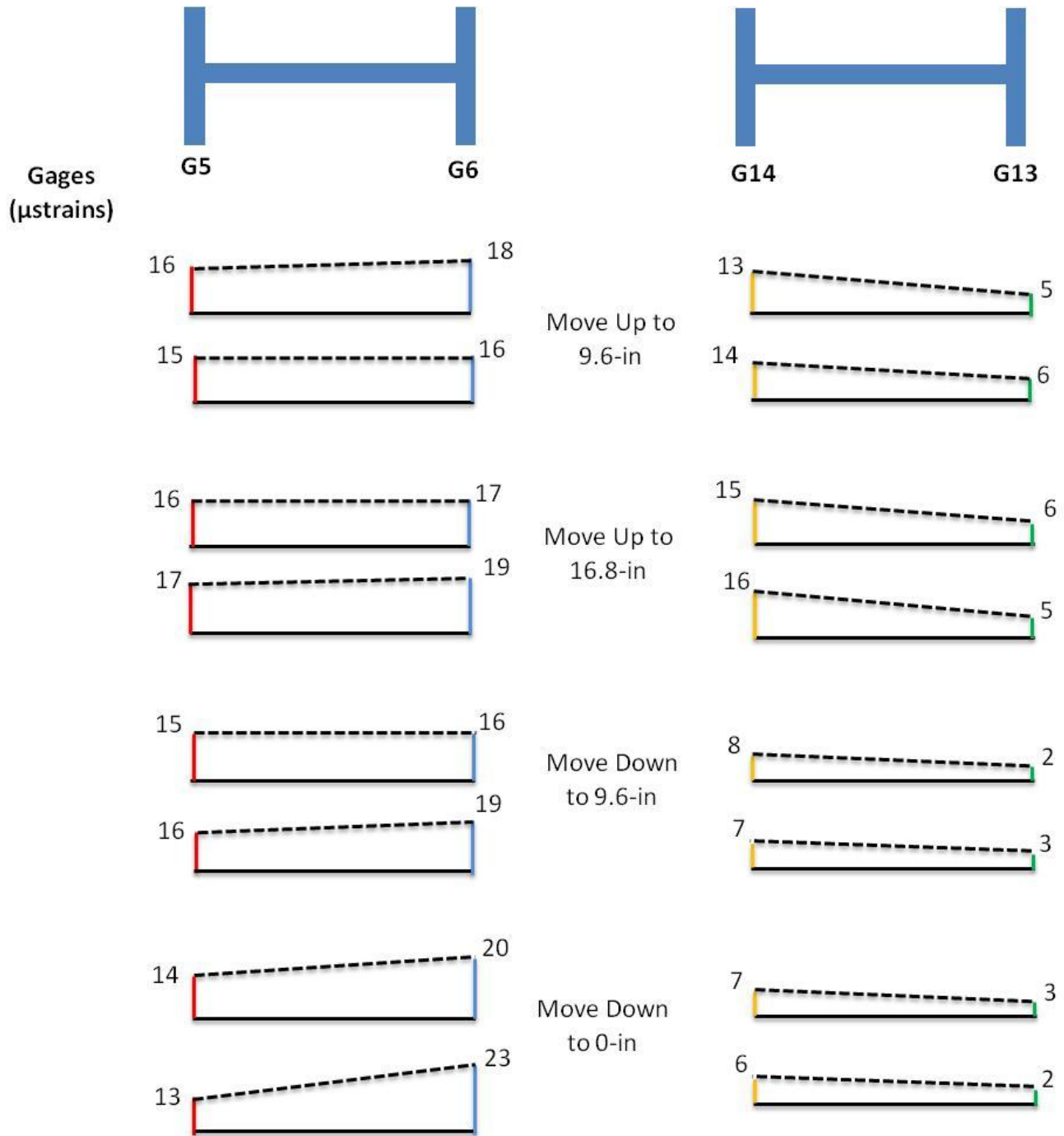


Figure 39: Cross section strain diagram for diagonal bracings

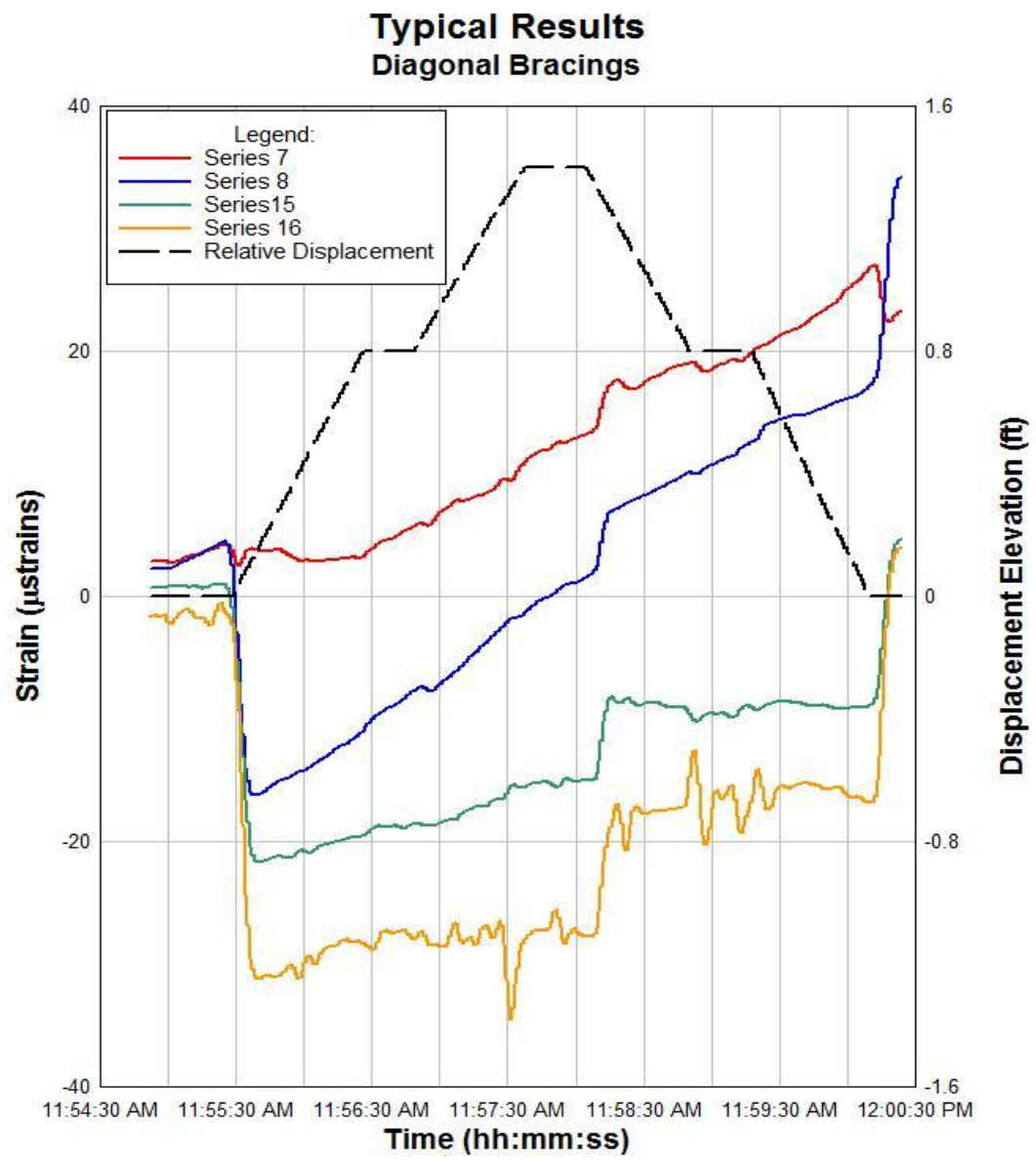


Figure 40: Typical Results, Diagonal Bracings close to Skin-Plate

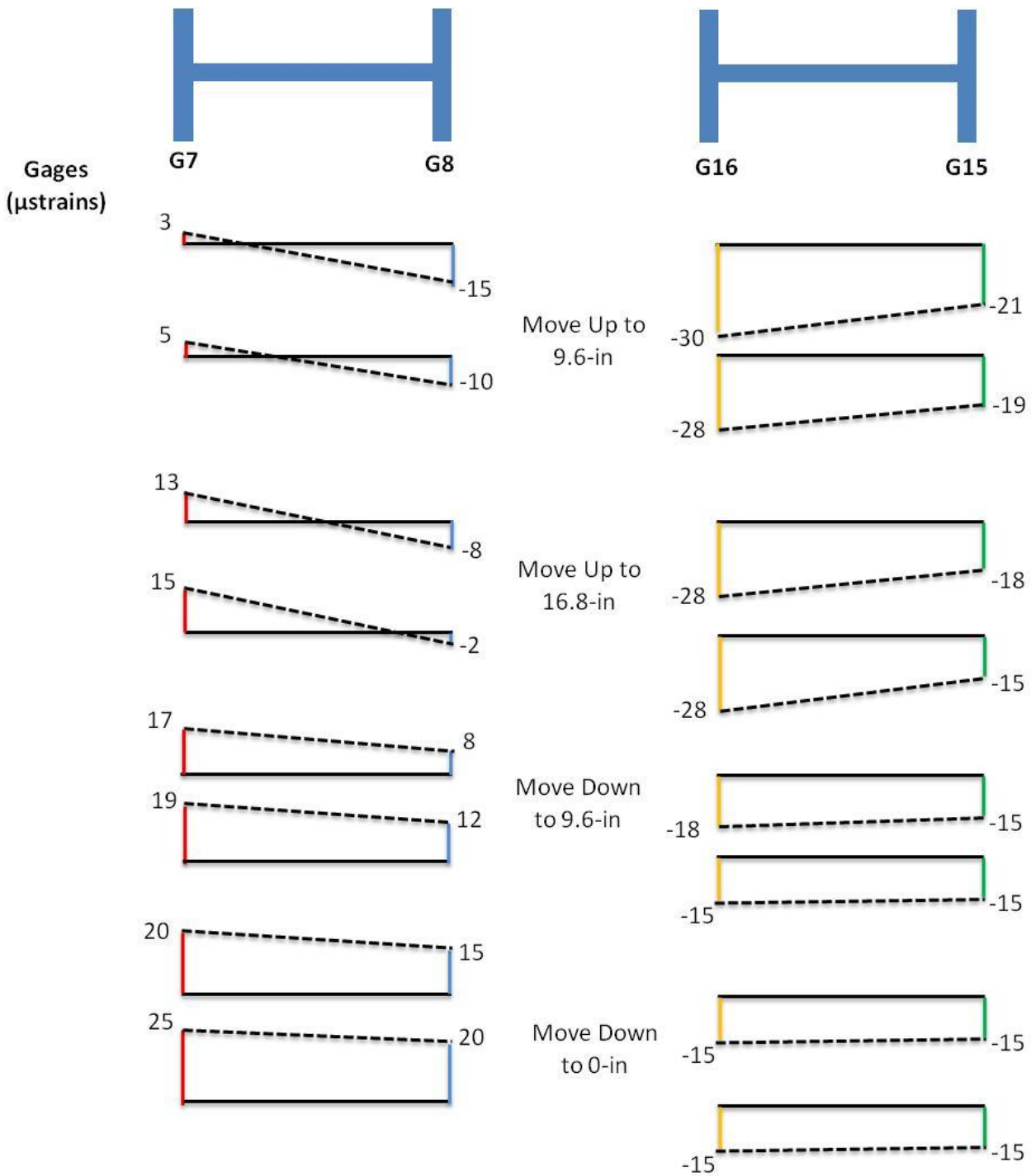


Figure 41: Cross section strain diagram for diagonal bracings closer to the skin-plate

Figure 41 show the cross section strain diagrams for the diagonal bracings closer to the skin-plate. Even though these diagrams show a similar behavior to the diagrams from gages 5, 6, 13 and 14, they show slightly more bending than the other diagonal bracings. This is because the diagonal bracings with gages 7, 8, 15 and 16 are closer to the skin-plate thus receiving more flexural loads from the girders.

The overall behavior of the members of the gate fulfilled its expectation. The struts arm components had higher strain magnitudes, which means that they are the principal elements transferring the loads from the skin-plate to the trunnion. Several differences between the outputs from each gage can be attributed to unsymmetrical loading, different friction coefficient in each pin and dynamic load effects, like vibrations due to the flow of water.

3.3 Experimental procedure achievements

The ultimate goal of the experimental procedure was to obtain the strain behavior with respect to time of the structural members while lifting and lowering the gate. It was found that the most critical phases, when the stresses acquire the biggest increments, were the initial lifting of the gate from the sill and initial lowering of the gate towards the sill. This phenomenon is attributed to the pull generated by the lifting cable at the beginning of the procedure and when the gate starts to go down. When the gate is resting on the sill the cables are not completely tight therefore when the gate opens the cables generate an instant pressure that causes a rapid increase of stresses in the components of the gate. The same principle occurs when the gate starts to move down because as the cable releases the weight of the gate instantly pulls down generating higher strains.

4 COMPUTATIONAL STUDY OF TAINTER GATES

The finite element analysis software Abaqus CAE v6.10 was used for the computational modeling and simulation of the tainter gate. Figure 42 illustrates a flowchart describing the computational modeling and simulation procedure used to create the tainter gate structure. The computational model describes the approach of the problem, the definition of the geometry, materials and the mesh. The computational simulation is the execution of the problem, in this case the recreation of the experimental procedure in the 3-D numerical model.

The gate used for this study was the tainter gate from the Carlyle Dam, which was previously subjected to experimental evaluations. The numerical model was developed based on the geometry from the original 1961 As-Built drawings. These As-Built drawings were obtained from the U.S. Army Engineer District St. Louis, MO and U.S. Army Engineer District Mobile, AL. The finite element model was created using isotropic and elastic shell elements because

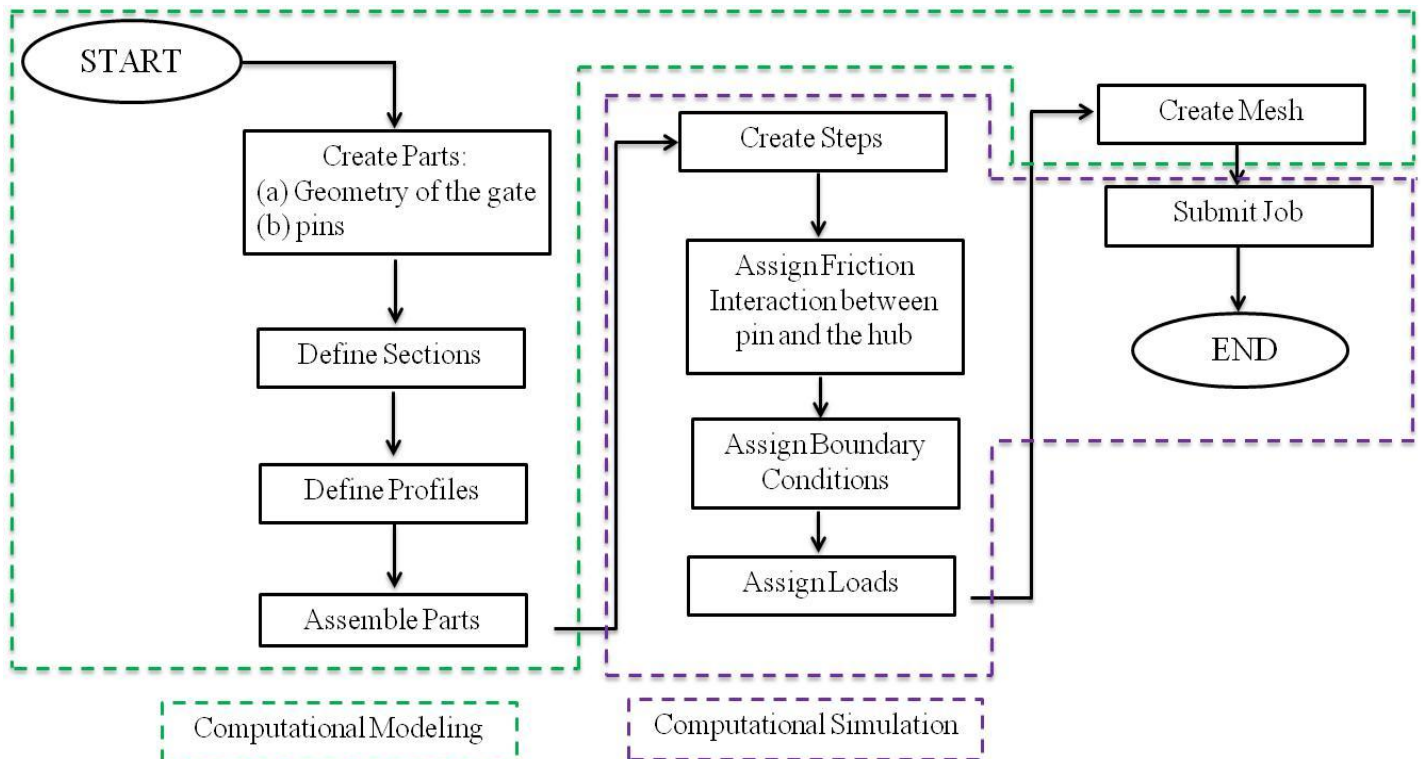


Figure 42: Computational modeling and simulation flowchart.

contrary to plates they can be curved and they support both membrane and bending forces. The loads and displacement boundary conditions applied to the tridimensional model resembled the experimental procedure previously described in chapter 3. For the numerical model analysis the static implicit method was used because the application of the loads and the displacement of the gate in the experimental procedure were relatively slow. The implicit method uses a static stress analysis in which the inertia effects are neglected, the model can be either linear or non linear, and ignores time-dependent material effects like creep or swelling (Abaqus 2010).

4.1 Computational Modeling

The 3-D model was created in two different parts. First, the whole geometry of the gate including the skin-plate, ribs, horizontal girders, strut arms, strut bracings, the gussets plates and the hub. These parts were created as 3-D deformable shells, the lifting beams, which were also included in this part, were created as beam elements with a profile section defined as a circle with a radius of 3-in. The second part of the model was the pins located inside the hubs (Figure 43). The pins were created as 3-D deformable solids.

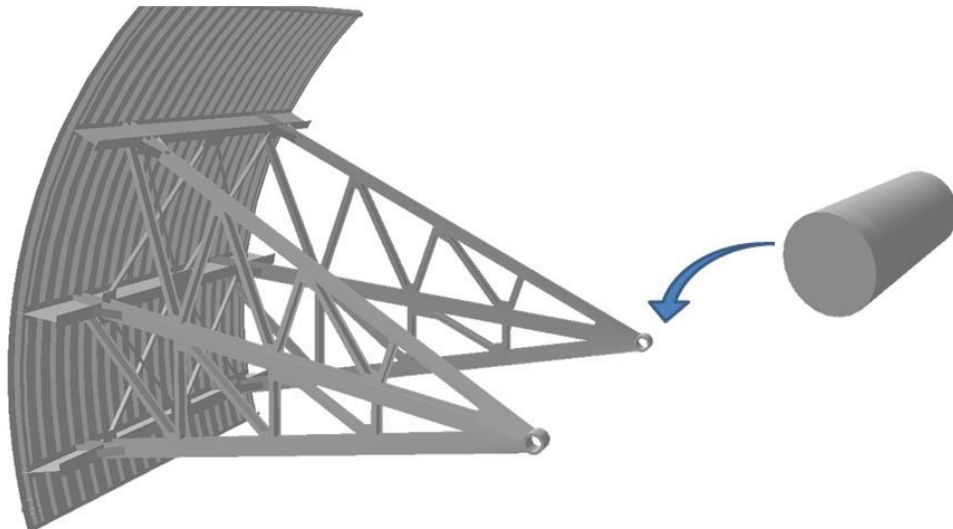


Figure 43: Deformable solid pin inside tainter gate's hub.

To assign the properties of each element a set of sections were created. For the shell sections the thickness and the material of the element was included. For the solid section, only the material of the element was defined. The beam section included the material and the definition of the profile. The material used for the elements of the gate was structural steel with a modulus of elasticity of 29,000 ksi.

Abaqus CAE v6.-10 performs an analysis of the instances that are in the assembly module. This module ensemble the independent parts and unifies all the components of the structure. In this case the whole gate part was ensemble with the pins, which are located at the end of the strut arms inside the hubs. Once the entire model is assembled, the interaction between the pin and the hub was created. This interaction describes the frictional behavior between the pin and the hub. The following section explains in detail the formulation used for the friction interaction.

Since the numerical model of the Carlyle tainter gate is simulating the experimental procedure for validation purposes, the steps created in the numerical analysis simulated the experimental procedure of lifting and lowering the gate. The simulation was performed using loads displacement boundary conditions to describe the procedure in each step. This process is explained in more detail in the computational simulation section.

The last step before submitting the job is to create the mesh for the assembly model. The mesh was created individually for the pins and the gate structure (Figure 44). At the locations where the gages were placed, the model has a finer mesh to obtain better results. The areas of the skin-plate, the horizontal girders, and the struts parts farther from the trunnion had a coarser refinement to reduce the model size, thus reducing the computational time. Because of the complex geometry of the gate the chosen element shape was quad-dominated. The element type used for the whole gate was a 4-node doubly curved thin shell with reduced integration of linear

geometric order. The reduced integration formulation is applied to reduce the computational time of the model because it only integrates one point inside each element instead of each of the edge points of each element. For the pins, an 8-node linear brick with reduced integration was used.

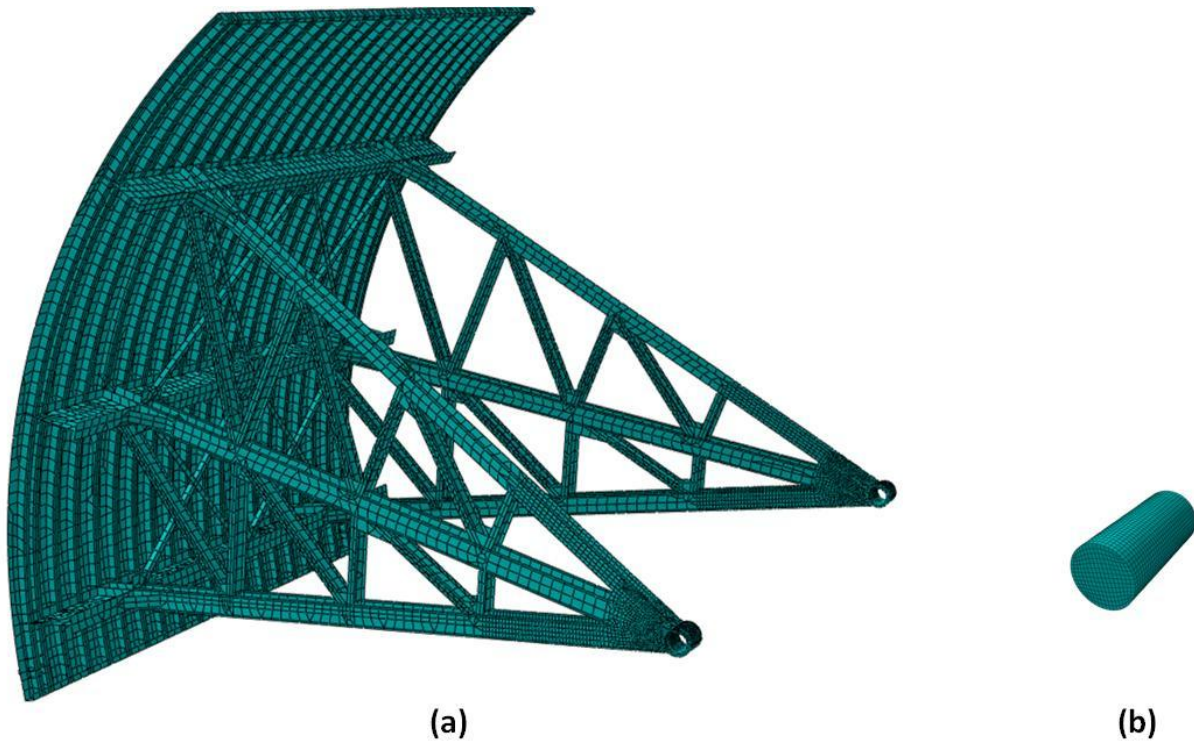


Figure 44: (a) Mesh for the shell elements of the gate. (b) Mesh for the solid elements of the pin. Picture from the 3D numerical model in Abaqus CAE v.6-10.

4.2 Computational Simulation

The computational simulation of the 3D numerical model describes the physical procedures performed in the Carlyle Dam tainter gate experiments. For this simulation the finite element method was implemented to obtain the state of strains acting in the structure due to the applied loads and operation. The following sections explain how the finite element method works, the steps implemented in the 3D numerical model, and the interaction formulation used for the analysis.

4.2.1 Finite Element Method (FEM)

The Finite Element Method consists of finding an approximate solution to complex continuous field problems. To solve these field problems certain parameters have to be known, such as geometry, material properties, loads and displacement boundary conditions. With these information multiple output parameters can be obtain, such as stresses, strains, forces and deformations. This study was conducted using a quasi-static implicit simulation with Abaqus CAE v.6-10.

In Abaqus CAE v. 6-10 the general static analysis consists of solving nonlinear problems. Is easier to identify a nonlinear problem by describing what it cannot do as oppose to what it can. A nonlinear system does not satisfy the superposition principle and its output values are not directly proportional to its input, which are conditions that can be fulfilled by a linear system. Some types of nonlinearity in structural mechanics include:

Material nonlinearity: Material properties are functions of the state of stress or strain.

Contact nonlinearity: Includes opening or closing of gaps between adjacent parts, changes in contact area between parts as the forces changes and sliding contact with frictional forces.

Geometric nonlinearity: Deformations are large enough that equilibrium equations have to be written with respect to the deformed structural geometry. (Cook R. *et al*, 2003)

For the tainter gate the contact and geometry nonlinearities applies. In this type of problem the load is function of displacement or deformation. This problem solving method involves a combination of incremental and iterative procedures that use Newton's method to solve nonlinear equations, which determines convergence by defining the loads as a function of time and choosing suitable time increments automatically (Abaqus, 2010). To define the problem in Abaqus/Standard it is required to create a series of steps that will describe a procedure, define the load and displacement boundary conditions, and request an output. Each step is broken into increments to follow the nonlinear solution path, the first increment is suggested by the user and the next is calculated by the program until it reaches an approximate equilibrium. Each increment consists of iterations, which are attempts to find an equilibrium solution in an increment. Every iteration will get the solution closer to equilibrium although sometimes it diverges. In that case the program terminates the iteration process and intends to find a solution with a smaller increment.

4.2.1.1 Newton-Raphson Method

The models generated in Abaqus can involve up to thousands variables and are usually nonlinear. The basic equilibrium equation that the finite element analysis software solves is:

$$\mathbf{F}^N(\mathbf{u}^M) = \mathbf{0} \quad \mathbf{4.1}$$

Where

F^N = Force component of the N^{th} variable.

u^M = Displacement value of the M^{th} variable.

After an initial iteration i , an approximate value u_i^M has been obtained with an increment of c_{i+1}^M , thus

$$F^N(u_i^M + c_{i+1}^M) = 0 \quad 4.2$$

Expanding the equation in a Taylor series about the approximate solution u_i^M ,

$$F^N(u_i^M) + \frac{\partial F^N}{\partial u^P}(u_i^M)c_{i+1}^P + \dots = 0$$

The magnitude of c_{i+1}^M will get smaller as the approximation of u_i^M , gets closer to the exact solution, therefore all but the first two terms of the equation can be neglected giving the following equation,

$$K_i^{NP} c_{i+1}^P = -F_i^N$$

Where

$$K_i^{NP} = \frac{\partial F^N}{\partial u^P}(u_i^M)$$

The equation above is the Jacobian matrix and

$$F_i^N = F^N(u_i^M)$$

The next approximation is:

$$u_{i+1}^M = u_i^M + c_{i+1}^M$$

And the iteration continues until F_i^N and c_{i+1}^M are sufficiently small and therefore neglected.

(Abaqus, 2010)

Figure 45 illustrates the nonlinear response of a structure to a small load increment with respect to its displacement. The objective of the algorithm is to get the final displacement of a structure given the load increment. For example, for the figure shown below a load P_1 is applied resulting in a displacement u_1 . To calculate the final displacement u_1 the program calculates a series of iterations. Starting with a displacement $u=0$, after the load increment, the initial tangent stiffness is K_0 and the load increment will be $\Delta P_1 = P_1$. This increment is going to generate a Δu , consequently

$$\Delta P_1 = K_0 \Delta u, \text{ where } \Delta u = 0 + u_A$$

For the load P_1 , the tangent of the curve at $u=0$ intersects at point a . This point corresponds to a displacement u_A which is the current estimate after the first iteration. The load P_1 minus the corresponding load for u_A , P_A , is called the residual force, R_A . In a nonlinear problem R_A will never be zero, so Abaqus/Standard compares it to a tolerance value. If R_A is less than the tolerance value, the program accepts the solution to be in equilibrium. However, the program also verifies that the last displacement correction, c_A , is small relative to the total increment displacement. If it does not comply Abaqus/Standard generates another iteration (Abaqus, 2010). Once the solution has converged for that time increment, it starts the second iteration. Keeping P_1 constant, the process starts taking the tangent to the curve at point A. Repeating the previous procedure, the tangent at point A intersects the load P_1 at point b. The corresponding displacement, u_B at this point has a load P_B . The difference P_1 minus P_B is the residual force R_B that is compared to the tolerance value as well as the c_B value compared to the Δu_B . If both values comply, the system is in equilibrium and it goes to the next increment, otherwise the program keeps performing further iterations until it reaches the equilibrium solution.

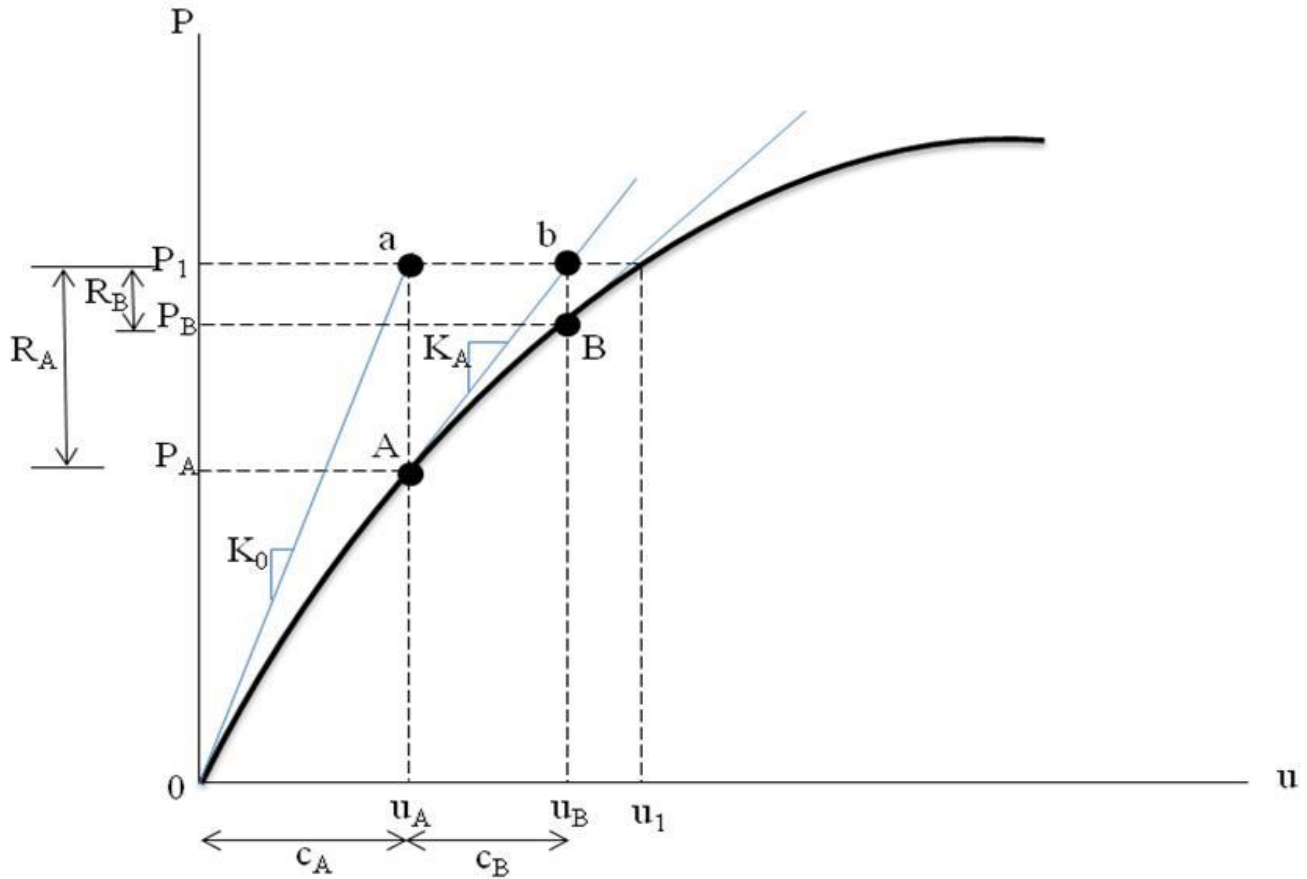


Figure 45: Nonlinear response of a structure subjected to a small load

4.2.2 Simulation of experimental procedure

The 3D numerical model of the Carlyle tainter gate recreates the procedures and conditions of the experiment. Ten steps were created to simulate the experimental procedure.

- Initial: This step is created automatically by Abaqus/CAE to allow the definition of boundary conditions, predefined fields, and interactions that will be applied at the beginning of the analysis.

- Gate on sill: The bottom edge of the skin-plate is restricted in the vertical direction (Z-axis) in the global coordinate system, to simulate the gate resting on the sill. The self weight (DL) and hydrostatic pressure (HP) loads are applied in this step and propagated until the last steps.
- Move up to 9.6-in: A displacement boundary condition of 9.6-in. in the global Z-axis is applied to the lifting beams of the gate. The cable pressure (CP) is applied in this step until the gate moves down to the sill.
- Stop at 9.6-in: The boundary conditions are restrained at the current position to stop the lifting of the gate.
- Move up to 16.8-in: A displacement boundary condition of 16.8-in. in the global Z-axis is applied to the lifting beams of the gate.
- Stop at 16.8-in: The boundary conditions are restrained at the current position to stop the lifting of the gate.
- Move down to 9.6-in: A displacement boundary condition of 9.6-in in the global Z-axis is applied to the lifting beams to lower the gate.
- Stop at 9.6-in: The boundary conditions are restrained at the current position to stop the lowering of the gate.
- Move down to sill: A displacement boundary condition of 0.0-in. in the global Z-axis is applied to the lifting beams to return the gate to the sill. The cable pressure is deactivated in this step.
- Stop at sill: Same boundary conditions and loads that the step Gate on sill.

The displacement boundary conditions were applied to the gate and the pin to simulate the lifting and lowering the gate. When the gate is at rest on sill, the bottom edge of the skin-plate was modeled pinned, restricting the directions normal and perpendicular to the surface. Only the self weight of the gate and the hydrostatic load were applied at this point. To lift the gate to the first position, 9.6-in., a displacement boundary condition was created applying the displacement in the vertical direction. The displacement was applied in the lifting beams near the bottom of the skin-plate. A similar boundary condition was applied to move the gate vertically to 16.8". The cable pressure load was added when the gate starts to move up and is propagated throughout the whole simulation, as well as the self weight and hydrostatic loads. To lower the gate the same procedure is applied. The boundary conditions in the stops also restricted the movements in the normal and perpendicular directions to reduce any residual movement from the step before.

The loads applied to the Carlyle Gate numerical model were based on the ones applied to the actual gate in the experimental procedure. The considered loads were the self weight of the gate, the hydrostatic load and the lifting cable pressure. The computation of the loads was based on basic fluids and engineering mechanics. Since the lifting and lowering of the gate was sufficiently slow, all the loads were considered to be static.

1. Gravity load: To consider the self weight of the structure, a gravity load was applied to the numerical model of the gate. The mass density of the steel was calculated dividing the density of the steel over the gravitational acceleration.
2. Hydrostatic load: For the hydrostatic load computation various factors were taken into consideration. One of them was the water level of the dam the day of the experimental procedure. For this parameter a reference picture that illustrates the height of the water was taken to obtain this value. From Figure 46 the water level at the upstream of the

gate a little over the second horizontal girder. From the As-build drawings, the distance from the bottom of the gate to the second horizontal girder is 16ft.



Figure 46: Water elevation in experimental procedure. Picture from the experimental procedures performed by Dr. Gopalaratnam and Dr. Riveros in the Carlyle Lake Dam.

The equation used to calculate the hydrostatic pressure in the skin-plate of the gate was

$$P = \gamma H \quad 4.3$$

Where,

P = hydrostatic pressure at height, psi

H = height of the water level upstream of the gate, in

γ = unit weight of water, lb/in³

3. Lifting cable load: To calculate the lifting cable pressure, the tension in the lifting beams was required. The tension in the lifting cables was calculated taking the weight of the moving parts of the gate, which was taken from the As-built drawings, and dividing it between four points which are the two cables that lift the gate and the two pins that support the end frame of the gate. The equation to calculate the pressure from the cable in the skin-plate was taken from the Engineering Manual, Design of Spillway Tainter Gates.

$$w = T/R \quad 4.4$$

Where,

w = cable pressure, lb/in

T = tension in the lifting beams, lb

R = radius of the gate, in

To convert the linear load into pressure the total was divided over the width of the cable.

4.2.3 Interaction simulation

For the interaction simulation between the pin and the hub the penalty formulation method was used. This method is based on the Amontons-Coulomb friction model. The first section introduces a review of the theory of solid friction and the second section explains in detail the interaction formulation.

4.2.3.1 Theory of solid friction

Friction is a resistance of movement that occurs when one body interacts over another body. These interactions can be between a gas and a solid, a liquid and a solid or between two solids (Blau P., 1992). In this research only the interaction of two solids will apply, specifically between the pin and the trunnion of the gate (steel to steel contact). The friction phenomenon is responsible for the dissipation and loss of energy, this behavior can help or affect the overall performance of a structure depending on the case. The dissipation of energy sometimes can be translated into the wearing of the material and deformations that will affect the performance of the structure.

There are several solid friction theories that have been developed throughout the years. The most used friction model and the one used in this study is the Amontons-Coulomb friction model. This model states that

$$F_{s,max} = \mu_s \times N \quad 4.5$$

$$F_k = \mu_k \times N \quad 4.6$$

Where,

$F_{s,max}$ = maximum static friction force, N (kip)

F_k = kinetic friction force, N (kip)

N = normal force, N (kip)

μ_s = static coefficient of friction

μ_k = kinetic coefficient of friction

From the equation above, $F_{s,max}$ is the maximum friction force right before an object starts moving and F_k is the frictional force when the object is in motion. N is the normal force and μ is the coefficient of friction. This last parameter, μ , is the proportionality constant between the

friction force and the normal force. There are two coefficients of friction, the static, μ_s , and the kinetic, μ_k . The static coefficient is the relation between the forces required to start moving an object from rest with respect to the normal force and the kinetic is the relation between the forces that is required to keep the object in motion with respect to the normal force. Usually the static coefficient of friction is greater than the kinetic because it takes more work to start moving an object than to keep it moving. Before the object starts moving the force is called the static force and the static coefficient of friction is used. When the static force reaches a maximum value it means that the object is going to start moving and the kinetic coefficient of friction should be applied.

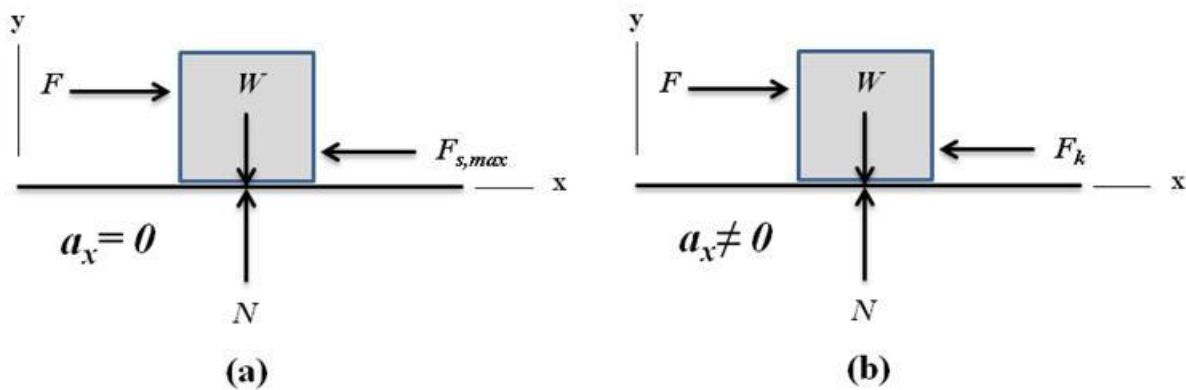


Figure 47: Load schematic (a) static case, (b) kinetic case

Figure 47 demonstrates the difference between the static friction force and the kinematic friction force. The block in Figure 47(a) is subjected to a force that is not large enough to move the object, so the acceleration is zero and the static friction coefficient is used. In Figure 47(b) the block starts moving because the force is larger than the friction resistance; therefore the kinematic friction coefficient will be applied.

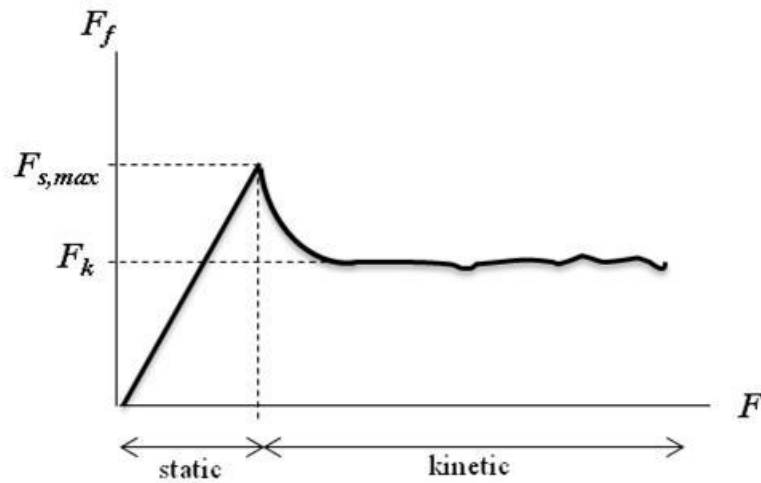


Figure 48: Friction Force vs. Applied Force

Figure 48 illustrates the typical behavior of the friction force versus the applied force. The first part of the curve, the static region, there is a linear behavior between the two loads, indicating that the friction coefficient is constant. The significant drop right after the linear slope means that the applied load over passed the friction force and the object started moving. The friction coefficient in this region is not constant. Figure 48 also shows that the kinematic friction force is less than the static friction force because the required force to keep the element moving is less than the force required to start the movement from rest.

Although existing literature assumes identical coefficient of friction in every point of the contact surfaces, this parameter varies from one point to the other inside the contact surfaces and throughout time (Vadivuchezhian *et al.*, 2011). The magnitudes of these coefficients depend on the nature and condition of the surfaces in contact.

4.2.3.2 Friction formulation

To simulate the friction between the pin and the hub in the finite element analysis an interaction property was defined between the two surfaces. An interaction consists of two components, one normal to the contact surface and the other tangential. The tangential component contains the frictional stresses of the contact. These stresses are responsible for resisting the sliding motion between the surfaces. Abaqus uses the Coulomb friction model to describe this interaction, which characterizes the friction behavior with a coefficient of friction, μ . The tangential motion in the program is zero until it reaches a critical shear stress value that depends on the normal contact pressure (Abaqus, 2010).

$$\tau_{crit} = \mu p$$

Where,

τ_{crit} = limiting frictional stress for the contact surfaces

μ = coefficient of friction

p = contact pressure

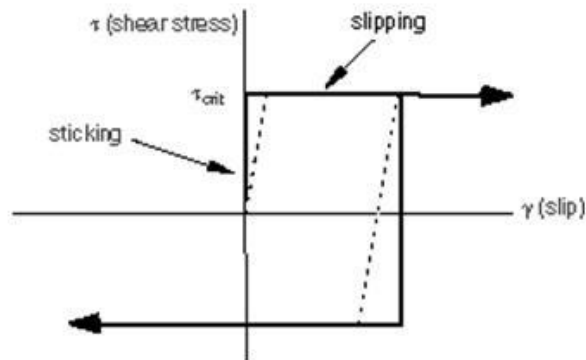


Figure 49: Coulomb friction model, from Abaqus Documentation.

Figure 49 describes the behavior of the coulomb friction model. When there is no slip the shear stresses are zero, this condition is identify as sticking. Once the surfaces reach the critical shear stress, μp , the surfaces start slipping.

When defining interaction properties in Abaqus CAE there are several behaviors that can be define. For the particular case of the pin and the hub an interaction was define with both the normal and tangential behavior. The tangential behavior contains the friction properties for the simulation. The friction formulation chosen for this analysis was the penalty method because it allows a level of relative motion between the surfaces as oppose to the rough formulation were an infinite friction coefficient is assumed or the Lagrange multiplier formulation which defines that there is no relative motion and add more degrees of freedom.

5 EXPERIMENTAL VALIDATION, TRUNNION FRICTION STUDY AND PARAMETRIC ANALYSES

5.1 Experimental Validation

From the experimental results it can be concluded that the most critical stresses occur when the gate starts to open and when it goes down. This behavior can be attributed to the elasticity of the lifting cable and the breaching of the static friction when the gate starts to rotate. Since the cable is not fully tensioned right before it starts to lift the gate, the instant pull in combination with the exerted pressure generates an initial jump either in tension or compression depending on the locating of the gages. Another conclusion about the experimental results is that the structure is subjected to unsymmetrical loading due to the lifting cables and/or different friction coefficients in each trunnion bearing.

In the experimental procedure, the gages were set to zero before the experiments began, not measuring the initial strains caused by the self weight and the hydrostatic loads. For the calibration of the numerical model the dead and hydrostatic loads were applied since the beginning of the procedure, thus generating initial strains. These strains were set to zero to make a more appropriate comparison with the experimental results. The plots were shifted by subtracting the initial strain magnitude, thus applying equally the same factor to all the values.

For each element a local coordinate system had to be created to obtain the axial strains (E11). To get a general idea of the behavior of the elements and compared them between each other, the gages were grouped by the location. In the top strut arms were located the gages 1, 2, 9 and 10. The bottom strut arms have gages 3, 4, 11 and 12. The diagonal bracings close to the skin-plate have the gages 7, 8, 15 and 16 and in the second diagonal bracings from the skin-plate

are gages 5, 6, 13 and 14 (Figure 32). The overall behavior of the numerical results was symmetric depending on the location of the gages.

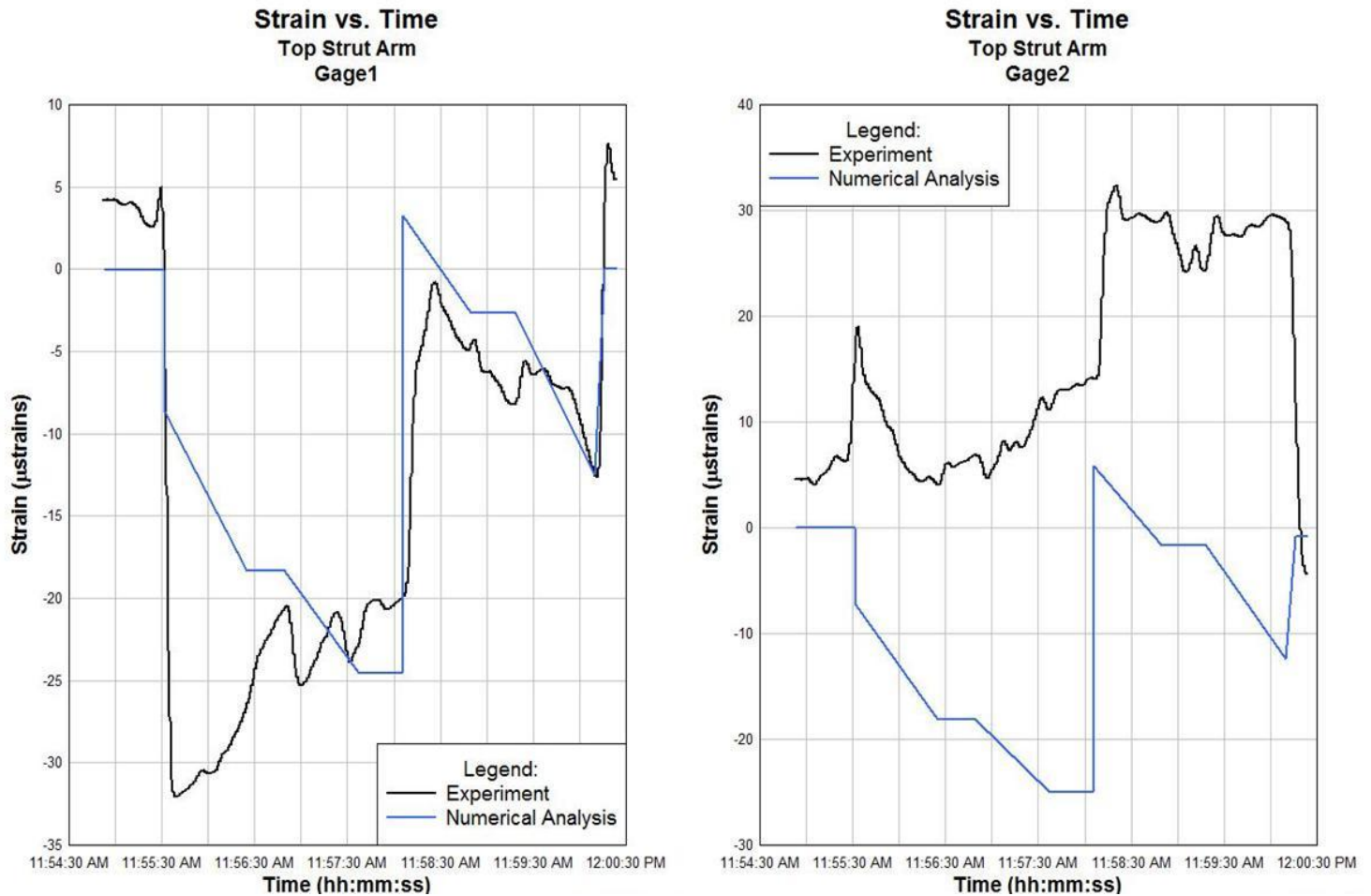


Figure 50: Experimental Results vs. Numerical Analysis from the Left Top Strut Arm Gages.

Figure 50 illustrates the comparison between the experimental results and the numerical analysis for the gages located at the top strut arm flanges of the left side of the gate (gages 1 and 2). In general, the results from the numerical analysis have the same behavior in both gages because the model was created with geometrical and loading symmetry. When the gate model begins the third step (gate moving up), there is an initial compression in the numerical analysis results (blue line) due to the applied cable pressure. This behavior can also be attributed to the

release of the boundary conditions of the bottom of the skin-plate which are now applied to the lifting beams to move the gate. As the gate goes up, the strains continue to increase in compression because the top strut arms are receiving more load from the weight of the skin-plate. Figure 51 illustrates how as the gate moves up the center of mass of the structure moves closer to the trunnion pushing the top strut arms. This behavior continuous until the gate starts to move down. There is an instant jump in tension when the gate changes direction because the self weight is now acting in the same direction as the gravity load thus producing the tension in the top strut members. As the gate moves down the strains start to increase in compression even though the center of mass of the gate is moving away for the trunnion but the cable start to wrap again the skin plate (Figure 51).

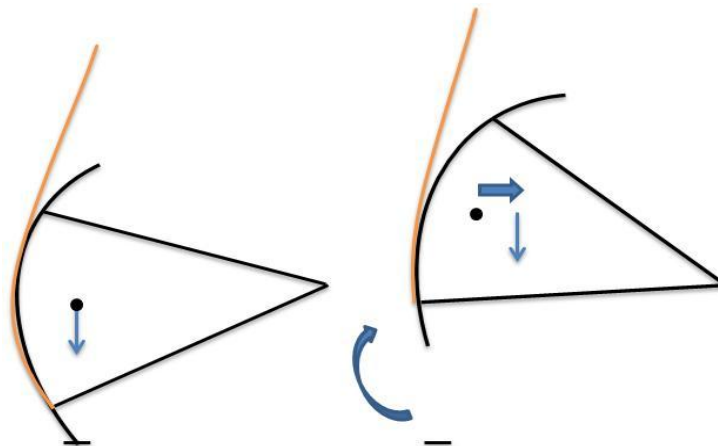


Figure 51: Simulation of the lifting of the gate

Comparing the experimental results with the numerical analysis they have a similar behavior and overall magnitudes. Since the numerical model was created with geometric and load symmetry the behavior of the gages located in the same area are going to be the same. There are some discrepancies between the numerical model and the experimental results. First to notice is how the gage 1 has initially compresses and gage 2 tenses when the gate start to move up. The

jump in tension at the beginning of the experiment produced by the pull of the cable was not replicated in the model because of the complexity of its computation. In addition, the lack of experimental data from the cable material properties and strains during the execution of the experiment contributed to the omission of this simulation. Gage 1, shown in Figure 50, has a positive slope when the gate starts to open as oppose to the negative slope from the numerical results. Gage 2 (Figure 50) has the same behavior as the numerical results from gage 1 but looks slightly different from the experimental results, especially when the gate is lifted for the second time. This behavior can be attributed to asymmetric loading of the lifting cables.

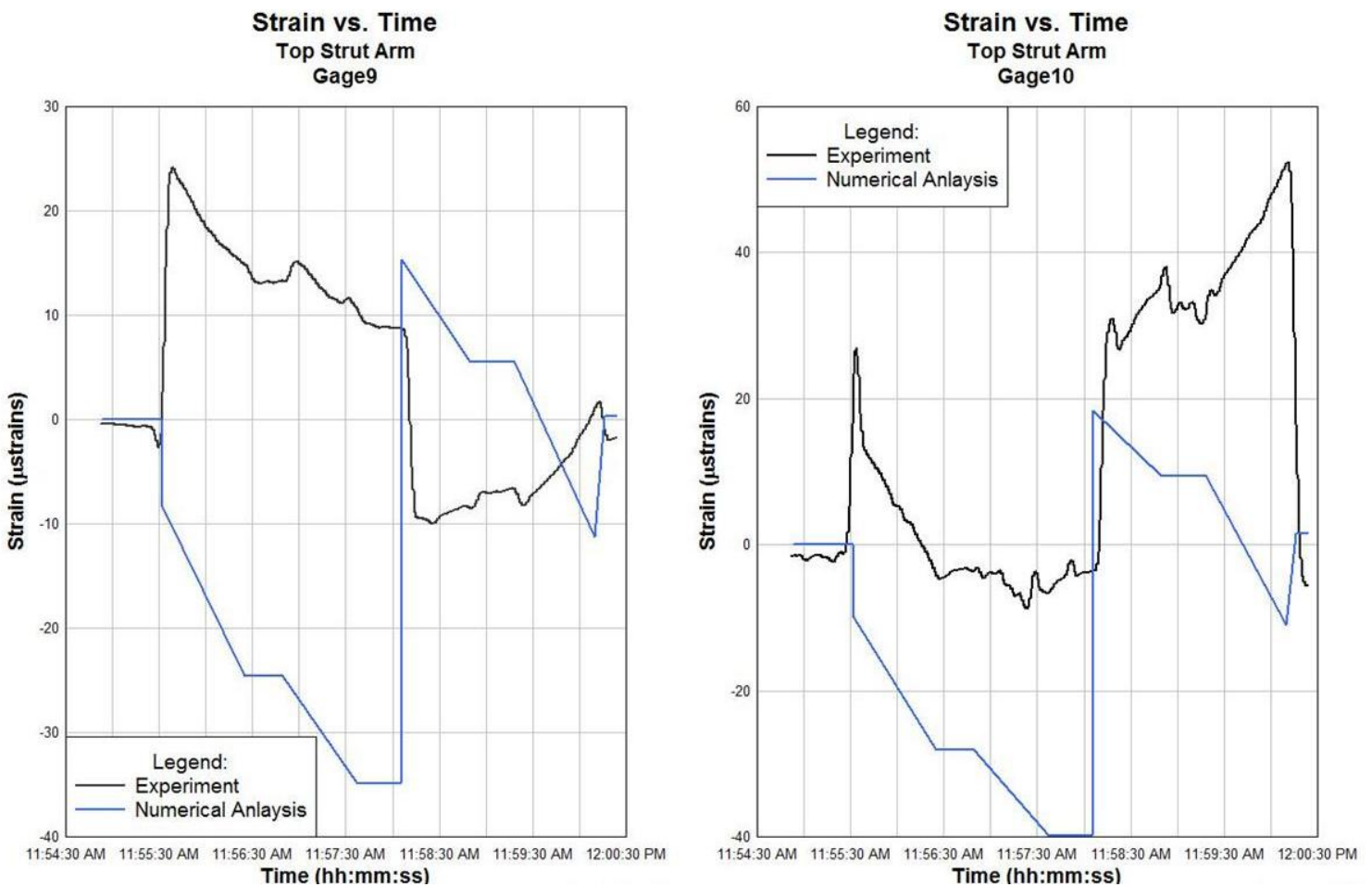


Figure 52: Experimental Results vs. Numerical Analysis from the Right Top Strut Arm Gages

The numerical analysis results from gages 9 and 10 (Figure 52), located in the top struts from the right side of the gate, also illustrate a similar behavior to the numerical analysis results from the gages 1 and 2. Comparing these gages with the experimental results it can also be concluded that they have a similar behavior and overall magnitudes.

When comparing with the experimental results gages 2, 9 and 10 have the same slope when the gate starts to move up. The reason why gage 1 has an opposite behavior to the analytical results is because the geometry and the loads applied to the model are symmetric; therefore the behavior is expected to be symmetrical as oppose to the experimental scenario in which the loads may not be completely symmetric. As the gate moves down, gages 9 and 10 illustrate the same behavior with a positive slope which means that the element is decreasing in compression.

Comparing the cross section diagrams from the numerical analysis results of the top strut gages (Figure 53), it is noticeable that there is not a considerable amount of bending in the elements. The reason is because the loads are applied symmetrically not producing eccentricities that cause bending in the elements. The axial forces and bending moments can be calculated as shown in Figure 35.

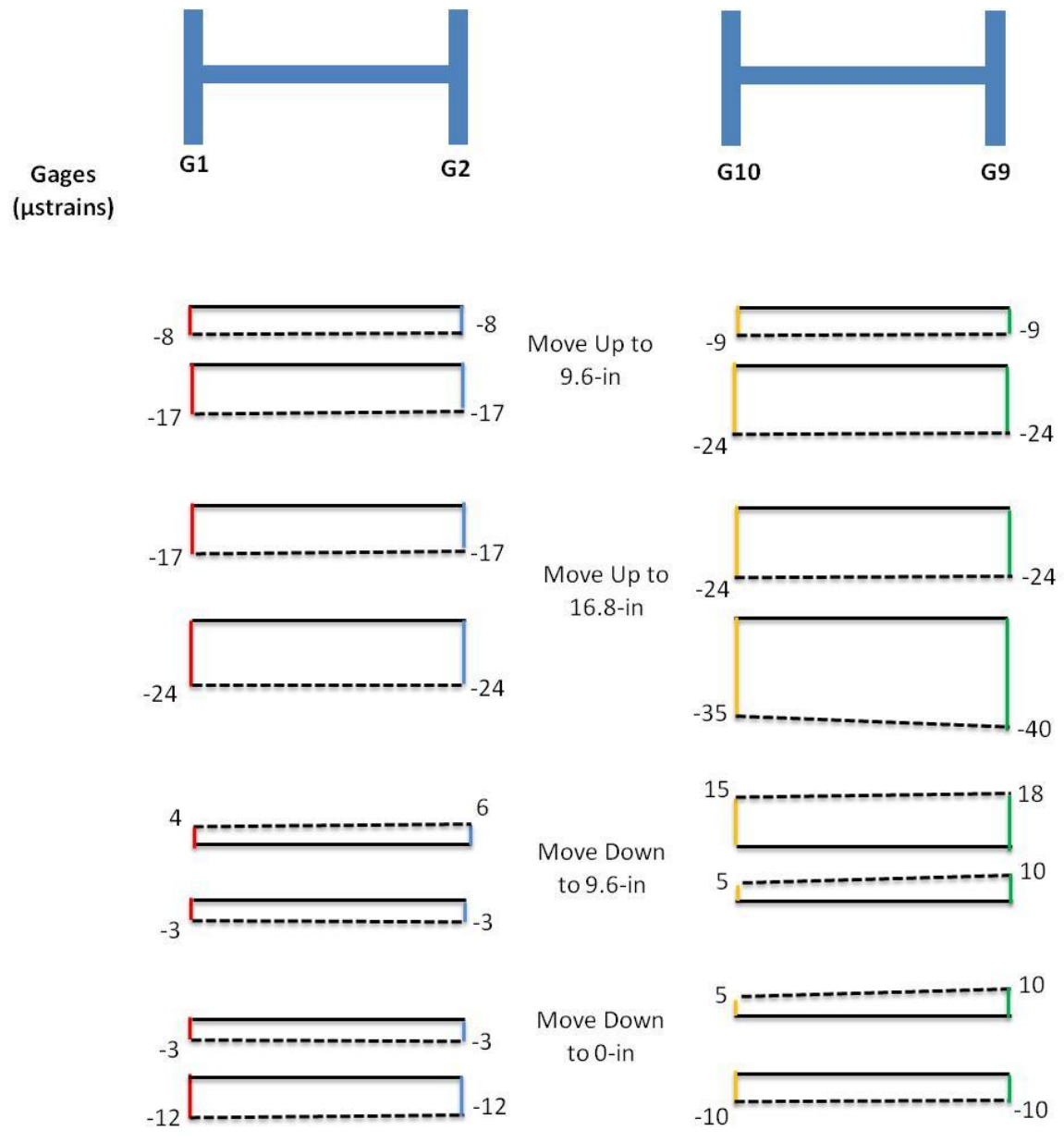


Figure 53: Cross section strain diagram from numerical analysis for top strut arms

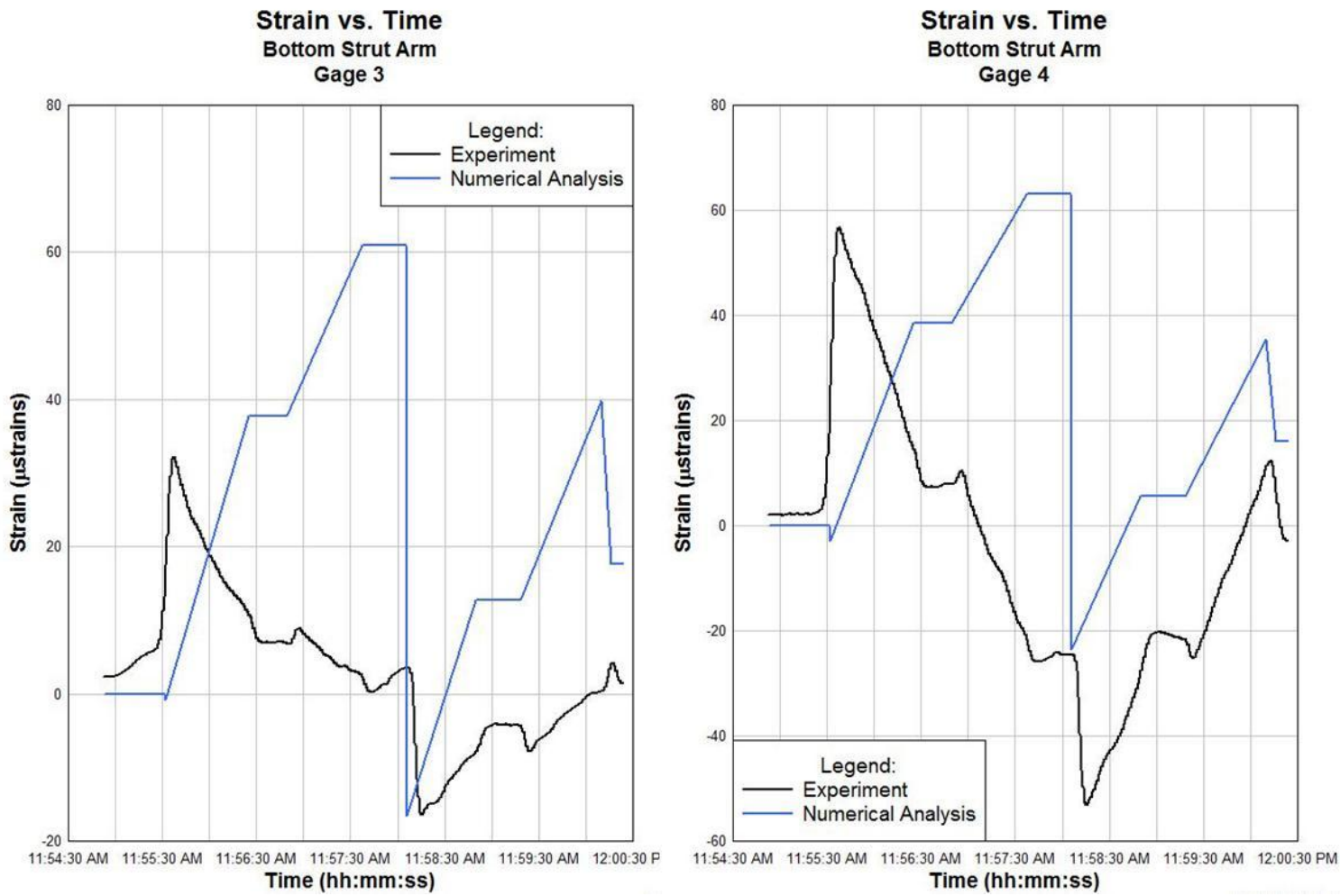


Figure 54: Experimental Results vs. Numerical Analysis from Left Bottom Strut Arm Gages

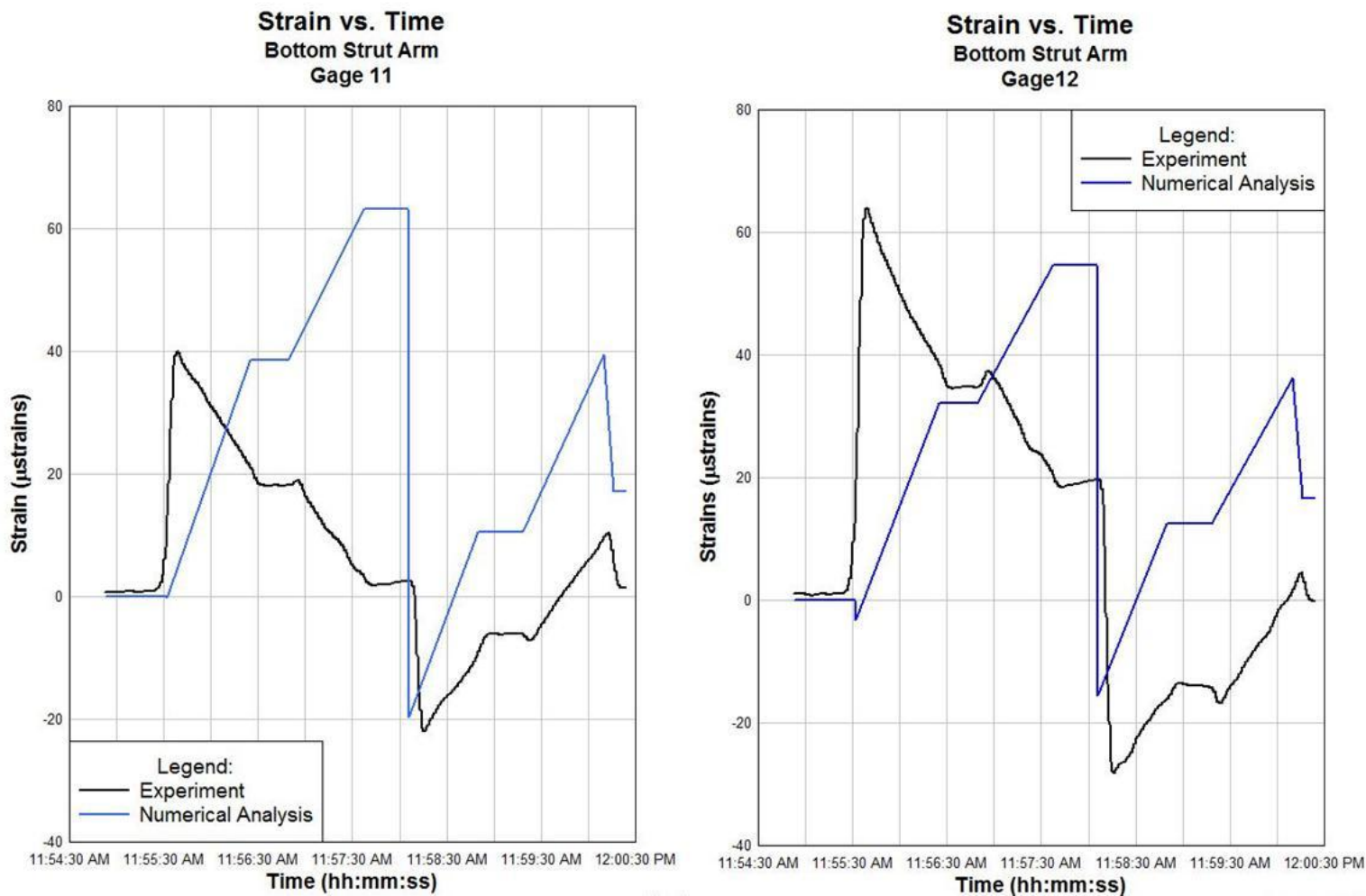


Figure 55: Experimental Results and Numerical Analysis from the Right Bottom Strut Arm Gages.

The analytical results from bottom strut gages have a similar behavior between each other throughout the simulation. Gages 3 and 4 (Figure 54) are located in the left bottom strut arm and gages 11 and 12 (Figure 55) in the right bottom strut arm. When the gate starts to open there is an increase in tensile strains because the lifting mechanism is near the bottom struts thus when the gate is lifted these bottom member are in tension. In this step the numerical behavior is different from the experimental results because the instant pull generated by the lifting cable was not included in the simulation of the 3-D numerical model. As the gate moves up the strains

from the numerical analysis continue to increase in tension as the hydrostatic load decreases as the gate is lifted. The first part of the simulation is different from the experimental results because the initial pull generated by the cable was not modeled, therefore, they do not have to release that initial tension, which is what happens in the experiments. When the gate starts to move down both the numerical analysis and experimental results have a positive slope meaning that the element is reducing its compression (increasing in tension).

As well as the cross section diagrams from the top strut gages, Figure 57 illustrates how there is almost no bending in the bottom strut arms. The strain magnitudes in these elements are higher because they are carrying the hydrostatic load. The top strut gages are less affected by the hydrostatic load because the water level in the experimental procedures was at the middle of the skin-plate elevation (Figure 56).

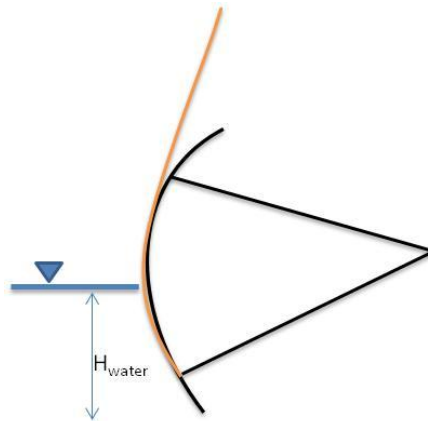


Figure 56: Water elevation for the experimental procedures

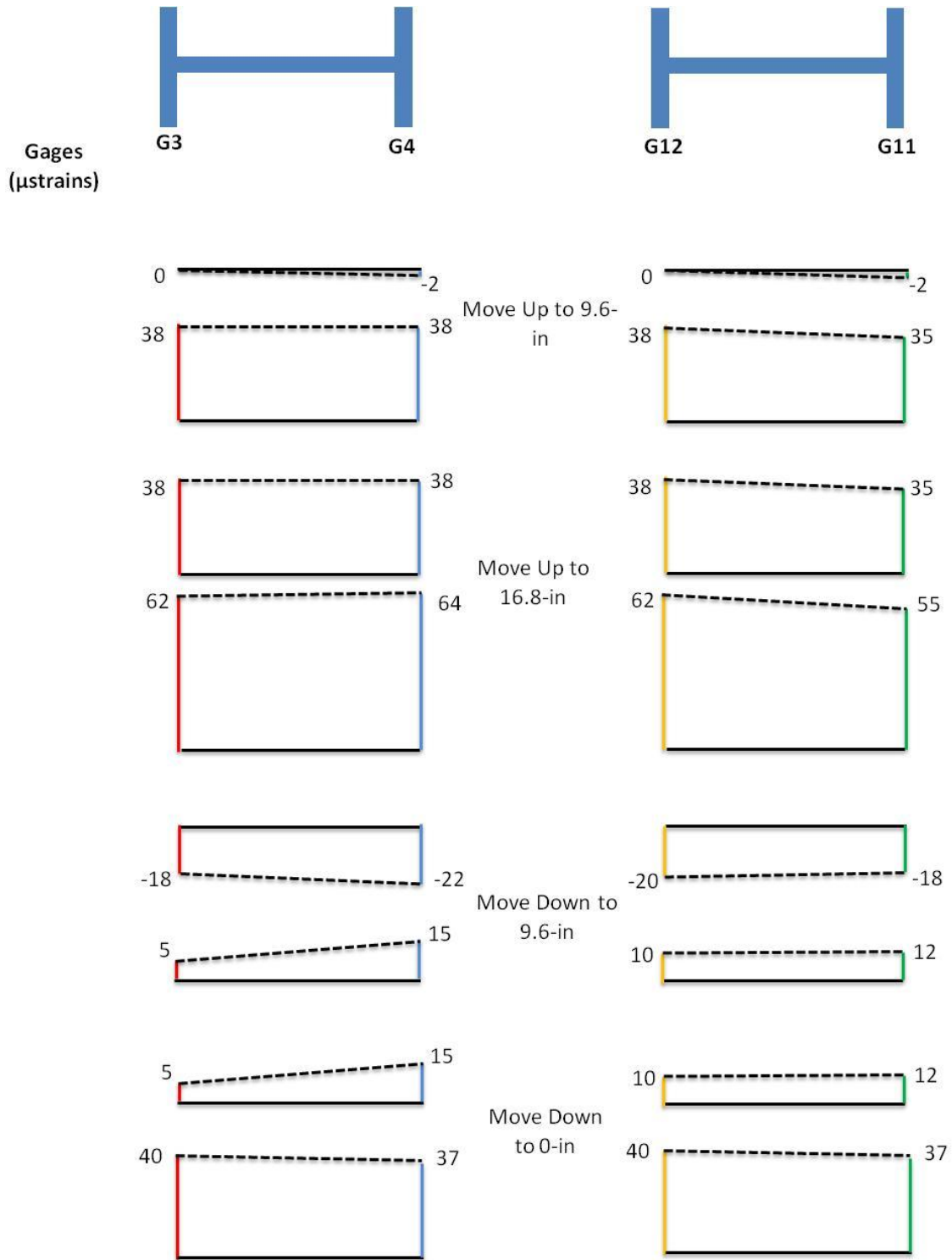


Figure 57: Cross section strain diagram from numerical analysis for bottom strut arms

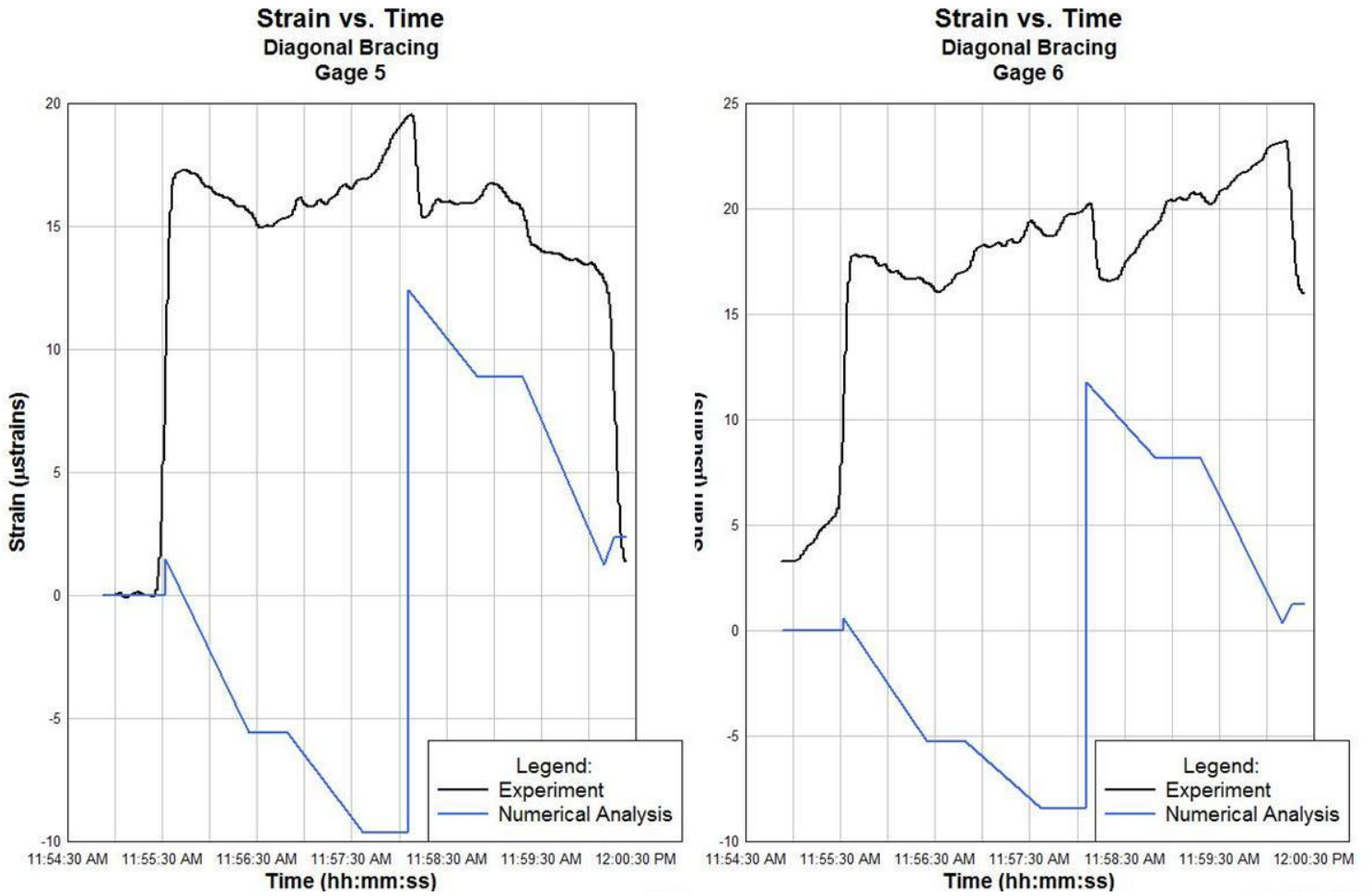


Figure 58: Experimental Results and Numerical Analysis for the Left Diagonal Bracings.

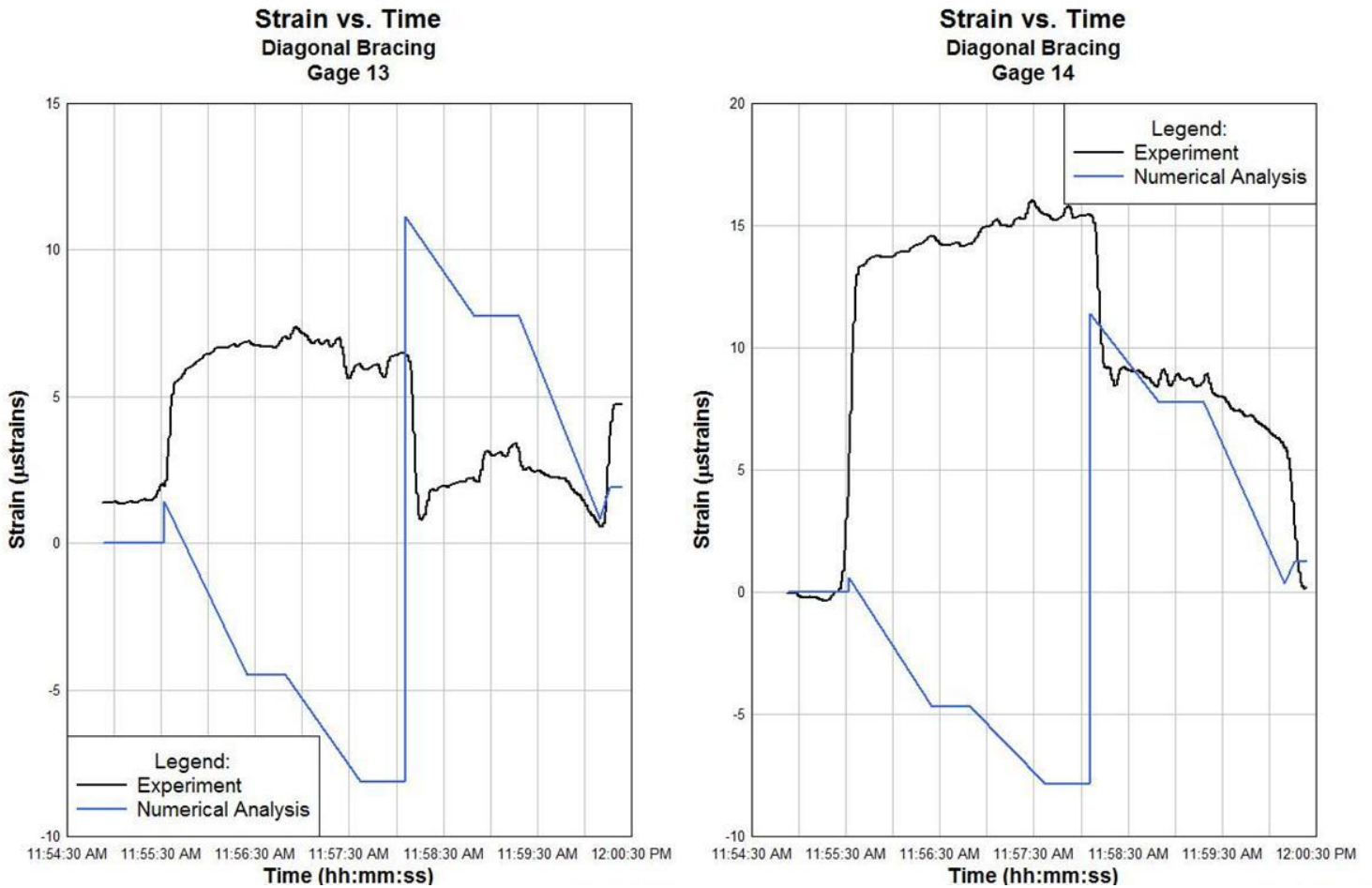


Figure 59: Experimental Results and Numerical Analysis for the Right Diagonal Bracings.

The numerical analysis results from the diagonal bracings show a similar behavior to the results from the top strut gages with the difference that there is a small increase in tension at the beginning of the simulation. That initial tension can also be seen in the experimental results but at a larger rate. The major difference between the numerical analysis and experimental results is when the gate starts to move down. The numerical results show an abrupt increase in tension while the experiments illustrate a less significant change in strain magnitudes. Even though the comparison between the numerical analysis and the experimental results is considerable when

looking at the change in magnitudes in the diagonals is about one quarter of the change in strain magnitudes in the strut arms.

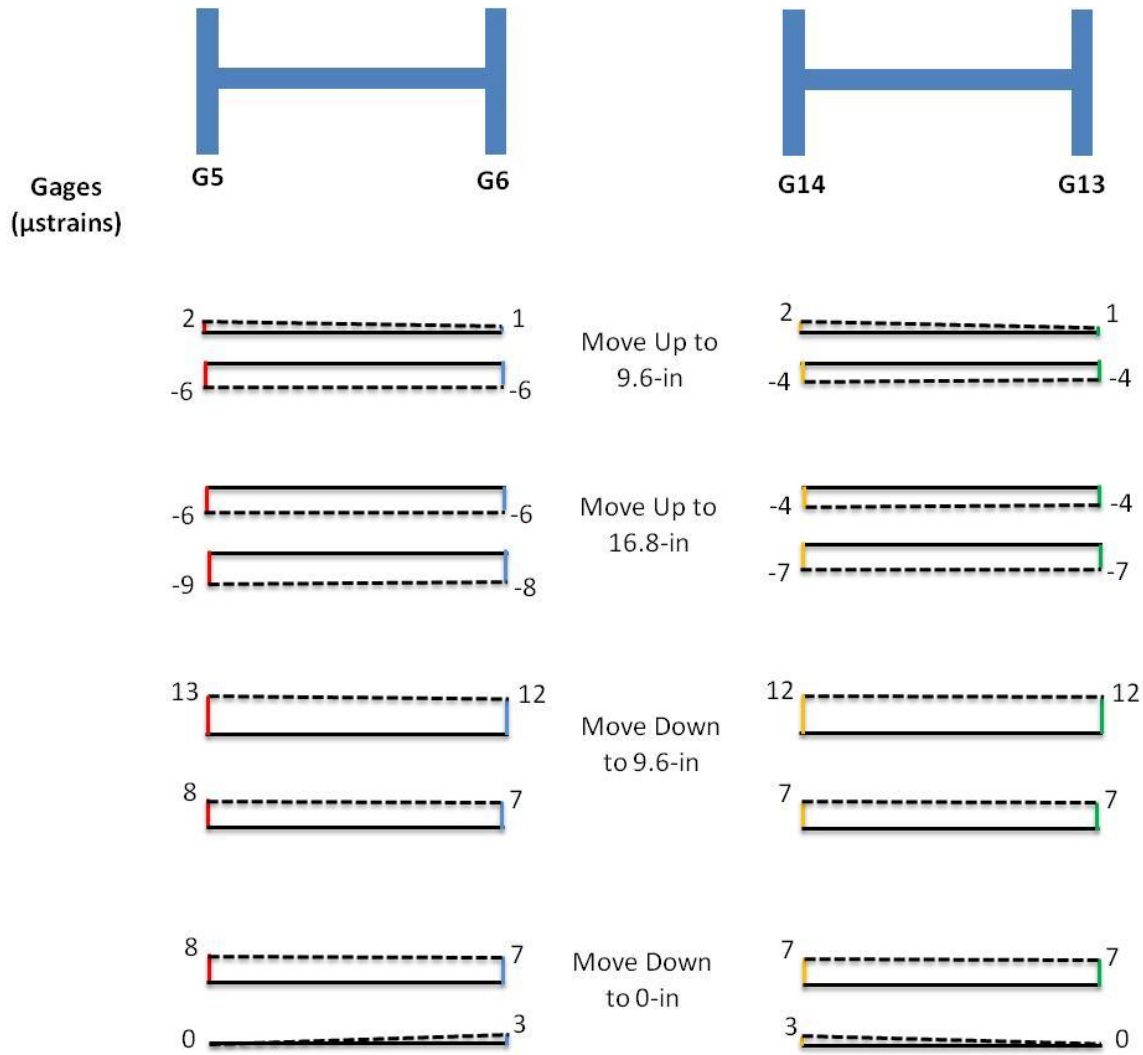


Figure 60: Cross section diagrams from numerical analyses results for the diagonal bracings

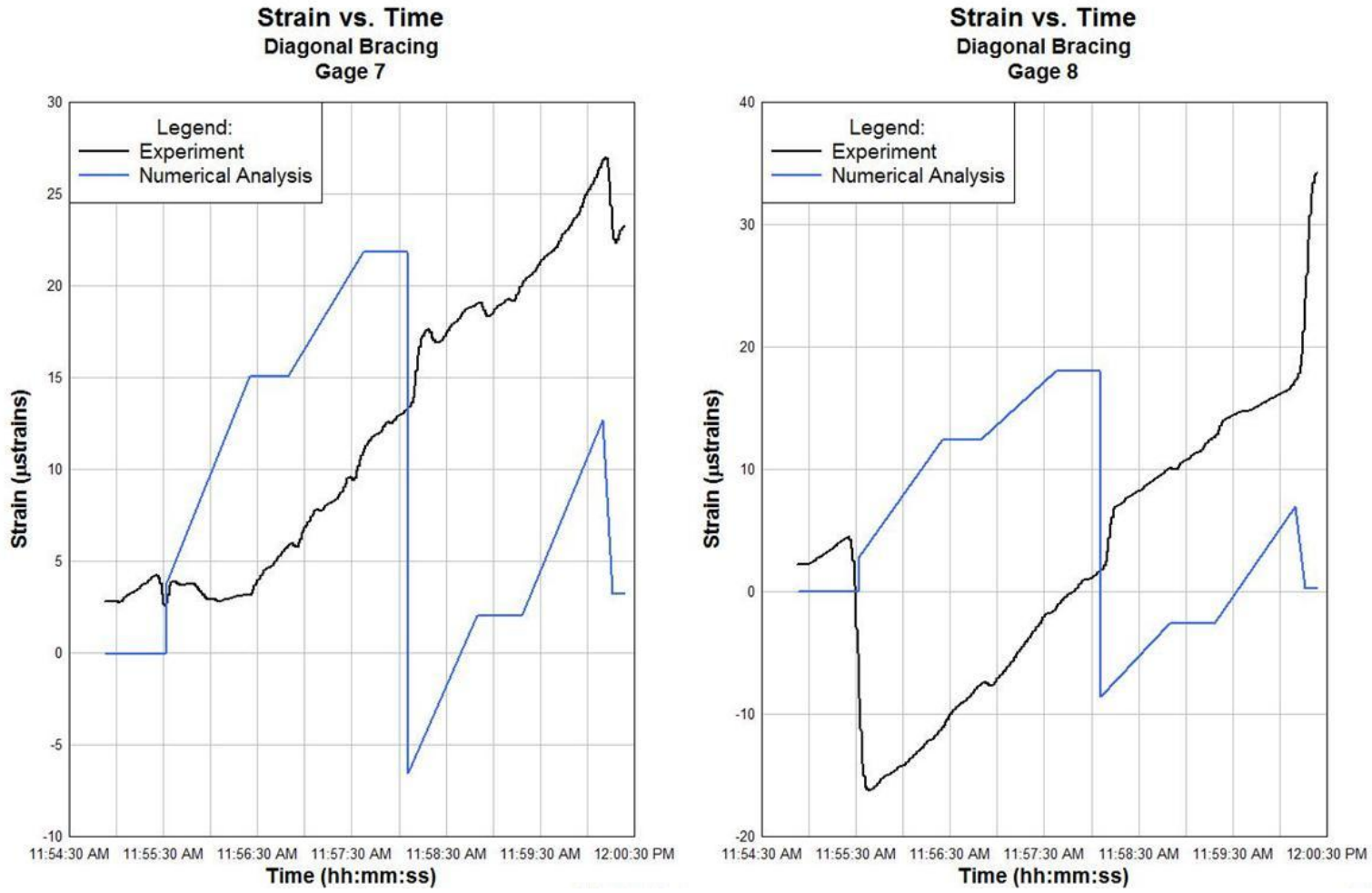


Figure 61: Experimental Results and Numerical Analysis for the Left Diagonal Bracings closer to the Skin-plate

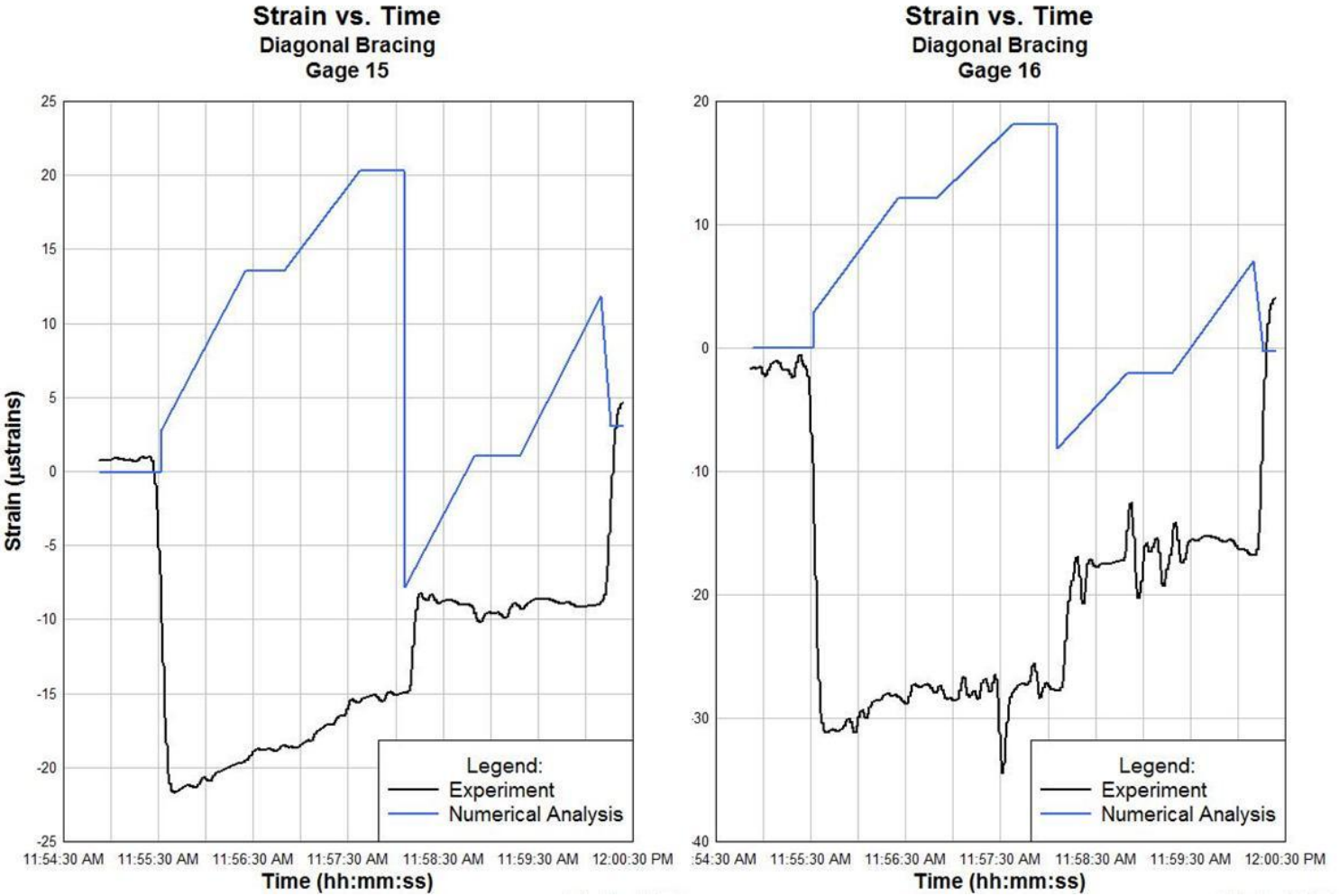


Figure 62: Experimental Results and Numerical Analysis for the Right Diagonal Bracings closer to the Skin-plate

The gages 7, 8, 15 and 16 that are located in the diagonal bracings closer to the skin-plate show a similar behavior to the bottom strut arm gages but with smaller magnitudes. Comparing the experimental results with the numerical analysis, both shown tension in the element as the gate is moving up as well as when the gate is moving down.

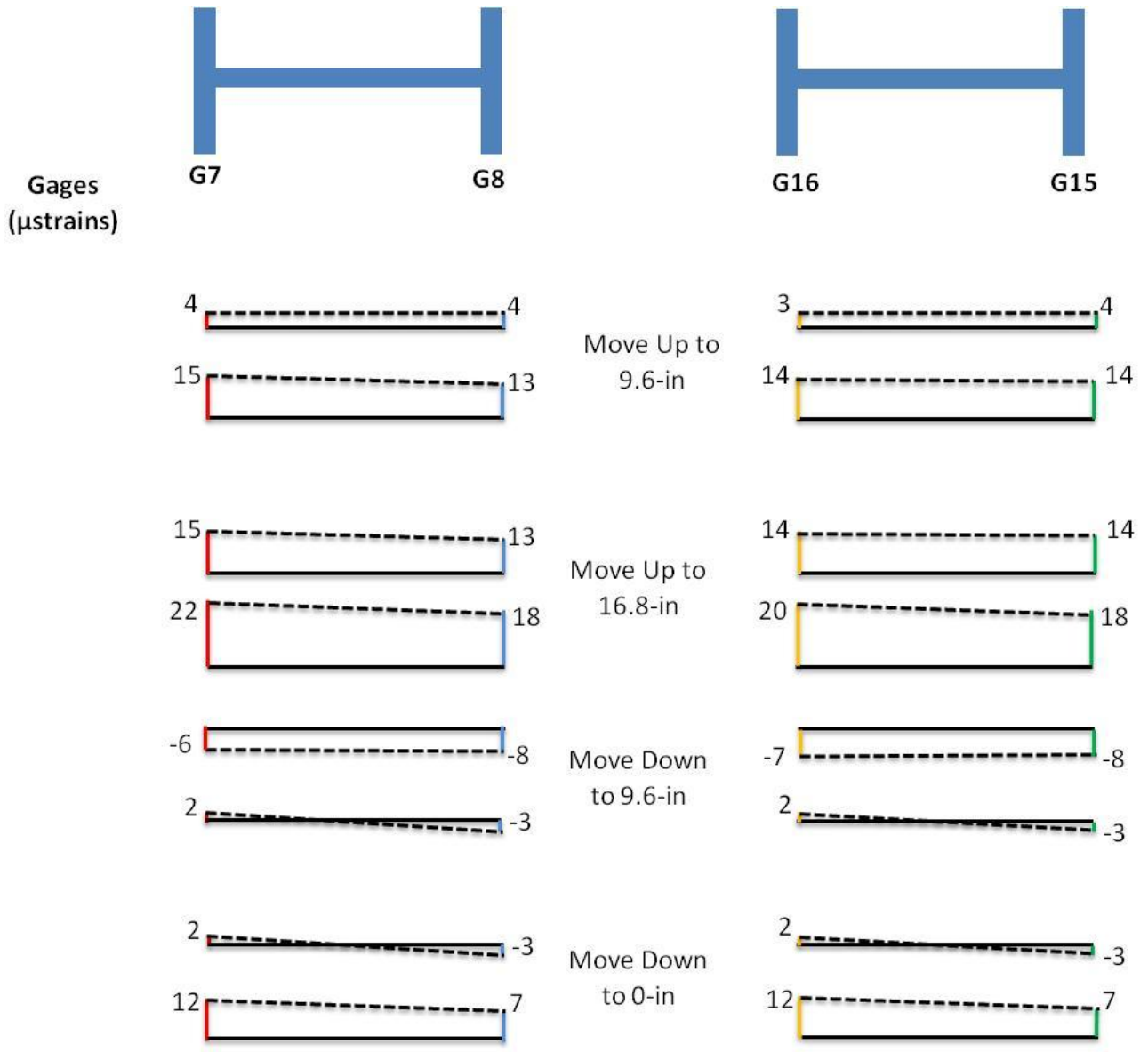


Figure 63: Cross section strain diagram from numerical analyses for diagonal bracings closer to the skin-plate

The cross section strain diagrams for all the diagonal bracings (Figure 60 and Figure 63) illustrate how the members have small bending and the strain magnitudes compare to the struts are also considerably low.

5.2 Trunnion Friction Study

5.2.1 Friction Sensibility Analysis

To better understand the effect of the increase in friction coefficient in the elements the elements of the gate, a friction sensibility study was performed. In this study the friction coefficient in both pins was varied uniformly from frictionless to 0.3. For this study the same simulation as the calibration of the model was used to determine the closest value of friction coefficient in the trunnion area for the Carlyle tainter gate under the conditions of the experiment performed in 2008.

Figure 64 presents the plots from the variation in the friction coefficient of gage 1 and gage 4 as a representation of the top strut and bottom strut gages respectively. The overall behavior of the strains with respect to the time was similar in all the gages, as the friction coefficient decreases the magnitude of the strains are smaller. A very important detail from the plots is the significant reduction in the jump when the gate starts to move down, at the point at which it can change from compression to tension. This means that breaching of the static friction when the gate is moving down contributes considerably to the drastic change in strains from the experimental procedures.

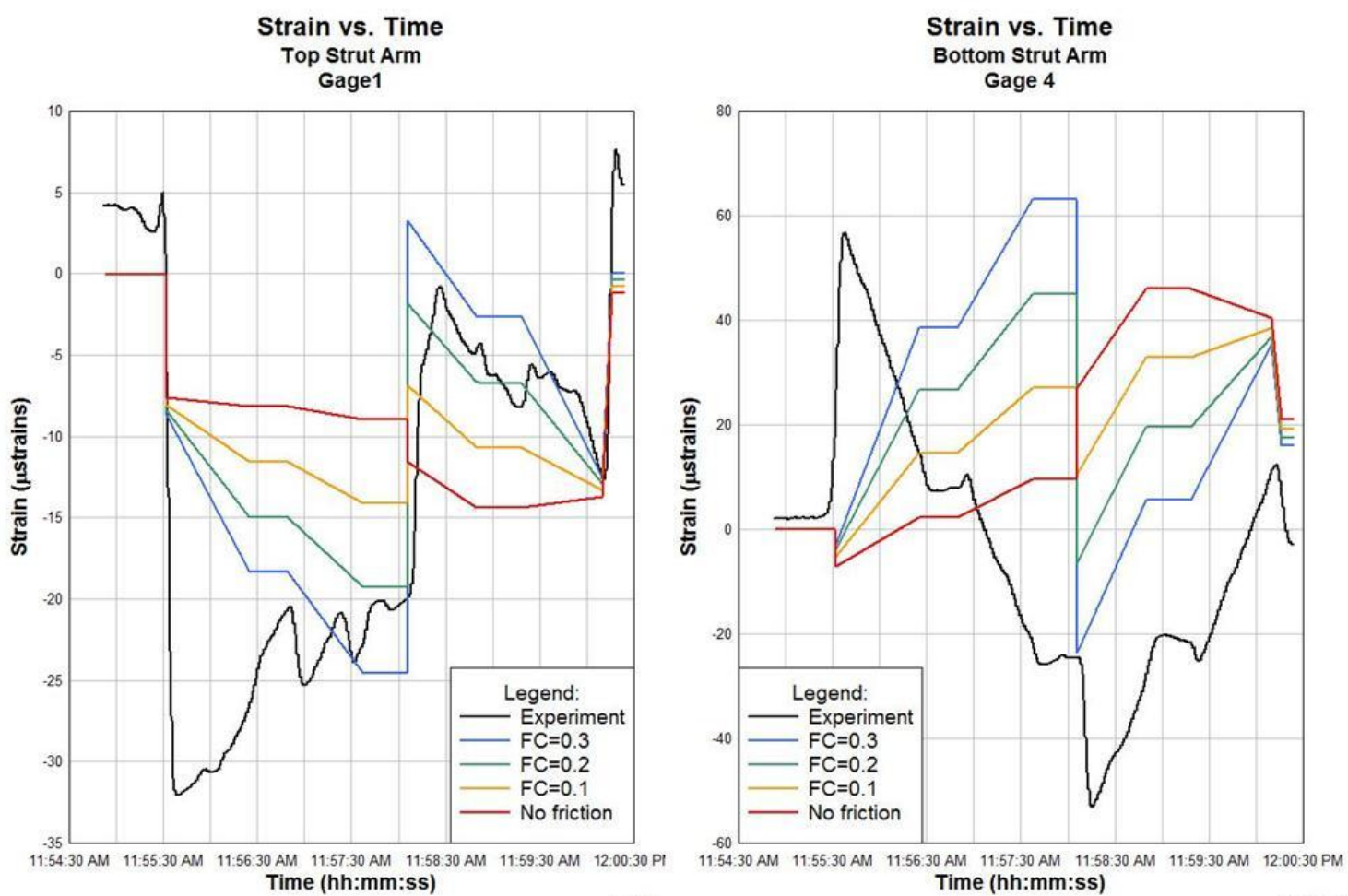


Figure 64: Friction sensibility study for gages 1 and 4.

Figure 65 illustrates the variation in friction for the gages located in the diagonal struts. Looking at the behavior of the analyses it is noticeable that with no friction (red line), the numerical analysis results simulate better the experimental results, for both gage 5 and gage 7. This behavior indicates that in the experiment the diagonal bracings closer to the skin-plate were not as affected by the friction in the trunnion as the strut arms.

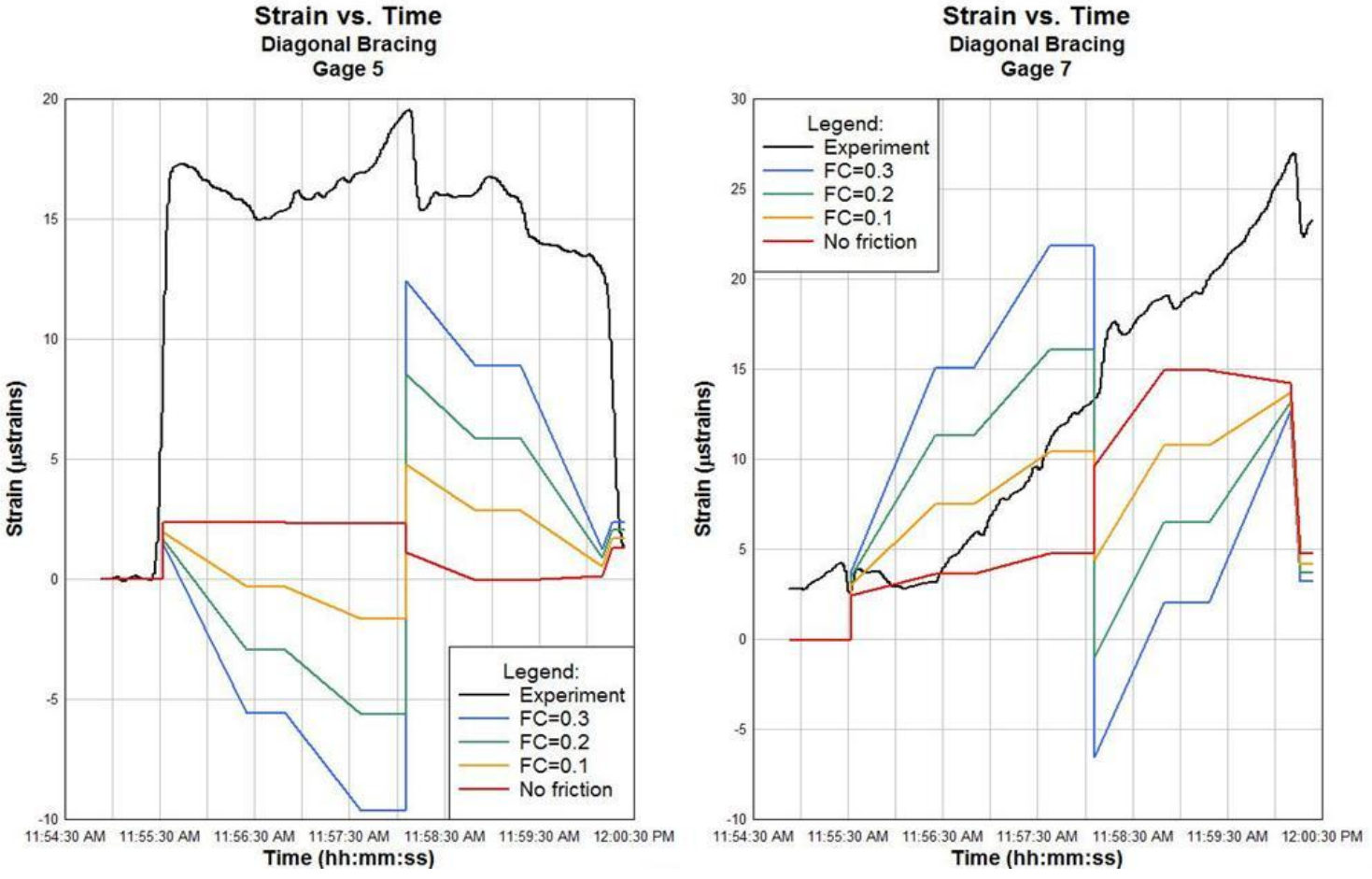


Figure 65: Friction sensibility study for gages 5 and 7.

From the 3-D numerical model the higher Von Misses stresses occur near the trunnion area, in the connection between the hub and the flanges from the trunnion gusset plates when the gate is stopped at 16.8-in (Figure 66). There is a change in geometry in this area that causes a concentration of stresses. Considering the yielding criteria the highest value of von misses stress is 30-ksi which is smaller than the yielding stress for this steel, therefore the structure is under a good condition. **Error! Reference source not found.** This behavior fulfills it expectations considering that all the loads are transferred through the end frame to the hubs. Even though this area contains the higher strains, the structure is less likely to fail at this point. The most

vulnerable member of a tainter gate subjected to high friction coefficients in the trunnion are the end frame members located close to the trunnion area as shown in Figure 67. The evidence is the failure from Folsom Dam which initial point of failure was the diagonal bracing closer to the trunnion area (Figure 4).

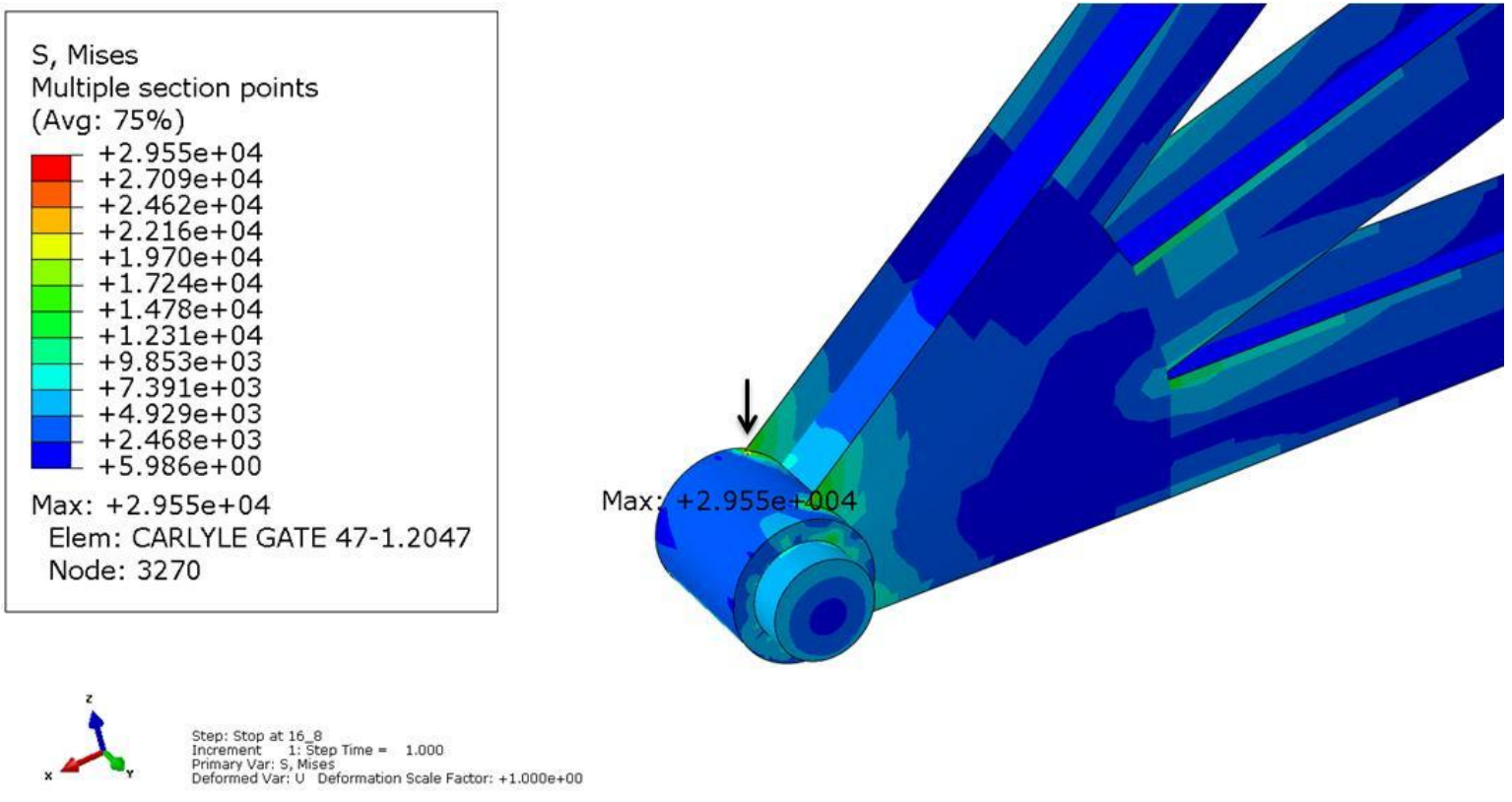


Figure 66: Von Misses stresses when the gate is stopped at 16.8-in

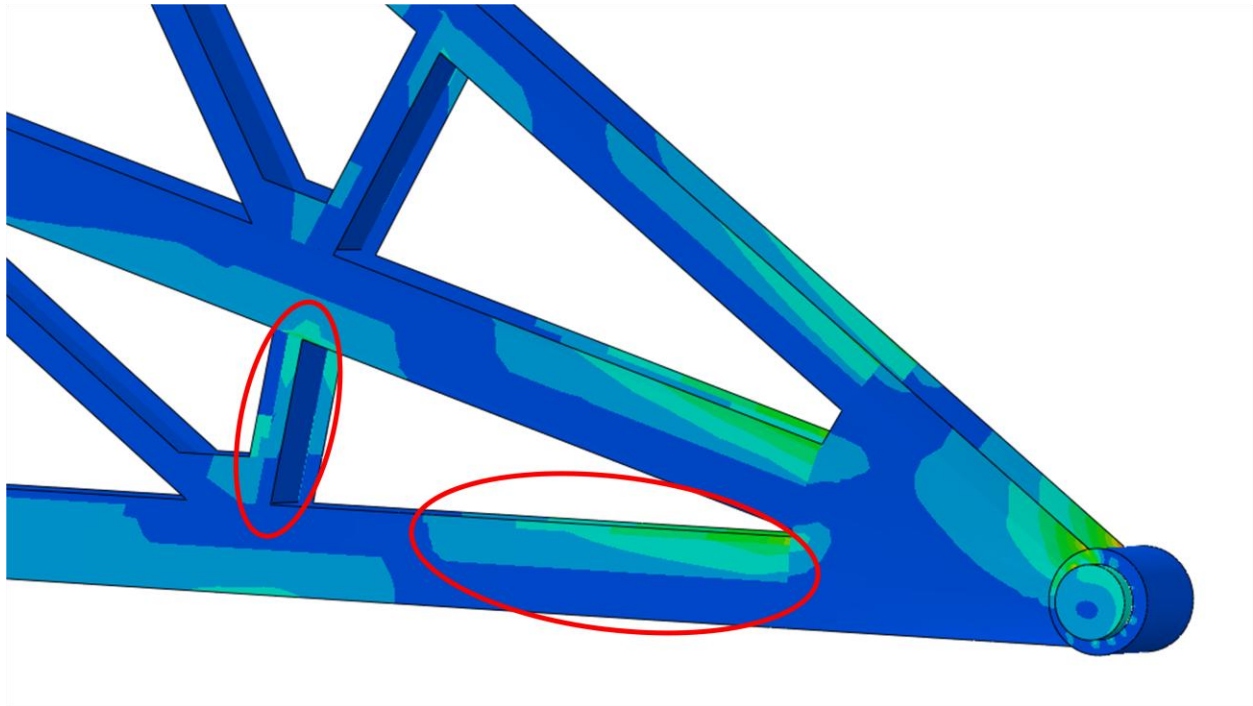


Figure 67: Stress configuration in the critical end frame members when the gate is lifted.

To evaluate the state of the structure and its vulnerability to failure, the principal stresses were taken at two of the most critical points of the structure. Figure 68 illustrates the points where the stresses were evaluated, DB, diagonal bracing and BS, bottom strut. The selection of these points was determined based on the results from the 3-D numerical model.

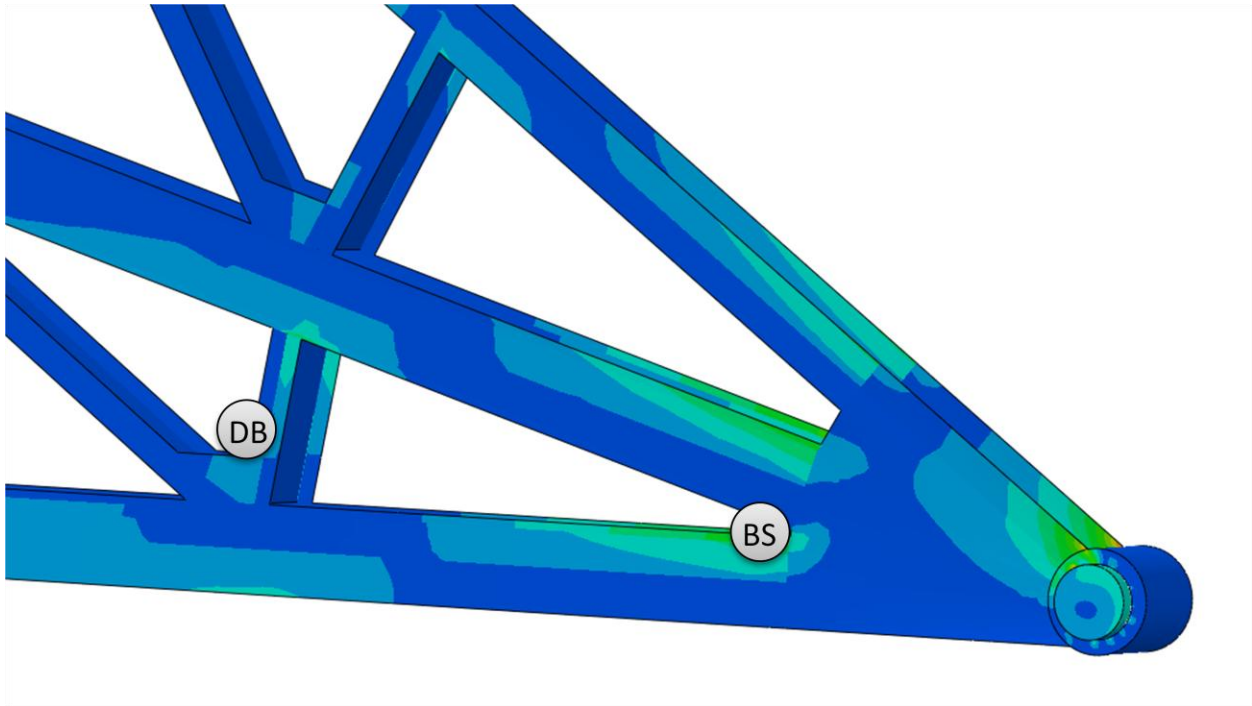


Figure 68: Points where the principal stresses were taken.

Since the gate was lifted and then lowered, the maximum and minimum principal stresses were taken to determine the compression and tension of these members. Table 5 and Table 6 illustrate the maximum and minimum principal stresses of the locations DB and BS for the left and right side of the gate. From the tables it is shown that there is not a significant difference in stresses from one side and the other because the structure and the loads are symmetric. Looking at the change in stresses throughout the experiments it can be seen that the maximum stresses occur when the gate stops at 16.8 in compression given that the highest value is the minimum principal stress.

Table 5: Maximum and Minimum Principal Stresses for the Diagonal Bracing (DB)

STEPS	DB _{left}		DB _{right}	
	Max. Principal (ksi) (+)	Min. Principal (ksi) (-)	Max. Principal (ksi) (+)	Min. Principal (ksi) (-)
On sill	0.19	1.7	0.17	1.6
Move up 9.6	0.17	2.3	0.14	2.1
Stop at 9.6	0	4.9	0	4.3
Move up 16.8	0	4.9	0	4.3
Stop at 16.8	0	6.5	0	5.7
Move down 9.6	0	6.5	0	5.7
Stop at 9.6	2.4	0	2.3	0
Down to 0	2.4	0	2.3	0
Stop at 0	0.14	0.92	0.15	0.85

Table 6: Maximum and Minimum Principal Stresses for the Bottom Strut (BS)

STEPS	BS _{left}		BS _{right}	
	Max. Principal (ksi) (+)	Min. Principal (ksi) (-)	Max. Principal (ksi) (+)	Min. Principal (ksi) (-)
On sill	0	3	0	3
Move up 9.6	0	3.6	0	3.6
Stop at 9.6	0	6.3	0	6
Move up 16.8	0	6.3	0	6
Stop at 16.8	0	7.7	0	7.4
Move down 9.6	0	7.7	0	7.4
Stop at 9.6	2.3	0	2.1	0
Down to 0	2.3	0	2.1	0
Stop at 0	0	1.5	0	1.5

Now that it was determined that the highest stress occurs when the gate stops at 16.8, the minimum principal stresses at this point are taken from the analyses with different friction coefficients to study the gradient of increase in the stresses with respect to the friction coefficient.

Table 7 illustrates the variation of stresses for the different friction coefficients when the gate stops at 16.8.

Table 7: Minimum principal stresses for different friction coefficients

Friction coefficient	Min. Principal (ksi) (-)			
	DB _{left}	DB _{right}	BS _{left}	BS _{right}
0.0	1.4	1.5	2.6	2.7
0.1	3.2	2.6	4.3	4.2
0.2	4.8	4.3	6	5.8
0.3	6.5	5.7	7.7	7.4

The results from Table 7 show an increase in stress as the friction coefficient increases, as it was expected. The rate of increase is about 1.5-ksi of the locations mentioned above.

5.2.2 *Unsymmetrical friction in trunnion pins*

A study for different friction coefficients in each pin was performed to evaluate its effect on the structural members and determined if the unsymmetrical loading due to the trunnion friction was a parameter affecting the calibration of the experimental results. Two analyses with two different friction coefficients in each pin-hub interaction were executed. The first one has a friction coefficient of 0.3 in the left pin-hub interaction and 0.1 in the right and the second analysis has the same friction coefficients but in the opposite sides.

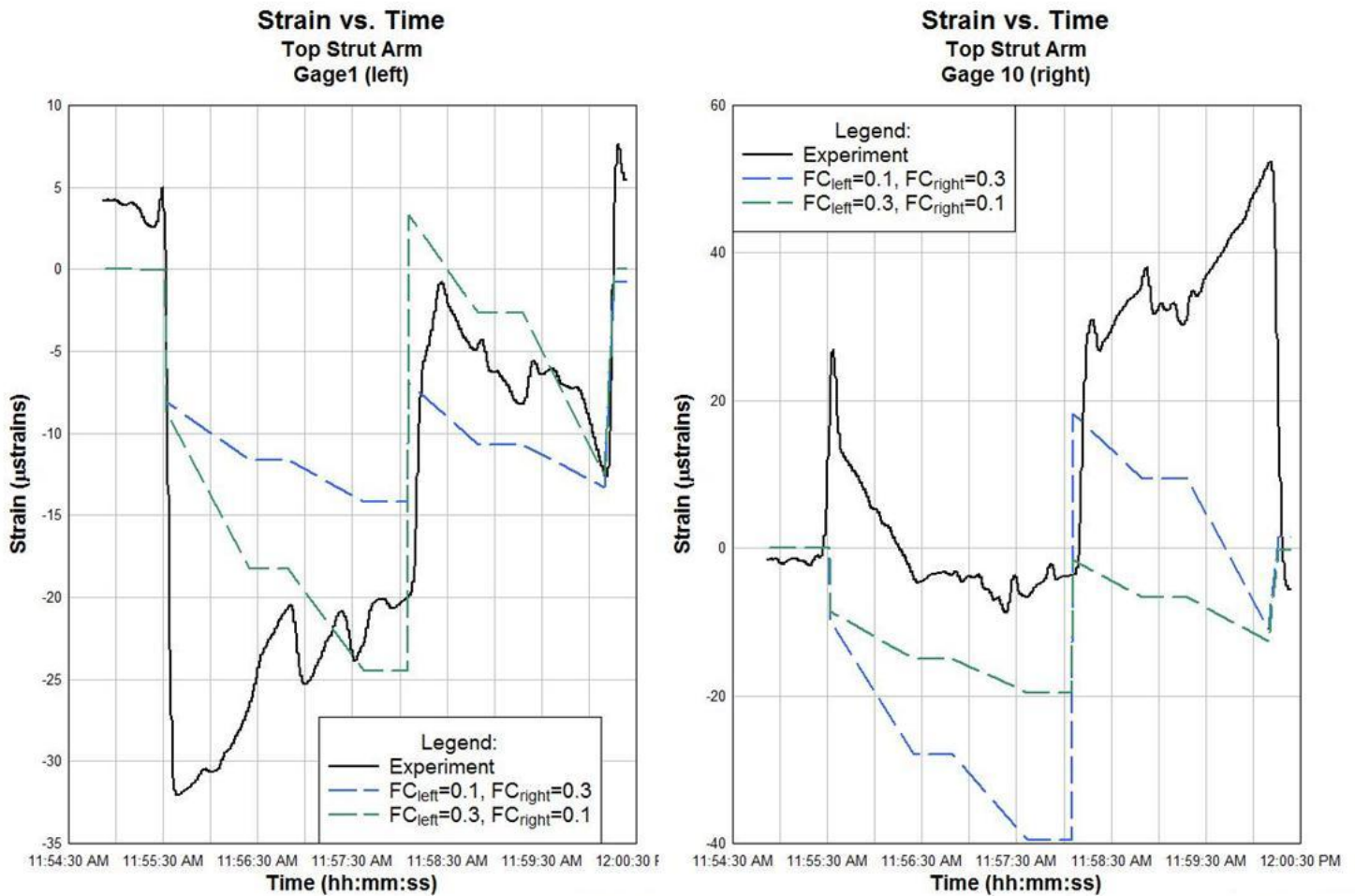


Figure 69: Different friction coefficient plots for top strut gages.

Figure 69 illustrates the plots for the analyses with different friction coefficients for the top strut arms. A gage from the left side of the gate (gage 2) was compared with a gage from the right side of the gate (gage 10) for the two different cases. The first plot illustrates the results from the analysis with the higher friction coefficient in the left side. As it was expected, the element on the side with the higher friction coefficient had higher strain magnitudes than the side with the lower friction coefficient. Even though there was a change in magnitude, the effect of

different friction coefficients in each pin did not affect behavior of the strains throughout the procedure. A similar conduct is observed in the bottom strut gages (Figure 70), the element in the side with the higher friction coefficient had higher strain magnitudes.

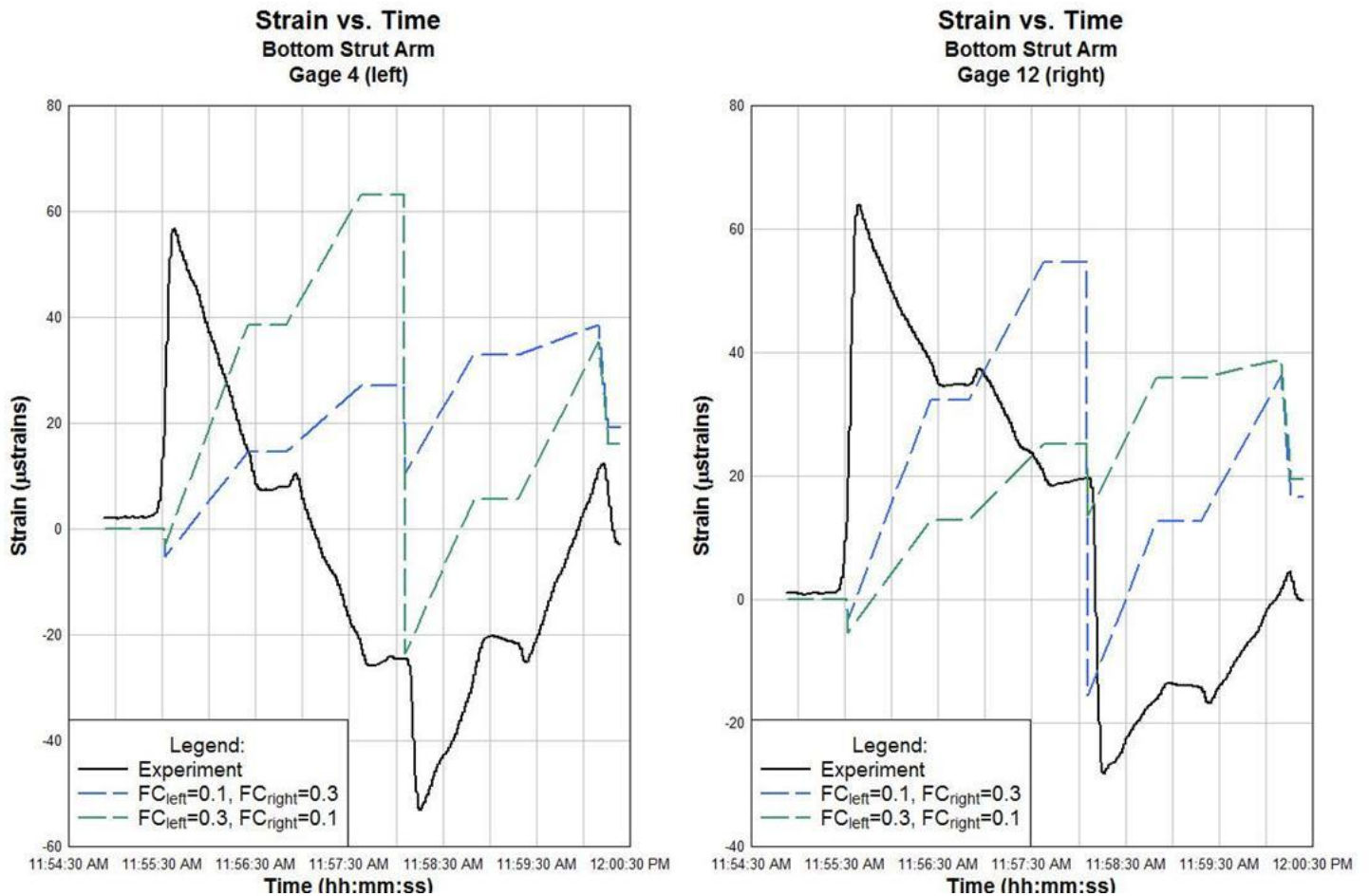


Figure 70: Different friction coefficient plots for bottom strut gages.

Table 8: Minimum Principal Stresses for the different friction coefficients analyses

Friction coefficient	Min. Principal (ksi) (-)			
	DB _{left}	DB _{right}	BS _{left}	BS _{right}
Left = 0.1, Right =0.3	3.2	5.7	4.3	6.7
Left = 0.3, Right =0.1	6.7	2.9	7.7	4.3

Table 8 illustrates the minimum principal stresses for the two cases of different friction coefficient. From the table it can be seen a significant change between one side and the other of the gate. However, comparing these values with the ones from Table 7, the stress values have similar magnitudes on the side that have the same friction coefficient. For example, point DB on the left side has a magnitude of 6.7-ksi for the analysis with a friction coefficient of 0.3 in the left and 0.1 in the right, that same point (DB_{left}) for the analysis of 0.3 friction coefficient in both pin had a magnitude of 6.5-ksi. The same with the right side (DB_{right}) for the analysis of FC_{left}=0.3 and FC_{right}=0.1, the stress value was 2.9-ksi compared to 2.6-ksi for the analysis with the same friction coefficient of 0.1 in both pins.

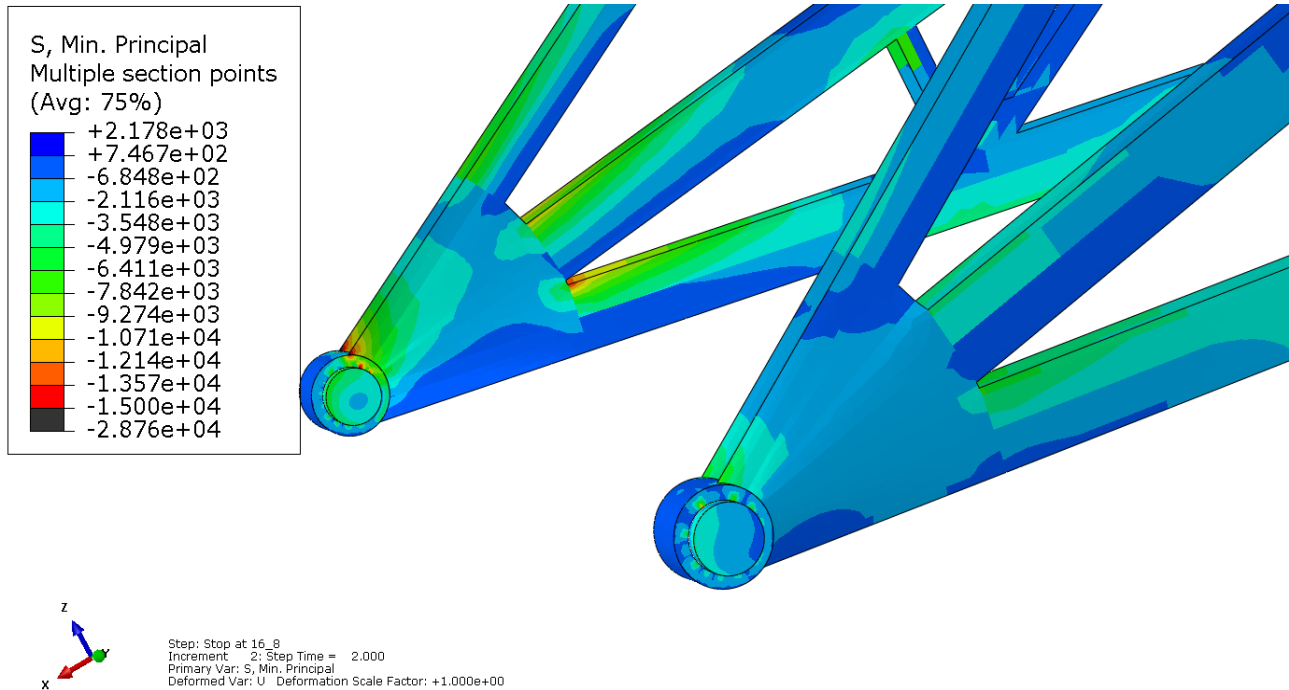


Figure 71: Stresses in the analysis with $FC_{\text{left}}=0.3$ and $FC_{\text{right}}=0.1$

Figure 71 illustrates the higher stresses in the left side of the gate due to the higher friction coefficient. A concentration of stresses with a magnitude of 15-ksi is observed at the connection of the gusset plate and the hub due to the change in geometry. The same conduct is observed in Figure 72 but the opposite side.

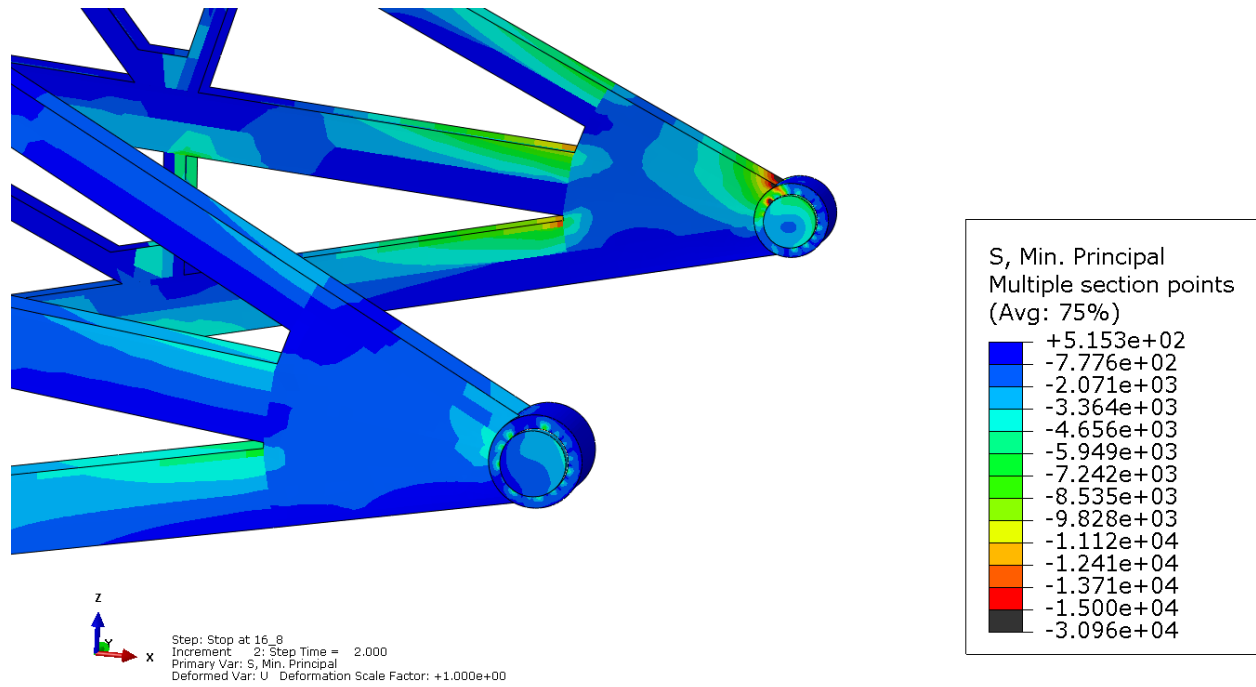


Figure 72: Stresses in the analysis with $FC_{left}=0.1$ and $FC_{right}=0.3$

5.3 Parametrical Analyses

A series of parametrical analyses were performed to study the behavior of the elements in the gate subjected to different load cases. The first analysis was the case of unsymmetrical loading due to the lifting cables. This is a very common condition in the operation of these gates since the motors not always perform at the same rate. This analysis was performed using the same simulation as the one used for the calibration of the model because one of the objectives was determine if the asymmetry in the cable pressure was parameter affecting the calibration of the model.

For the second analysis a new simulation was created, the gate was lifted to its highest state and the lowered back to the sill. The purpose of this analysis was to study the limit cases at which the gate can be subjected, including the gate without hydrostatic pressure and completely full.

5.3.1 *Unsymmetrical lifting cables*

Given that in the calibration of the model some of the behavior indicated possible unsymmetrical loading, an analysis with different cable pressures in each side was performed. In the analysis a higher load was applied to the left side of the gate. Figure 73 illustrates the effects of the unsymmetrical loading in the top strut gages 1 and 2 which are located at the left side of the gate. Comparing with the original calibration, a higher compressive strain was obtained in gage 1, from almost 8- μ strains to 33- μ strains in compression and a tensile behavior is observed at the beginning of the lifting of the gate in gage 2, from 10- μ strains in compression to 3- μ strains in tension.

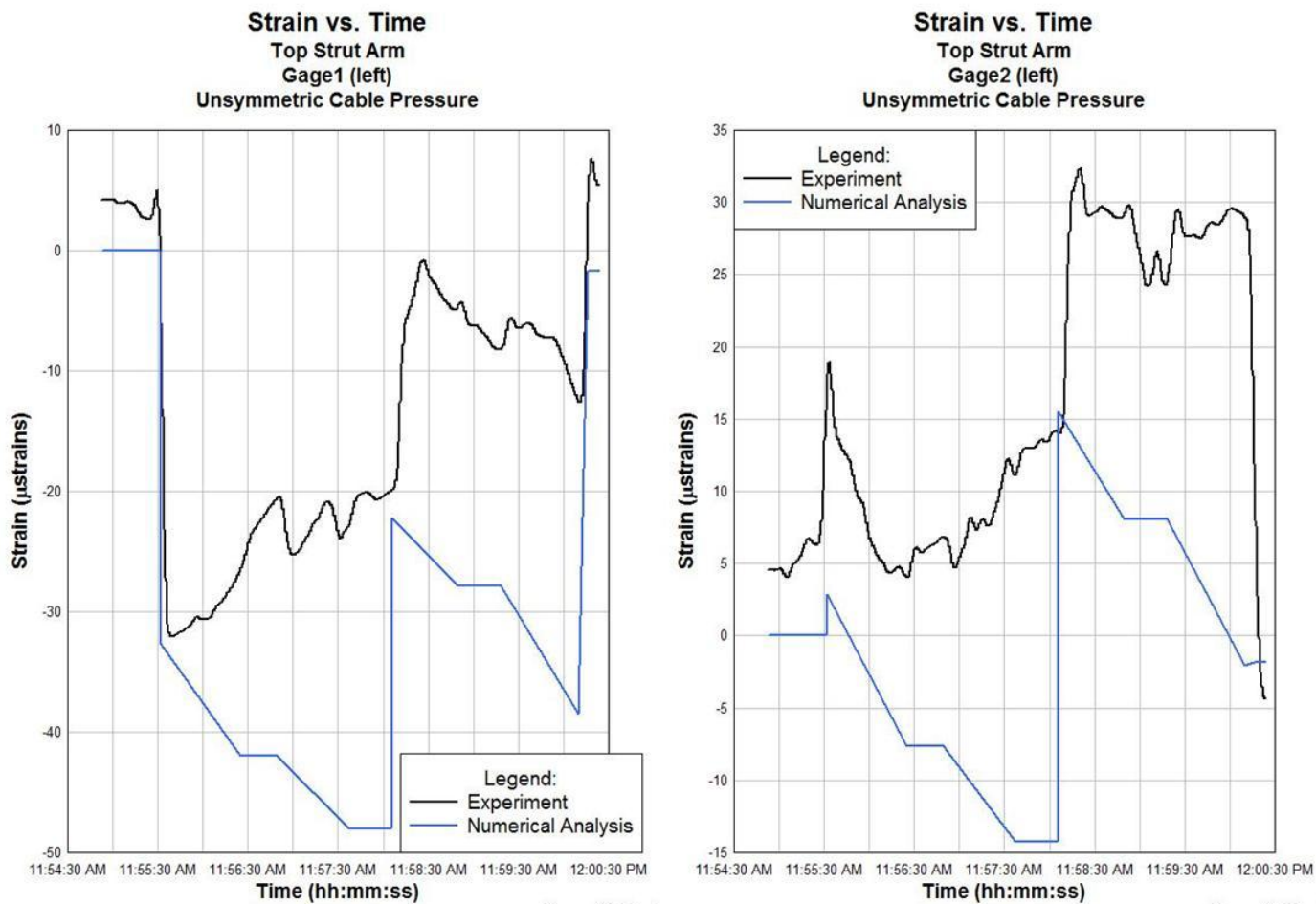


Figure 73: Effects of unsymmetrical loading in the left top strut

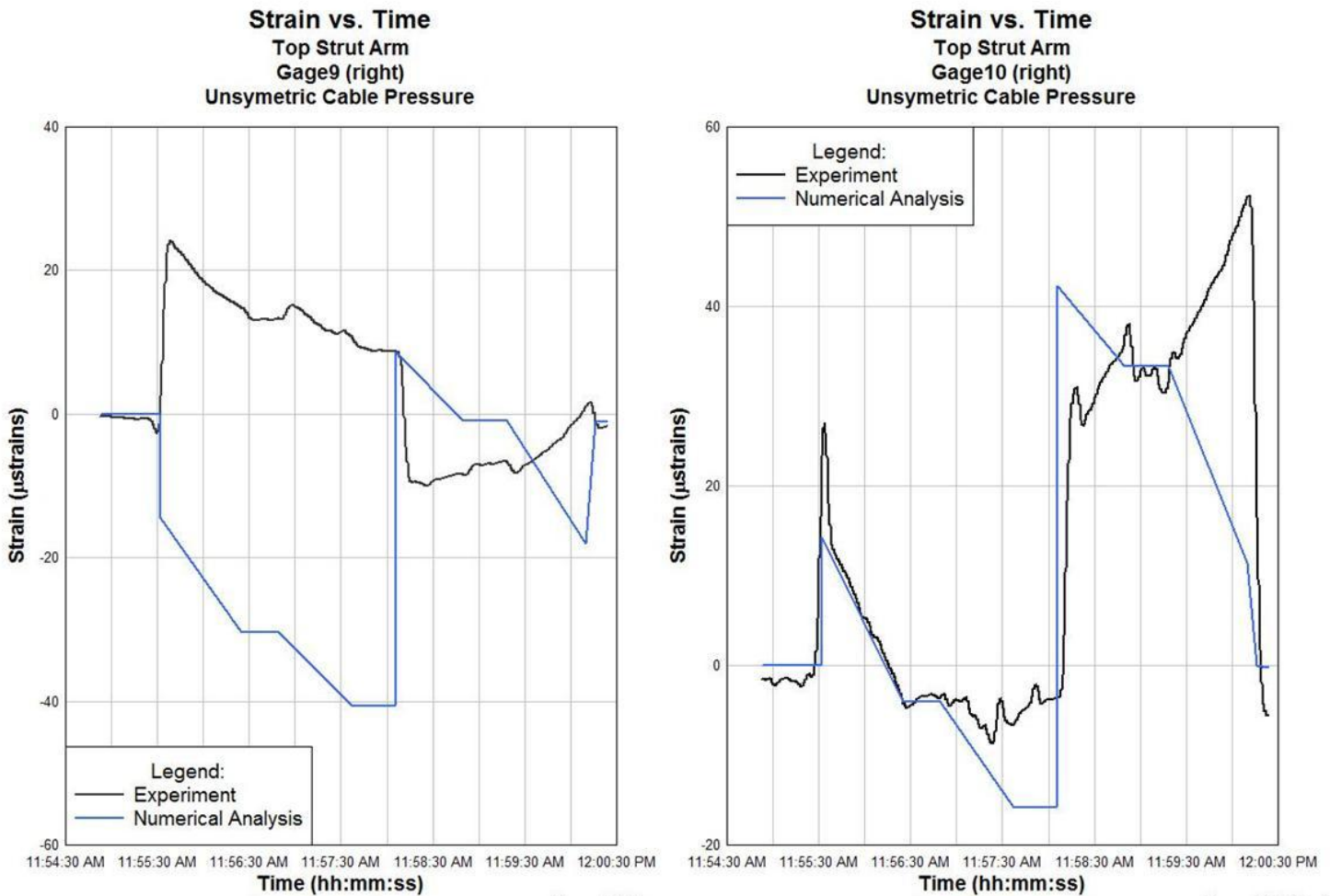


Figure 74: Effects of unsymmetrical loading in the right top strut

Figure 74 illustrate the behavior of the top strut gages 9 and 10 located at the right of the gate when subjected to unsymmetrical cable pressure loading. The same conduct as the gages from the right side can be observed. Gage 9 had an increase in compression, although not as significant as gage 1 because the higher cable pressure load was applied in the left side. Gage 10 had an increment in tension, almost replicating the same magnitude as the experiments.

These results simulates better the experimental results, thus it can be concluded that the structure was subjected to unsymmetrical loading due to the lifting cables.

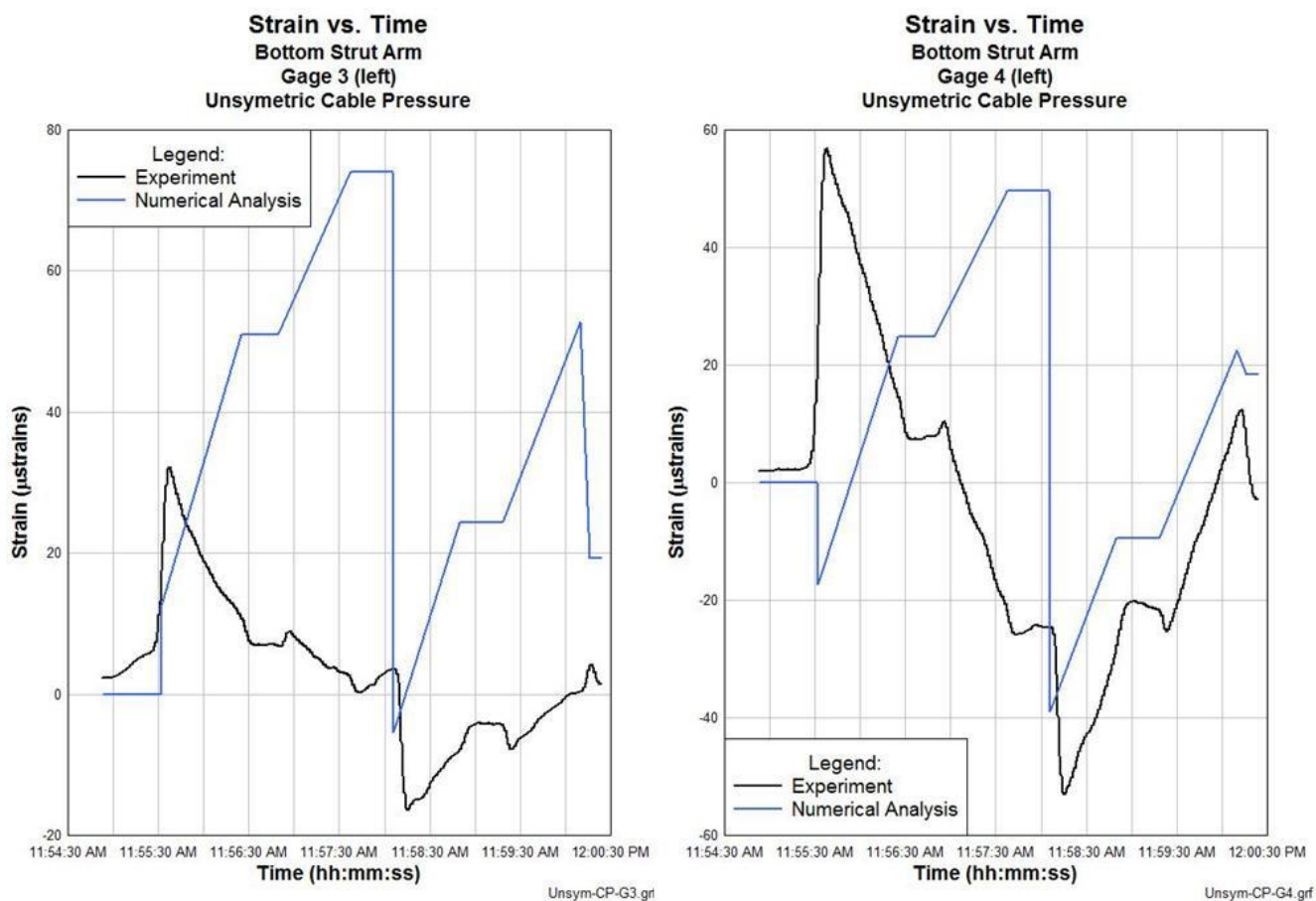


Figure 75: Effects of unsymmetrical loading in the left bottom strut

The effect of the asymmetric loading in the bottom struts is illustrated in Figure 75 and Figure 76. For these members an initial bending is observed on both sides of the structure (left and right bottom struts). Even though there is a higher cable pressure load applied in the left side of the gate, both bending magnitudes (in the left and right struts) are very similar because the cable pressure is not directly applied to the bottom strut region, contrary to the top strut gages where the initial bending is considerably higher in the left side.

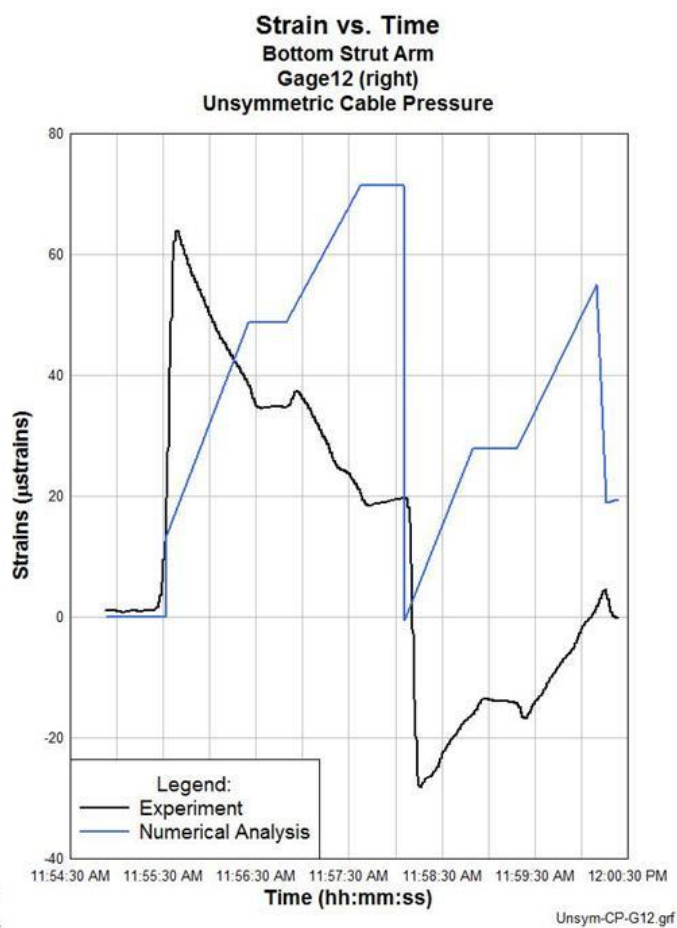
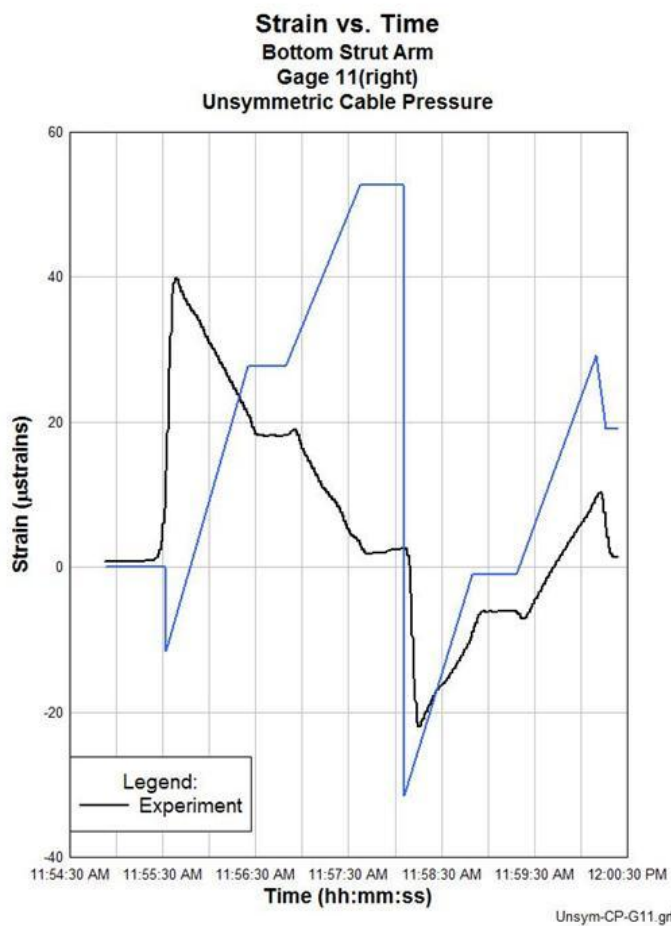


Figure 76: Effects of unsymmetrical loading in the right bottom strut

5.3.2 *Limit cases*

To evaluate the response of the structure under regular operation a 3-D simulation was created opening the gate 30-ft with no hydrostatic pressure and with the gate completely full. Both of these analyses had the same friction coefficient equal to 0.3. To study the change in stresses for this simulation in comparison with the simulation of the experimental procedure the same points (DB and BS) were used to take the stresses throughout the procedure. The purpose is to see how the principal stresses increase as the gate is lifted a significant height.

The simulation consisted in lifting the gate to an elevation of approximately 30-ft and then lowering it back to the sill. This procedure was performed applying small displacements to prevent the model from not converging. For this simulation the gate was lifted without stops because the purpose is to see the maximum stresses when the gate is completely open.

Table 9 illustrates the variation in maximum and minimum principal stresses in the DB and BS points for the simulations with the gate with no hydrostatic pressure and completely under water. For both the diagonal bracing (DB) and the bottom strut (BS) it can be seen how the points in the elements are acting in compression when the gate is going up and then in tension when the gate starts to move down.

Table 9: Principal Stresses for the Diagonal Bracing and the Bottom Strut

STEPS	DB _{left}				BS _{left}			
	No HP		Full Reservoir		No HP		Full Reservoir	
	Max. Principal (ksi) (+)	Min. Principal (ksi) (-)	Max. Principal (ksi) (+)	Min. Principal (ksi) (-)	Max. Principal (ksi) (+)	Min. Principal (ksi) (-)	Max. Principal (ksi) (+)	Min. Principal (ksi) (-)
On sill	0	0.4	1.1	5.5	0.08	0.03	0	9.5
Move up 15	0	0.4	0	0.3	0.04	0.07	0.13	0.02
Move up 45	0	4.3	0	12	0	4.3	0	15
Move up 75	0	4.1	0	9.9	0	4.1	0	13
Move up 105	0	4.7	0	9.3	0	4.8	0	12
Move up 135	0	3.2	0	6.5	0	3.1	0	8.1
Move up 165	0	4.9	0	8.1	0	4.9	0	8.3
Move up 195	0	2.1	0	3.9	0	2	0	3.9
Move up 225	0	5.4	0	7.4	0	5.5	0	6.3
Move up 255	0	0.38	0	0.52	0.09	0.19	0	0.2
Move up 285	0	5.6	0	6.9	0	5.6	0	5.6
Move up 315	0	1.8	0	2.2	0	1.5	0	1.5
Move up 345	0	4.4	0	5.5	0	4.4	0	4.4
Move up 375	0	1.8	0	2.3	0	1.6	0	1.6
Move down 345	0	3.8	0	4.8	0	3.8	0	3.8
Move down 315	5.8	0	7.2	0	6.5	0	6.6	0
Move down 285	2.8	0	3.4	0	3.3	0	3.4	0
Move down 255	4.4	0	5.4	0	5	0	5.1	0
Move down 225	2.6	0	3.2	0	3.2	0	3.2	0
Move down 195	5.6	0	6.9	0	6.4	0	6.4	0
Move down 165	0.5	0	0.5	0	0.9	0	0.93	0
Move down 135	5.5	0	6.4	0	6.3	0	5.7	0
Move down 105	1.8	0	1.4	0	2.3	0	0.9	0
Move down 75	5.2	0	5.4	0	5.9	0	3.6	0
Move down 45	2.5	0	2.1	0	3	0	0.8	0
Move down 15	4.7	0	4.7	0	5.3	0	2.1	0
Move down 0	5.4	0	2.9	0	6.2	0	1	0
Stop at 0	4	0	4	0	4.8	0	1.7	0

To understand the behavior of the strains throughout the lifting and lowering of the gate the axial strains were plotted with respect to the time for both locations mentioned above (DB and BS). Figure 77 shows the difference between the strains in the same location for the two limit case scenarios (gate empty and completely full). The red line illustrates the behavior of the strains in the diagonal bracing close to the trunnion when the gate is lifted and lowered without water and the blue line shows the strain behavior when the gate is full of water. When the gate is under the full hydrostatic pressure load the strains when the gate starts to open are considerably higher in compression than when the gate is empty. The red and the blue plots match when the gate is completely open because at this stage the hydrostatic pressure is not acting on the gate. As the gate moves down the strains from the gate under full hydrostatic pressure tend to compress again.

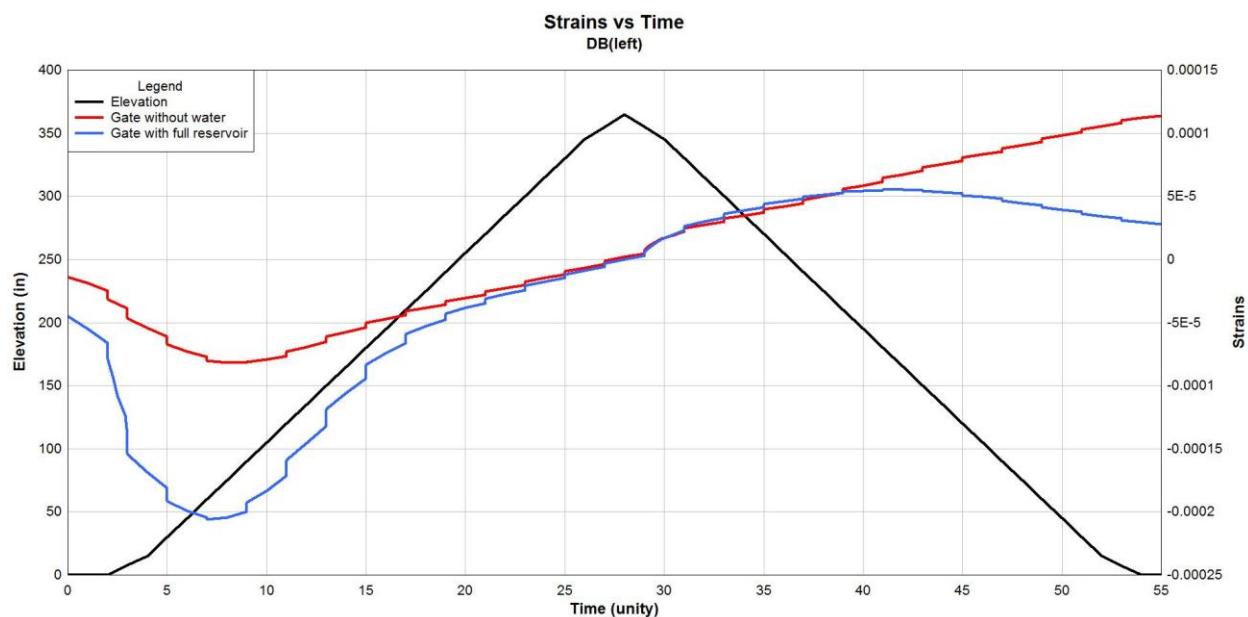


Figure 77: Strain vs. Time plot for DB

Figure 78 shows the strains behavior for the BS location which is at the bottom strut close to the trunnion. The magnitude of the strains at this location is considerably higher than in DB, which is the same conduct observed previously in the discussion of the experimental results. In the bottom strut it is also noticeable how the strains have higher compressive magnitudes when the gate is under hydrostatic pressure than when it is empty. As the gate starts to open the strains begin to compress and as the water level is lowering its level acting on the skin plate the strains increase in tension until the gate start to move down again.

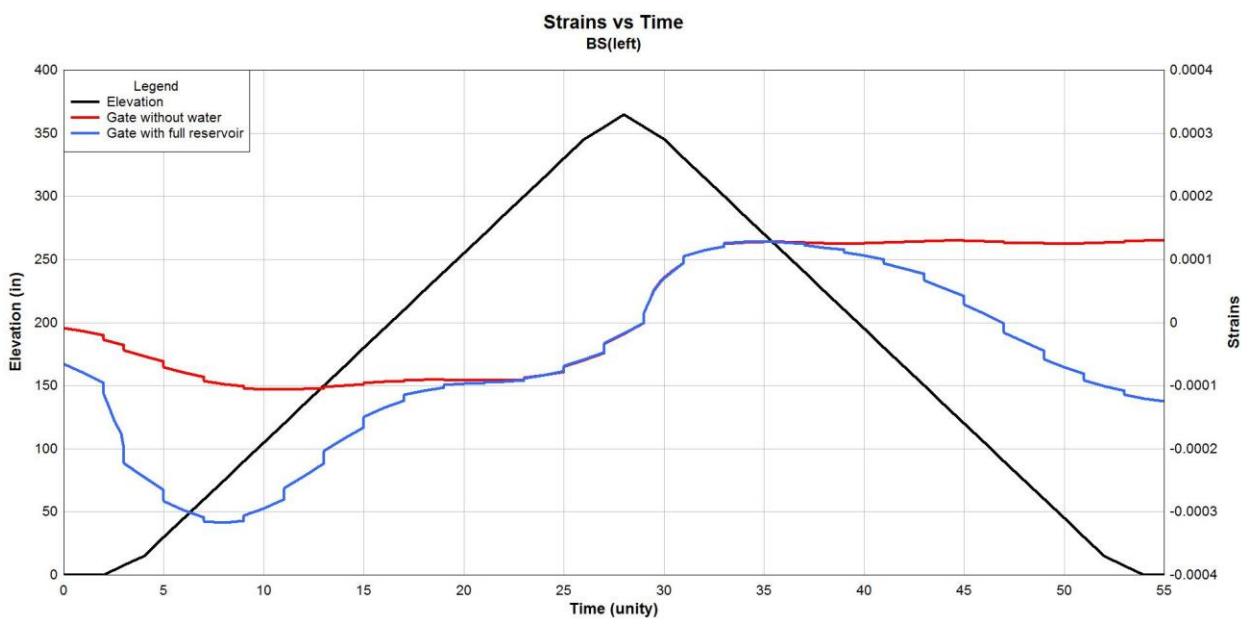


Figure 78: Strain vs. Time for BS

6 CONCLUSIONS AND RECOMMENDATIONS

In this investigation an evaluation of the of the Carlyle tainter gate structural members subjected to various friction coefficients and load cases was performed. A three-dimensional (3-D) numerical model of the Carlyle Dam tainter gate was created and successfully validated with the purpose of representing the stress behavior of a standard Corps of Engineer tainter gate structure subjected to various typical load cases. A series of parametrical analyses were performed to evaluate the performance of the structural members under different load cases and friction coefficients.

6.1 Conclusions

6.1.1 Design Consideration of the Carlyle tainter gate

The Carlyle Lake Dam tainter gate was subjected to the experimental procedures performed in 2008 by Dr. Gopalarathnam and Dr. Riveros. A revision of the design for this tainter gate was performed to corroborate the capacity of the structure under the actual loads. Two principal elements were chosen for this revision, the bottom horizontal girder and the bottom strut arm. The horizontal girder was considered to act as a beam and it satisfied the specifications for the AISC Manual 13 edition for flexural members. The bottom strut arm was considered to act as a beam column because it carries both axial and flexural forces. The original design of this member did not considered the weak axis moments generated by the trunnion pin friction. For the revision of this member the weak axis moment for this section was calculated and added to the stability equation to verify its compliance. The coefficient of friction used to

calculate the weak axis moment was 0.3. A comparison was made between the results taking the weak axis moment as zero and calculating this value. There was an increase from 0.73 to 0.94 but still less than 1, which means that the member stratifies the stability equation. With this calculation it is proven that not considering the bending of the strut in the minor axis could jeopardize the compliance of the stability equation.

6.1.2 Experimental Procedure

Sixteen gages were placed in the strut arms and diagonal bracing of the Carlyle Dam tainter gate to measure the behavior of the strains throughout the lifting and lowering of the gate. From the experimental results it was found that the members are have higher change in strains when the gate starts to move up and begins to move down due to the breaching of the static friction force and the applied cable pressure.

6.1.3 Computational Study of the Tainter Gate

A 3-D computational study was performed including the modeling and the simulation of the Carlyle Dam tainter gate using the finite element analysis software Abaqus. The modeling included the definition of the problem including the geometry of the gate, material properties, and the definition of the mesh. The simulation was the execution of the problem, in this case the duplication of the experimental procedures, which was performed by defining displacement boundary conditions and loads. The interaction between the pin and the hub was also defined at this stage. An implicit static general simulation was performed given that in the experimental procedure the gate was lifted and lowered at a slow rate.

6.1.4 Experimental Validation, Trunnion Friction Study and Parametrical Analyses

The 3-D numerical calibration of the Carlyle tainter gate was not quite the same from the experimental procedure but have very close behavior in most gages and reasonable strain magnitudes. The reason why the model did not behave exactly as the experimental results was that it was simulated under symmetric loading and perfect conditions and the experimental results suggested asymmetric loading throughout the procedure. However for the parametric analyses when the gate was subjected to asymmetric loading due to the lifting cables a better conduct was observed, especially for the top strut gages.

From the trunnion friction study it was discovered that the strains magnitudes in the elements are directly proportional to the value of the coefficient of friction between the pin and the hub. The higher the friction coefficient, the more abrupt change in strains will be gate the gate starts to move down.

The stress analysis on the finite element model showed that the elements with higher stress magnitudes are the ones closer to the trunnion area because they are receiving all the loads that are transferred trough the end frame to the pins.

6.2 Recommendations

It was found that with the experimental data obtained from the Carlyle Lake Dam was not sufficient to adequately measure the cable effects of the gate. For a future work it is recommended to measure the lifting mechanism (chain, tendons or cables) material properties and behavior during the operation of the gate. This date will help to have a better understanding

of the asymmetric loading effects on the gate and a more detailed calibration analysis could be performed.

Another parameter to consider in the numerical model is the effect of the vibrations that are produced by the water flowing through the bottom edge of the skin-plate. It is recommended to perform a dynamic explicit analysis to consider this load case.

REFERENCES

ABAQUS Inc. (2010). Documentation, Version 6.10. Rhode Island: Hibbitt, Karlsson and Sorensen, Inc.

American Institute of Steel Construction Inc. (2005). Steel Construction Manual 13 edition. Chicago IL.

"Design Standards No.7, Valves, Gates and Steel Conduits", August 14, 1950, and its revision date November 7, 1956, engineering manual by the Bureau of Reclamation, Denver, Colorado

Bureau of Reclamation Mid-Pacific Region (1996). *Spillway Gate 3 Folsom Dam*, Forensic Report, Sacramento, CA

Boyer, B., Anderson, B. and Jordan, S. (2001). "Tainter Gate Testing a Holistic Approach." In *Waterpower XII: Advancing Technology for Sustainable Energy*, Salt Lake City, UT, July 9-11, 2001. Kansas City, MO

Blau, P. (1992). "ASM Handbook Volume 18 Friction, Lubrication, and Wear Technology", ASM International

Cook, R. et al (2003) "Concepts and Applications of Finite Element Analysis, Fourth Edition," University of Wisconsin, Madison

Daleo, S. (1976). "Our Story the Chippewa Valley and Beyond", Eau Claire Leader Telegram, Eau Claire WI.

Dressier (1976), "Design Criteria for Tainter Gates", TGDA Workshop

Emkin L. Z. (1976) "General Purpose Computer-Aided Analysis and Design of Tainter Gates"
Vol. II, Tucker, GA

F.F. Ling, E.E. Klaus R. S. Fein, "Boundary Lubrication, An Appraisal of World Literature,"
1969, compiled and edited for ASME Research Committee on Lubrication.

Hansen, K., Gene Yow, M. and Xiong, Y. (2005). "Tainter Gate Testing and Evaluation Rocky
Reach Hydroelectric Project." In *Technologies to Enhance Dam Safety and the Environment*,
United States Society on Dams (USSD) Annual Conference, Salt Lake City, UT, June 6-10, 2005.
Denver, CO: United States Society on Dams

Headquarters, U.S. Army Corps of Engineers (1950). *Crest and Head Gates*, Engineer Manual
Civil Works Construction, Washington, DC

Headquarters, U.S. Army Corps of Engineers (2000). *Design of Spillway Tainter Gates*,
Engineer Manual 1110-2-2702, Washington, DC

Headquarters, U.S. Army Corps of Engineers (2001). *Inspection, Evaluation and Repair of
Hydraulic Steel Structures*, Engineer Manual 1110-2-6054, Washington, DC

Hibbeler R. C. (2005) "Mechanics of Materials sixth edition", Published by Pearson Prentice
Hall; Upper Saddle River, New Jersey

Ishii, N., Anami, K., Knisley, C.W., Oku, T., Aslam, M. (2009). "Field vibrations test concerning
the dynamic stability of tainter gates at the Poe Power Dam."

Journal of the Power Division (1962). "Structural Design Practices for Tainter Crest Gates".
Proceedings of the American Society of Civil Engineers, December 1962, San Mateo, CA

Riveros G. A. (2006). "Numerical Evaluation of Stress Intensity Factors: J-Integral Approach." Presented at *Proceedings of the Navigation Lock and Dam Inspection and Emergency Repairs Workshop*, Vicksburg, MS April 18-20, 2006. Vicksburg, MS: U.S. Army Engineer Research and Development Center

Todd, R. V. (1999). *Spillway Tainter Gate Failure at Folsom Dam, California, Hydro's Future: Technology, Markets and Policy*, ASCE Waterpower Conference 1999, Las Vegas NV, July 6-9, 1999, edited by Peggy A. Brookshier. Reston, VA: American Society of Civil Engineers.

Todd, R. (2005) "Evaluating a Tainter Gate's Dynamic Stability Using Modal Analysis", Conference: 2005 IMAC-XXIII: Conference & Exposition on Structural Dynamics

U.S. Army Engineer District St. Louis, MO and U.S. Army Engineer District Mobile, AL (1961). *Carlyle Main Dam Second Stage Design Memorandum No. 7*, Mobile, AL

Vadivuchezian K., Sundar S., Murthy H. (2011) "Effect of variable friction coefficient on contact tractions." *Tribology International*.

Zhuravlev V. F. (2010) "History of the Law of Dry Friction" *Doklady Physics*, 2010, Vol. 55. Pleiades Publishing, Ltd. 2010 Original Russian Text published in *Doklady Akademii Nauk*. Translated by G. Merzon.

APPENDIX A. LIMITING WIDTH-THICKNESS RATIOS FOR COMPRESSION ELEMENTS

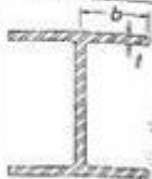
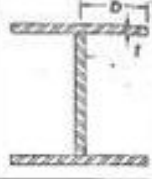
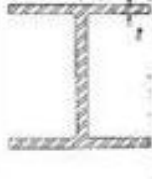
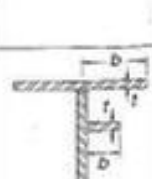
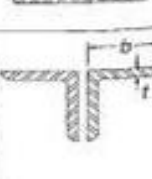
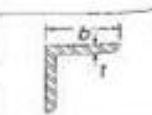
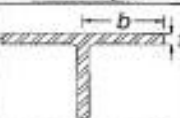
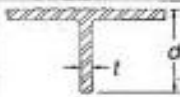
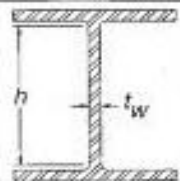
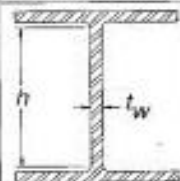
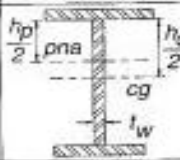
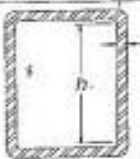
Case	Description of Element	Width Thickness Ratio	Limiting Width-Thickness Ratios		Example
			λ_p (compact)	λ_r (noncompact)	
Unstiffened Elements	1 Flexure in flanges of rolled I-shaped sections and channels	b/t	$0.38\sqrt{E/F_y}$	$1.0\sqrt{E/F_y}$	
	2 Flexure in flanges of doubly and singly symmetric I-shaped built-up sections	b/t	$0.38\sqrt{E/F_y}$	$0.95\sqrt{k_c E/F_y}^{(a)(b)}$	
	3 Uniform compression in flanges of rolled I-shaped sections, plates projecting from rolled I-shaped sections; outstanding legs of pairs of angles in continuous contact and flanges of channels	b/t	NA	$0.56\sqrt{E/F_y}$	
	4 Uniform compression in flanges of built-up I-shaped sections and plates or angle legs projecting from built-up I-shaped sections	b/t	NA	$0.64\sqrt{k_c E/F_y}^{(a)}$	
	5 Uniform compression in legs of single angles, legs of double angles with separators, and all other unstiffened elements	b/t	NA	$0.45\sqrt{E/F_y}$	
	6 Flexure in legs of single angles	b/t	$0.54\sqrt{E/F_y}$	$0.91\sqrt{E/F_y}$	

TABLE B4.1 (cont.)
Limiting Width-Thickness Ratios for
Compression Elements

Case	Description of Element	Width Thickness Ratio	Limiting Width-Thickness Ratios		Example
			λ_p (compact)	λ_r (noncompact)	
7	Flexure in flanges of tees	b/t	$0.38\sqrt{E/F_y}$	$1.0\sqrt{E/F_y}$	
8	Uniform compression in stems of tees	d/t	NA	$0.75\sqrt{E/F_y}$	
9	Flexure in webs of doubly symmetric I-shaped sections and channels	h/t_w	$3.76\sqrt{E/F_y}$	$5.70\sqrt{E/F_y}$	
10	Uniform compression in webs of doubly symmetric I-shaped sections	h/t_w	NA	$1.49\sqrt{E/F_y}$	
11	Flexure in webs of singly-symmetric I-shaped sections	h_c/t_w	$\frac{h_c}{h_p} \sqrt{\frac{E}{F_y}}$ $\left(0.54 \frac{M_p}{M_y} - 0.09\right)^2 \leq \lambda_r$	$5.70\sqrt{E/F_y}$	
12	Uniform compression in flanges of rectangular box and hollow structural sections of uniform thickness subject to bending or compression; flange cover plates and diaphragm plates between lines of fasteners or welds	b/t	$1.12\sqrt{E/F_y}$	$1.40\sqrt{E/F_y}$	
13	Flexure in webs of rectangular HSS	h/t	$2.42\sqrt{E/F_y}$	$5.70\sqrt{E/F_y}$	

Appendix B. Limit States Calculations for Girder W36x170

Steel Beam Design

Length from CL to CL	276	in
Dist from CL to gussets	7.35	in
Lb =	261.3	in

Middle and Bottom Girders
W36x170

Check if section is compact

W36x170 Section Properties			Material Properties		
d =	36.2	in	Fy =	50	psi
t _w =	0.68	in	E =	29000	psi
r _y =	2.53	in			
I _y =	320	in ⁴			
C _w =	98500	in ⁶			
S _x =	581	in ³			
J =	15.1	in ⁴			
h ₀ =	35.1	in			
Z _x =	668	in ³			
S _y =	53.2	in ³			
Z _y =	83.8	in ³			

If flexural members are compact ,
plastic moment can be reached
without local buckling.

from table1-1 of the AISC Manual 13ed

case 1 from table B4.1

case 9 from table B4.1

Flange		Web	
$\lambda = b/t =$	5.47	$\lambda = h/t_w =$	47.70
$\lambda_p =$	9.15	$\lambda_p =$	90.55
$\lambda_r =$	24.08	$\lambda_r =$	137.27
compact		compact	

Parameters to calculate lengths

c =	1	
r _{ts} =	3.11	in

Limiting Lengths		
L _b =	261.3	in
L _p =	107.24	in
L _r =	288.98	in
Lateral torsional buckling applies		

Doubly Symmetric Compact I-shaped Member Bent about their Major Axis:

Yielding

L_b > L_p

Does not meet the limit state of yielding in equation (F2-1)

$$\phi M_n = \phi 0.7 F_y S_x = \quad \mathbf{18,302 \text{ k-in}}$$

Lateral Torsional Buckling

When $L_p < L_b \leq L_r$

$$M_n = C_b \left[M_p - (M_p - 0.7F_y S_x) \left(\frac{L_b - L_p}{L_r - L_p} \right) \right] \leq M_p \quad (\text{F2-2})$$

(c) When $L_b > L_r$

$$M_n = F_{cr} S_x \leq M_p \quad (\text{F2-3})$$

where

L_b = length between points that are either braced against lateral displacement of compression flange or braced against twist of the cross section, in. (mm)

$$F_{cr} = \frac{C_b \pi^2 E}{\left(\frac{L_b}{r_{ts}} \right)^2} \sqrt{1 + 0.078 \frac{Jc}{S_x h_o} \left(\frac{L_b}{r_{ts}} \right)^2} \quad (\text{F2-4})$$

$M_p = F_y Z_x =$

33,400 k-in

Cb Calculation		
$M_{max} =$	13798.65	k-in
$M_a =$	10129.60	k-in
$M_b =$	13798.65	k-in
$M_c =$	10129.60	k-in
$R_m =$	1	for doubly symmetric members
$C_b =$	1.15	ok!

$M_n =$ 25,591 k-in

$\phi M_n =$ **23,032 k-in**

Nominal Shear Strength

a =	276	in
h =	32.436	in
a/h =	8.509064	
	29.7104984	
kv =	5	

h/tw =	47.7		1
	59.2368129		1.241862
	73.7767579		1.92459

Cv=	1	
Aw =	24.616	in ²

$$\phi V_n = \quad \quad \quad \mathbf{665 \text{ kip}}$$

Appendix C. Limit States Calculations for Strut Arm W14x13

Section W14x132.

From section H1 of the AISC Manual 13 ed.:

Doubly Symmetric Member Subjected to Flexure and Axial Force

$$\frac{P_r}{P_c} + \frac{8}{9} \left(\frac{M_{rx}}{M_{cx}} + \frac{M_{ry}}{M_{cy}} \right) \leq 1.0 \text{ for } \frac{P_r}{P_c} \geq 0.2$$

Determine ϕP_n

E 29000 ksi
Fy 50 ksi

strut arm with
3 braces

Determine the governing buckling mode



K	0.5	K	0.7	1	1	0.7
L	476.6 in	L	120	102	102	90
rx	6.28 in	ry	3.76	3.76	3.76	3.76
KL/rx	37.9	KL/ry	22.3	27.1	27.1	16.8

Fe = 198.78 ksi
0.44*Fy 20 ksi

Fcr = 45.00 ksi

Ag = 38.8 in

$$\phi P_n = \phi F_{cr} A_g$$

Pc = ϕP_n = **1,572 k**

To determine ϕM_n bent about their major axis

Lb =

476.6 in

Check if section is compact

W14x127 Section Properties			Material Properties		
d =	14.7	in	F _y =	50	ksi
t _w =	0.645	in	E =	29000	ksi
r _y =	3.76	in			
I _y =	548	in ⁴			
C _w =	25500	in ⁶			
S _x =	209	in ³			
S _y =	74.5	in ³			
J =	12.3	in ⁴			
h ₀ =	13.6	in			
Z _x =	234	in ³			
Z _y =	113	in ³			

from table1-1

case 1 from table B4.1

case 9 from table B4.1

Flange		Web	
$\lambda = b/t =$	7.15	$\lambda = h/t_w =$	17.70
$\lambda_p =$	9.15	$\lambda_p =$	90.55
$\lambda_r =$	24.08	$\lambda_r =$	137.27

compact

compact

Parameters to calculate lengths

c =	1	
r _{ts} =	4.22918849	in

Limiting Lengths		
$L_b =$	476.6	in
$L_p =$	159.37	in
$L_r =$	738.42	in
Lateral torsional buckling applies		

Yielding

$L_p > L_b$

Does not meet the limit state of yielding in equation (F2-1)

$$\phi M_n = \phi 0.7 F_y S_x = \quad \quad \quad \mathbf{6,584 \text{ k-in}}$$

Lateral Torsional Buckling

When $L_p < L_b \leq L_r$

$$M_n = C_b \left[M_p - (M_p - 0.7 F_y S_x) \left(\frac{L_b - L_p}{L_r - L_p} \right) \right] \leq M_p \quad (\text{F2-2})$$

(c) When $L_b > L_r$

$$M_n = F_{cr} S_x \leq M_p \quad (\text{F2-3})$$

where

L_b = length between points that are either braced against lateral displacement of compression flange or braced against twist of the cross section, in. (mm)

$$F_{cr} = \frac{C_b \pi^2 E}{\left(\frac{L_b}{r_{ts}} \right)^2} \sqrt{1 + 0.078 \frac{J_c}{S_x h_o} \left(\frac{L_b}{r_{ts}} \right)^2} \quad (\text{F2-4})$$

Cb Calculation		
$M_{max} =$	1.00	k-in
$M_a =$	1.00	k-in

$M_b =$	1.00	k-in
$M_c =$	1.00	k-in
$R_m =$	1	for doubly symmetric members
$C_b =$	1.00	ok!

$$Mn_x = 6,984 \text{ k-in}$$

$$\phi Mn_x = \mathbf{6,286 \text{ k-in}}$$

Nominal Shear Strenght

a =	476.6	in
h =	11.4165	in
a/h =	41.7465948	
	215.774522	
kv =	5	

h/tw =	17.7		1
	59.2368129		3.3467126
	73.7767579		13.977465

Cv =	1	
Aw =	9.4815	in ²

$$\phi Vn = \mathbf{256 \text{ k}}$$

To determine ϕM_n bent about their minor axis

Yielding

$$M_n = M_p = F_y Z_y \leq 1.6 F_y S_y$$

$$M_{n_y} = 5650 \text{ k-in}$$

$$\phi M_{n_y} = 5,085 \text{ k-in}$$

Flange Local Buckling

For sections with compact flanges the limit state of yielding shall apply.

Moment from friction force in the pin:

Rv =	659	Pin radius=	6
Rh =	104.73		
Rr =	667.27009		
assume cf	0.3		
Ff	200.181027		
Mf	1201.08616	k-in	

Summary

$$\frac{P_r}{P_c} + \frac{8}{9} \left(\frac{M_{rx}}{M_{cx}} + \frac{M_{ry}}{M_{cy}} \right) \leq 1.0 \text{ for } \frac{P_r}{P_c} \geq 0.2$$

Not considering weak axis moment:

Pr=	671	k	from etabs	Pr/Pc	0.426974	ok!
-----	-----	---	---------------	-------	----------	-----

$P_c = 1,571.53 \text{ k}$

$M_{rx} = 2130 \text{ k-in}$ from etabs

$M_{ry} = 0 \text{ k-in}$ from etabs

$M_{cx} = 6285.82 \text{ k-in}$

$M_{cy} = 5,085 \text{ k-in}$

Expression = 0.728 ok

Considering weak axis moment:

$P_r = 671 \text{ k}$ from etabs $P_r/P_c = 0.426974 \text{ ok!}$

$P_c = 1,571.53 \text{ k}$

$M_{rx} = 2130 \text{ k-in}$ from etabs

$M_{ry} = 1225 \text{ k-in}$ from etabs

$M_{cx} = 6285.82 \text{ k-in}$

$M_{cy} = 5,085 \text{ k-in}$

Expression = 0.942